KTH ROYAL INSTITUTE
OF TECHNOLOGY

Degree Project in Electrical Engineering

Second cycle, 30 credits

Automatic Identification of Machine Parameters for Motor Drives

Double degree in Electric Power Engineering

CARLA PETTA

Stockholm, Sweden, 2024

Automatic Identification of Machine Parameters for Motor Drives

Double degree in Electric Power Engineering

CARLA PETTA

Degree Programme in Electrical Engineering
Date: February 20, 2024

Supervisor: Gustaf Falk Olson Supervisor
Examiner: Luca Peretti, Iustin Radu Bojoi
Royal Institute of Technology School of Electrical Engineering and Computer Science and Polytechnic of Turin Energy Department
Host company: Imperix Ltd
Supervisors at the host company: Nicolas Cherix, Simon Strobl
Swedish title: Automatisk identifiering av maskinparametrar för motor drivenheter
Swedish subtitle: Dubbel examen i elkraftteknik

Abstract

In industrial settings, a common challenge associated with electrical machines is the lack of parameters, which are not always available from the machine manufacturer. These parameters play a crucial role in tuning the control gains of Field-Oriented Control (FOC). Traditional parameter identification methods, widely accepted in the literature, are the standard IEEE tests such as DC measurement, no-load test, locked-rotor test, and short circuit test. However, their implementation can be impractical as they necessitate additional equipment that may be costly and not readily accessible.

This thesis addresses self-commissioning procedures as a solution to this challenge, aiming to automatically identify electrical parameters of machine equivalent circuits. Specifically, this study focuses on the Imperix motor testbench, comprising Induction Machine (IM) and Surface Mounted Permanent Magnet Synchronous Machine (SPMSM). Self-commissioning is a standstill procedure that utilizes signal injection through a power converter and the available sensors, with minimal operator intervention and no additional equipment.

For the SPMSM, the parameters under study include the stator resistance, the synchronous inductance, and the Permanent Magnets (PM)-flux. The resistance is estimated through direct current injection considering the inverter non-linearity. The synchronous inductance and its saturation characteristic are examined using high-frequency sinusoidal injection with and without DC bias via a Current Controller (CC), and square wave voltage injection through hysteresis control. The PM-flux is determined by accelerating the SPMSM using the IM as a prime mover in an open circuit configuration. This deviation from the standstill constraint of the self-commissioning procedure is necessary as the PM's effect becomes visible only when the rotor speed is non-zero.

For the IM, the stator resistance, the leakage inductance, the rotor resistance, and the magnetizing inductance are analyzed. The stator resistance and inverter non-linearity are identified using the same method as for the SPMSM. The leakage inductance is tested with a high-frequency sinusoidal injection with stepped DC bias, with which the saturation characteristic is built. Then, a DC-biased low-frequency sinusoidal injection identifies the rotor resistance. The magnetizing inductance is not identified in this work because of the extensive nature of the problem and time constraints.

Comparison with standard IEEE tests serves as validation, demonstrating close alignment of the results, except for discrepancies in the unsaturated SPMSM synchronous inductance estimation. The introduced innovation involves adapting existing procedures, initially developed for other AC machines, to SPMSM applications, for which only limited literature is available. Overall, this work makes a valuable contribution to understanding the influence of inverter non-linearity and saturation behavior on parameter identification. It also opens the door to integrating saturation effects into control algorithms, which enables dynamic adjustment of FOC gains, potentially enhancing control performance.

Keywords

Parameter estimation, Machine vector control, Motor drives, IM, Permanent Magnet Synchronous Machine (PMSM), Variable Speed Drives (VSD).

Sammanfattning

I industriella miljöer är en vanlig utmaning i samband med elektriska maskiner bristen på parametrar, som inte alltid är tillgängliga från maskintillverkaren. Dessa parametrar spelar en avgörande roll för att ställa in kontrollförstärkningarna för FOC. Traditionella metoder för parameteridentifiering, som är allmänt accepterade i litteraturen, är standard IEEE-tester som DC-mätning, nollbelastningstest, låst rotortest och kortslutningstest. Implementeringen av dessa kan dock vara opraktisk eftersom de kräver ytterligare utrustning som kan vara kostsam och svåråtkomlig.

Denna avhandling behandlar procedurer för självavstängning som en lösning på denna utmaning och syftar till att automatiskt identifiera elektriska parametrar för maskinens ekvivalenta kretsar. Studien fokuserar särskilt på Imperix motortestbänk, som består av IM och SPMSM. Självinkoppling är en stillesståndsprocedur som använder signalinjektion genom en kraftomvandlare och de tillgängliga sensorerna, med minimal operatörsintervention och utan extra utrustning.

För SPMSM studeras parametrarna statorresistans, synkroninduktans och PM-flöde. Motståndet uppskattas genom likströmsinjektion med hänsyn till växelriktarens olinjäritet. Den synkrona induktansen och dess mättnadskarakteristik undersöks med hjälp av högfrekvent sinusinjektion med och utan DC-bias via en CC, och fyrkantsvåginjektion genom hysteresstyrning. Flödet PM bestäms genom acceleration av SPMSM med hjälp av IM som drivmotor i en öppen krets-konfiguration. Denna avvikelse från stillesståndsbegränsningen i förfarandet för självavstängning är nödvändig eftersom PM:s effekt blir synlig först när rotorhastigheten är skild från noll.

För IM analyseras statorresistansen, läckinduktansen, rotorresistansen och den magnetiserande induktansen. Statorresistansen och inverterns olinjäritet identifieras med samma metod som för SPMSM. Läckageinduktansen testas med en högfrekvent sinusformad injektion med stegad DC-bias, med vilken mättnadskarakteristiken byggs. Därefter identifierar en DC-baserad lågfrekvent sinusinjektion rotorresistansen. Den magnetiserande induktansen identifieras inte i detta arbete på grund av problemets omfattande natur och tidsbegränsningar.

Jämförelse med standard IEEE-tester fungerar som validering och visar att resultaten ligger nära varandra, med undantag för avvikelser i uppskattningen av den omättade synkrona induktansen för SPMSM. Den introducerade innovationen innebär att befintliga procedurer, som ursprungligen utvecklats för andra AC-maskiner, anpassas till SPMSM-tillämpningar, för vilka endast begränsad litteratur finns tillgänglig. Sammantaget ger detta arbete ett värdefullt bidrag till förståelsen av hur omriktarens icke-linjäritet och mättnadsbeteende påverkar parameteridentifieringen. Det öppnar också dörren för att integrera mättnadseffekter i regleralgoritmer, vilket möjliggör dynamisk justering av FOC-förstärkningar, vilket potentiellt kan förbättra reglerprestanda. Jämförelse med standard IEEE-tester fungerar som validering och visar att resultaten ligger nära varandra, med undantag för avvikelser i uppskattningen av den omättade synkrona induktansen för SPMSM. Den introducerade innovationen innebär att befintliga procedurer, som ursprungligen utvecklats för andra AC-maskiner, anpassas till SPMSM-tillämpningar, för vilka endast begränsad litteratur finns tillgänglig. Sammantaget ger detta arbete ett värdefullt bidrag till förståelsen av hur omriktarens icke-linjäritet och mättnadsbeteende påverkar parameteridentifieringen. Det öppnar också dörren för att integrera mättnadseffekter i regleralgoritmer, vilket möjliggör dynamisk justering av FOC-förstärkningar, vilket potentiellt kan förbättra reglerprestanda.

Nyckelord

Parameterestimering, maskinvektorstyrning, motordrifter, Induktionsmaskiner, synkronmaskiner med permanent magnet, frekvensomriktare.

Acknowledgments

to complete

Sion, Switzerland, February 2024
Carla Petta

Contents

List of acronyms and abbreviations

ACG	Automated Code Generation
ADALINE	Adaptive Linear Neuron
ADC	Analog to Digital Converter
CB PWM	Carrier-based PWM
CC	Current Controller
DFT	Discrete Fourier Transform
DTC	Direct Torque Control
DUT	Device Under Test
EMF	Electromagnetic Force
FEA	Finite Element Analysis
FOC	Field-Oriented Control
GPI	General Purpose Inputs
GPO	General Purpose Outputs
IM	Induction Machine
IPMSM	Interior Permanent Magnet Synchronous Machine
LLS	Linear least-squares
LUT	Lookup Table
MLR	Multiple Linear Regression
MMF	Magneto Motive Force
OL	Open Loop
PI	Proportional Integral
PM	Permanent Magnets
PMSM	Permanent Magnet Synchronous Machine
PR	Proportional Resonant
PWM	Pulse Width Modulation
RCP	Rapid Control Prototyping
RFOC	Rotor Field Oriented Control
RMS	Root Mean Square

SC	Speed Controller
SDK	Software Development Kit
SEIG	Self-Excited Induction Generator
SiC	Silicon Carbide
SMO	Sliding-Mode Observer
SPMSM	Surface Mounted Permanent Magnet Synchronous Machine
SynRM	Synchronous Reluctance Machines
VSD	Variable Speed Drives

List of Symbols Used

The following symbols will be later used within the body of the thesis.

$\mathbf{i}_m^s$	Magnetizing current space vector in the $\alpha\beta0$ stationary reference frame , see equation (2.28), page 15
$\mathbf{i}_r^r$	Rotor current space vector in the rotor reference frame , see equation (2.24), page 14
$\mathbf{i}_R^s$	Rotor current space vector in the $\alpha\beta0$ stationary reference frame in the inverse-Γ equivalent circuit , see equation (2.34), page 16
$\mathbf{i}_r^s$	Rotor current space vector in the $\alpha\beta0$ stationary reference frame in the T-circuit , see equation (2.25), page 14
$\mathbf{i}_R^{dq0}$	Rotor current space vector in the dq0 reference frame in the inverse-Γ equivalent circuit , see equation (2.45), page 18
$\mathbf{i}_s^s$	Stator current space vector in the $\alpha\beta0$ stationary reference frame , see equation (2.5), page 8
$\mathbf{i}_s^{dq0}$	Stator current space vector in the dq0 reference frame , see equation (2.10), page 10
$\mathbf{v}_r^r$	Rotor voltage space vector in the rotor reference frame , see equation (2.24), page 14
$\mathbf{v}_s^s$	Stator voltage space vector in the $\alpha\beta0$ stationary reference frame , see equation (2.5), page 8
$\mathbf{v}_s^{dq0}$	Stator voltage space vector in the dq0 reference frame , see equation (2.10), page 10
ω_e	Synchronous angular speed of the dq0 reference frame , see equation (2.9), page 9

ω_m	Mechanical angular rotor speed, see equation (2.1), page 6
ω_r	Electrical angular rotor speed , see equation (2.26), page 15
ω_{slip}	Angular slip speed , see equation (2.45), page 18
$\boldsymbol{\psi}_r^r$	Rotor flux space vector in the rotor reference frame , see equation (2.24), page 14
$\boldsymbol{\psi}_R^s$	Rotor flux space vector in the $\alpha\beta0$ stationary reference frame in the inverse-Γ equivalent circuit , see equation (2.34), page 16
$\boldsymbol{\psi}_r^s$	Rotor flux linkage space vector in the $\alpha\beta0$ stationary reference frame , see equation (2.5), page 8
$\boldsymbol{\psi}_r^s$	Rotor flux space vector in the $\alpha\beta0$ stationary reference frame in the T-circuit for IM , see equation (2.25), page 14
$\boldsymbol{\psi}_R^{dq0}$	Rotor flux space vector in the dq0 reference frame in the inverse-Γ equivalent circuit , see equation (2.45), page 18
$\boldsymbol{\psi}_s^s$	Stator flux space vector in the $\alpha\beta0$ stationary reference frame , see equation (2.5), page 8
θ	Phase angle of the rotor flux linkage space vector in the $\alpha\beta0$ stationary reference frame , see equation (2.6), page 9
θ_e	Synchronous angle between d-axis and α-axis , see equation (2.10), page 10
θ_r	Rotor position in the $\alpha\beta0$ stator reference frame , see equation (2.25), page 14
L_M	Transformed magnetizing inductance in the inverse-Γ equivalent circuit , see equation (2.37), page 17
L_m	Magnetizing inductance in the T-circuit , see equation (2.28), page 15
L_s	Synchronous inductance, see equation (2.5), page 8
L_σ	Total leakage inductance in the inverse-Γ equivalent circuit , see equation (2.37), page 17
L_{rl}	Rotor leackedge inductance in the T-circuit , see equation (2.30), page 16

L_{sl}	Stator leackedge inductance in the T-circuit , see equation (2.30), page 16
R_R	Transformed rotor resistance in the inverse-Γ equivalent circuit , see equation (2.39), page 17
R_r	Rotor resistance in the T-circuit , see equation (2.24), page 14
R_s	Stator resistance, see equation (2.5), page 8

Chapter 1

Introduction

1.1 Evolution of commissioning procedures

The general definition of ”commissioning” in an electrical environment is the systematic process of testing equipment, systems, or facilities to ensure that they meet the design and operational requirements of the owner.

In the field of electrical machines and drives, a preliminary action, necessary to perform the normal routine of a motor (start-up and the various control strategies), is the knowledge of machine parameters. Electrical machines are characterized by a nameplate in which basic information under rated and limit conditions is provided, such as current, voltage, power, torque, and speed. On the other side, electrical parameters (resistances, inductances of the machine’s equivalent circuit) and mechanical parameters (inertia and viscous friction coefficient) should be found in the datasheet. However, the datasheet of the available machines in the market does not always present all these necessary information.

This represents a typical problem in industrial environments. The motor commissioning is thus related to the development of control techniques for Variable Speed Drives (VSD). For this reason, the subject has been dealt with since the 1990s, as shown by the publication of Peter Vas in [1]. In fact, around the 1980s, VSD were introduced. Thanks to the development of AC control techniques, AC motors spread into new fields of application where smooth control is required, partly replacing the DC motors used until then.

The advances in semiconductor technology led to improvements in power electronics components (for instance higher switching frequencies), which made VSD even more popular in industrial and commercial settings. With the ever-changing industrial sector over the years, the need to automate manufacturing processes has increased. Therefore, electric motor commissioning processes have also been automated to keep up.

Motor commissioning is always evolving in parallel with industrial and electric drive progress, the reason why different methods have been developed over the years, as discussed in Section 3.1.

1.2 Problem and definition

The subject of self-commissioning for AC motor drives, addressed in this thesis, refers to automatically configuring and tuning a motor drive system. Looking at the structure of the words, it is possible to derive its definition.

The meaning of ”commissioning” is already presented in Section 1.1. The use of the prefix ”self” highlights the automatic nature of this process, with minimal or no user involvement [2]. Self-commissioning is an automatic procedure performed when the machine is operated (online) or one time before its starting up (offline). It allows the initialization of the drive system and ensures that it operates efficiently and effectively in a given application. Specifically, calibration, identification of machine parameters, and automatic tuning are involved in this routine.

Different methods are presented in the literature, for instance, the standard tests proposed by the IEEE in [3] such as the DC, no-load, and locked-rotor tests. These tests are not automated and, depending on the particular application, it is not always possible to perform them on machines already placed on site. Their drawbacks are the use of additional equipment, which could be expensive and not always available, and the request of considerable time and effort, which, in an industrial environment, are translated into costs and loss of production. Moreover, the accuracy of machine parameters can be affected by the method and the type of equipment used. In fact, in high-performance control in which fast response, zero steady-state error, and accurate reference tracking are required from the motor drive, accurate knowledge of machine parameters is fundamental [4].

Optimization of costs, time, and accuracy is achieved by automating the process.

More specifically, the research question is:

How can a state-of-the-art automatic identification procedure of parameters be implemented for the Imperix motor testbench, which is composed of Induction Machine (IM) and Surface Mounted Permanent Magnet Synchronous Machine (SPMSM)?

1.3 Purpose

1.3.1 Host company

The main actor of this project is the Swiss company Imperix. The company offers high-end control and power solutions for research laboratories in power electronics. As part of its R&D activities, Imperix seeks to continuously develop state-of-the-art control techniques for all sorts of power converters. It provides its customers with a set of examples of standard control techniques implemented on its products, creating a publicly accessible knowledge base via the website. The continuously growing knowledge base is essential to effectively support its customers, mostly world-leading universities and industries. This purpose involves also electrical drives. Imperix wishes to include the procedure under study of self-commissioning for motor drives in its existing Field-Oriented Control (FOC) examples. FOC is a control technique that relies on knowledge of machine parameters for tuning.

Incorporating the self-commissioning procedure into Imperix's knowledge base will strengthen its support for electrical drives, potentially enhancing competitiveness in the market and offering customers more advanced solutions.

1.3.2 Academic community

For the academic community, this work is scientifically relevant because it keeps track of the progress made in the field of self-commissioning over the years, summarizing a very vast and constantly evolving topic. This could serve as a valuable resource for identifying machine parameters in the future. Moreover, this work contributes to develop scientific knowledge on machine parameter identification because it adapts existing procedures on new applications.

1.3.3 Sustainability

The final purpose is addressed to the world and the sustainability process. The project contributes in an indirect way to sustainability questions because it addresses techniques that do not require additional hardware, which means a reduction of electronic waste, by promoting sustainable design. This improves also the long-term impact, reducing maintenance and improving durability.

1.4 Method

To address the research question defined in Section 1.2, the following goals have to be reached.

Goal 1 Machine modeling:

- **Task 1** Define the theoretical knowledge of the AC motors.
- **Task 2** List all the parameters that should be identified for FOC.

Goal 2 Literature review:

- **Task 1** Study and classify existing parameters' identification techniques for the AC motors. This set a full understanding of the possible procedures available from the literature.
- **Task 2** Select and justify which method will be implemented among those available from the literature.

Goal 3 Simulation design:

- **Task 1** Implement the chosen method in simulation using the parameters provided by the machine manufacturer.

Goal 4 Experimental validation:

- **Task 1** Test and validate the selected self-commissioning procedures on the experimental imperix motor testbench, identifying strengths and drawbacks of the tested procedure.
- **Task 2** Test and validate the IEEE standard tests in [3] and [5] on the imperix motor testbench, identifying strengths and drawbacks of the tested procedure.

Goal 5 Comparison and conclusions:

- **Task 1** Compare the obtained results from the self-commissioning procedures and the IEEE standard.
    - If the results of both self-commissioning and standard tests align and this comparison can be scientifically explained, the self-commissioning method can be considered technically relevant.
    - If the results of both self-commissioning and standard tests do not align, a conclusive determination cannot be made.

1.5 Delimitations

The following section aims to establish the boundaries and limits of the thesis project to clearly define what falls outside its scope. Due to time constraints, this project only includes offline identification of machine parameters through machine excitation with test signals while at a standstill, and not the online techniques, which instead require tracking the parameters during operation. These last techniques result in a more advanced study of the topic because they take into consideration the effects of the environment, such as temperature changes, on the drive system during work time. An offline procedure allows to have a first picture of motor parameters.

Furthermore, due to time constraints, only the electrical parameters of the machine's equivalent circuit are estimated in this study, while the mechanical parameters are not addressed.

Another limit is due to the available equipment in the laboratory, which restricts the power rating (up to 15 kW) and the types of machines investigated (IM and SPMSM). Higher power ranges cannot be tested due to a lack of corresponding equipment.

Additionally, only the FOC is considered, and no other control techniques, since this is the most sensitive control strategy to parameter variations between those implemented by the company imperix (Direct Torque Control (DTC), scalar voltage-frequency control, and Rotor Field Oriented Control (RFOC)).

Chapter 2

Background knowledge

In this chapter, the dynamic model of the two types of motors is described with their respective equations. The mechanical model is presented in Section 2.1 and the electrical one in Section 2.2.1 for the SPMSM and in Section 2.2.2 for the IM. Specific focus on the inverter and its effects on the self-commissioning methods is in Section 2.4. Subsequently, the theoretical background on the control strategies for motor drives is given in Section 2.5, specifically, the principle of RFOC in Section 2.5.1.

2.1 Mechanical Dynamic Model of Motor Drives

The dynamic model of an electric motor drive can be divided into electrical dynamic and mechanical dynamic. These are studied, following the reference [6]. The mechanical torque τ_m is the input of the mechanical Equation (2.1),

$$J\frac{d\omega_m}{dt} = \tau_m - b_f\omega_m - \tau_L \tag{2.1}$$

where J is the inertia of the electric drive, b_f is the friction coefficient, τ_L is the load torque.

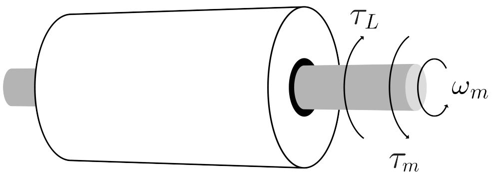

Figure 2.1: Rotating motor physics.

Specifically, the Imperix electric drive is a dual motor testbench, composed of two electrical machines coupled through the same shaft. One of the units performs as a motor/generator (τ_m), while the other unit serves as a variable load (τ_L). More details about the testbench are provided in Section 5.3.

2.2 Machine Electrical Dynamic Model

2.2.1 Permanent Magnet Synchronous Machine (PMSM)

In this section, the background theory necessary for the SPMSM parameter identification is explained. First, the general equation for the Permanent Magnet Synchronous Machine (PMSM) are defined, than they are particularized for the SPMSM. First, the ideal PMSM model is described under the following hypotheses, following the literature by A. Cavagnino [7]:

- no magnetic saturation;
- stator windings with theoretical sinusoidal distribution;
- no spatial harmonics in the Magneto Motive Force (MMF) and magnetic field distributions.

and the following conventions are used:

- motor conventions for supply voltages and currents;
- anti-clockwise sequence order of the stator winding triad;
- quadrature axis of rotor 90° in advance of direct axis.

Later in the analysis, the saturation effect is introduced in the model in Section 2.3. In the three-phase abc reference frame, the electrical and magnetic vector equations are defined in Equation (2.2).

$$\begin{aligned} \mathbf{v}_s - R_s\mathbf{i}_s - \frac{d\boldsymbol{\psi}_s}{dt} = 0 \\ \boldsymbol{\psi}_s = L_s\mathbf{i}_s + \boldsymbol{\psi}_r \end{aligned} \tag{2.2}$$

where

$$\mathbf{v}_s = \begin{vmatrix} v_{sa} \\ v_{sb} \\ v_{sc} \end{vmatrix} ; \quad \mathbf{i}_s = \begin{vmatrix} i_{sa} \\ i_{sb} \\ i_{sc} \end{vmatrix} ; \quad \boldsymbol{\psi}_s = \begin{vmatrix} \psi_{sa} \\ \psi_{sb} \\ \psi_{sc} \end{vmatrix} \tag{2.3}$$

The subscript 's' and 'r' identify the stator and rotor quantities, and the subscript indicates the phase of the reference frame. The three-phase reference frame is introduced because it is used for the single-phase configuration by L. Peretti in [8].

Subsequently, the electrical Equation (2.2) is transformed into the two-phase model $\alpha\beta 0$ in Equation (2.5), thanks to the transformation matrix in Equation (2.4), where x is a generic electric or magnetic quantity (v, i or ψ).

$$\mathbf{x}_s^s = \begin{bmatrix} x_{s\alpha} \\ x_{s\beta} \\ x_{s0} \end{bmatrix} = \frac{2}{3} \cdot \begin{bmatrix} 1 & -1/2 & -1/2 \\ 0 & \sqrt{3}/2 & -\sqrt{3}/2 \\ 1/2 & 1/2 & 1/2 \end{bmatrix} \cdot \begin{bmatrix} x_{sa} \\ x_{sb} \\ x_{sc} \end{bmatrix} \tag{2.4}$$

Equation (2.5) is represented with the equivalent circuit in the $\alpha\beta 0$ stationary reference frame in Figure 2.2. It models the electrical behavior of the stator because the PMSM is supplied from the stator side. Indeed, the Permanent Magnets (PM) are on the rotor side. The stator circuit is composed of the stator resistance R_s (representing the copper losses) in series with the synchronous inductance L_s (equivalent inductance of self-inductance and mutual-inductance) and with a voltage source, that represents the back-Electromagnetic Force (EMF) $\mathbf{E}^s$ induced in the stator windings by the rotor magnetic field.

$$\begin{aligned} \mathbf{v}_s^s - R_s\mathbf{i}_s^s - \frac{d\boldsymbol{\psi}_s^s}{dt} = 0 \\ \boldsymbol{\psi}_s^s = L_s\mathbf{i}_s^s + \boldsymbol{\psi}_r^s \end{aligned} \tag{2.5}$$

where $\boldsymbol{\psi}_r^s = \psi_r^s e^{j\theta}$ is the rotor flux linkage, which is produced by the permanent magnets.

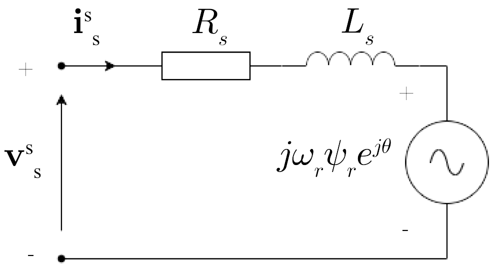

Figure 2.2: Synchronous machine dynamic vector equivalent circuit in the $\alpha\beta 0$ stationary reference frame.

The derivative of the flux $\boldsymbol{\psi}_s^s$ in Equation (2.5) is:

$$\frac{d\boldsymbol{\psi}_s^s}{dt} = L_s \frac{d\mathbf{i}_s^s}{dt} + j\omega_e \psi_r^s e^{j\theta} \tag{2.6}$$

Substituting Equation (2.6) in Equation (2.5),

$$L_s \frac{d\mathbf{i}_s^s}{dt} = \mathbf{v}_s^s - R_s \mathbf{i}_s^s - \underbrace{j\omega_e \psi_r^s e^{j\theta}}_{\mathbf{E}^s} \tag{2.7}$$

θ is the phase of the rotor flux $\boldsymbol{\psi}_r^s$ and the synchronous angle θ_e is the angle between the α-axis and the d-axis, (which time derivative is the synchronous speed ω_e). Figure 2.3 clarifies the reference frame definition.

In perfect field-oriented conditions, the actual flux angle θ and the synchronous coordinate system used in the dq0 transformation θ_e are equal. In other words, the d-axis of the rotor should overlap the rotor flux linkage $\boldsymbol{\psi}_r^s$. Moreover, since the slip in the SPMSM is null, the synchronous position θ_e corresponds to the rotor position θ_r.

$$\theta = \theta_e = \theta_r \tag{2.8}$$

The $\alpha\beta 0$ reference frame is rotated at the angle θ_e, through the complex exponential in Equation (2.9), where $\omega_e = \frac{d\theta_e}{dt}$.

$$\mathbf{x}^{dq0} = e^{-j\omega_e t}\mathbf{x}^s \tag{2.9}$$

Substituting Equation (2.9) in Equation (2.7) in perfect field orientation

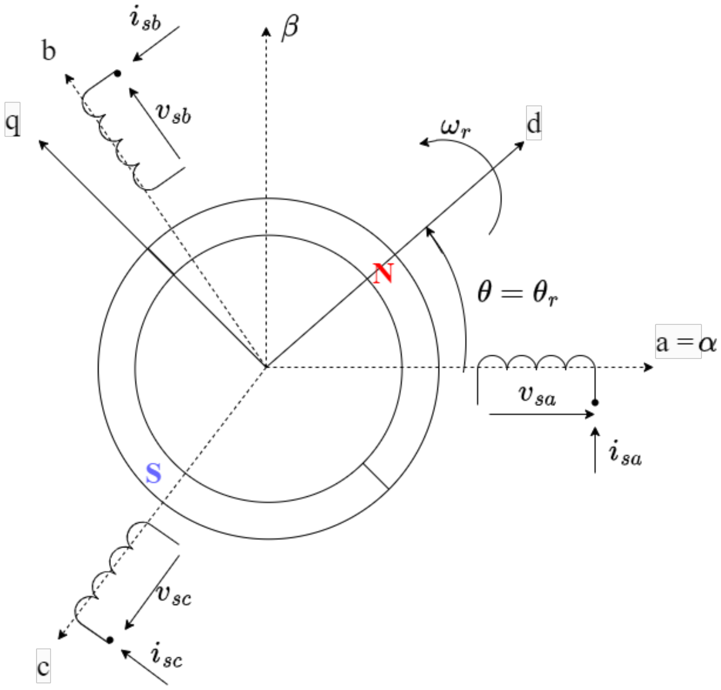

Figure 2.3: Reference frame definition for SPMSM.

results in Equation (2.10).

$$L_s \frac{d\left(e^{j\theta_e}\mathbf{i}_s^{dq0}\right)}{dt} = e^{j\theta_e}\mathbf{v}_s^{dq0} - R_s e^{j\theta_e}\mathbf{i}_s^{dq0} - j\omega_e\psi_r \tag{2.10}$$

Simplifying the notation, the electrical dynamic is transformed to dq0 synchronous coordinates in Equation (2.11) in matrix form.

$$\boldsymbol{L}_s \frac{d\boldsymbol{i}_s^{dq0}}{dt} = \mathbf{v}_s^{dq0} - \left(R_s\boldsymbol{I} + \boldsymbol{J}\omega_e L_s\right)\boldsymbol{i}_s^{dq0} - \boldsymbol{J}\omega_e\boldsymbol{\psi}_r \tag{2.11}$$

where,

$$\boldsymbol{L}_s = \begin{bmatrix} L_d & 0 \\ 0 & L_q \end{bmatrix}, \quad \boldsymbol{I} = \begin{bmatrix} 1 & 0 \\ 0 & 1 \end{bmatrix}, \quad \boldsymbol{J} = \begin{bmatrix} 0 & -1 \\ 1 & 0 \end{bmatrix}, \quad \boldsymbol{\psi}_r = \begin{bmatrix} \psi_r \\ 0 \end{bmatrix} \tag{2.12}$$

Subsequently, the voltage equations are written in component form, whose equivalent circuit is given in Figure 2.4.

$$
\begin{aligned}
L_d \frac{di_{s,d}}{dt} &= v_{s,d} - R_s i_{s,d} + \omega_e L_q i_{s,q} \\
L_q \frac{di_{s,q}}{dt} &= v_{s,q} - R_s i_{s,q} - \omega_e \left(L_d i_{s,d} + \psi_r \right)
\end{aligned}
\tag{2.13}
$$

The SPMSM is assumed isotropic, which is reflected in the condition Equation (2.14).

$$
L_d \approx L_q = L_s \tag{2.14}
$$

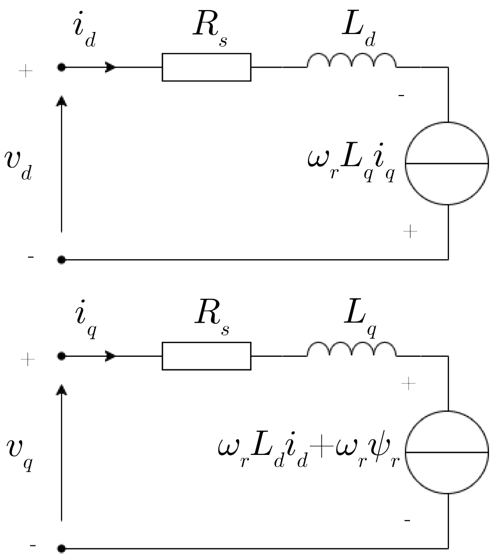

Figure 2.4: Dynamic equivalent circuit for the PMSM in d and q axis.

In steady-state the time derivative is null, so the steady-state equations for the SPMSM are given in Equation (2.15). This circuit is used for the self-commissioning procedure from Chapter 3.

$$
\begin{aligned}
v_{s,d} &= R_s i_{s,d} - \omega_e L_s i_{s,q} \\
v_{s,q} &= R_s i_{s,q} + \omega_e \left(L_s i_{s,d} + \psi_r \right)
\end{aligned}
\tag{2.15}
$$

To complete the model of the PMSM, the mechanical torque τ_m is calculated through the vector product of flux and current vectors, solved in Equation (2.16).

$$
\tau_m = \frac{3n_p}{2K^2} \left[\psi_r i_{s,q} + \left(L_{s,d} - L_{s,q} \right) i_{s,d} i_{s,q} \right] \tag{2.16}
$$

where n_p are the pole pairs and K is the scaling constant equal to 1 for peak-value scaling, $\frac{1}{\sqrt{(2)}}$ for Root Mean Square (RMS)-value scaling, and $\sqrt{(\frac{3}{2})}$ for power-invariant scaling. The only contribution of torque in a SPMSM comes from the PM. The reluctant torque $\frac{3n_p}{2K^2}\left(L_{s,d} - L_{s,q}\right) i_{s,d} i_{s,q}$ is canceled since the reluctance all around the rotor circumference is assumed constant. In conclusion, substituting Equation (2.14) in Equation (2.16) results in Equation (2.17).

$$\tau_m = \frac{3n_p}{2K^2}\psi_r i_{s,q} \tag{2.17}$$

2.2.2 Induction Machine (IM)

First, the IM circuit from the standard 112-2017 [3] is introduced in Figure 2.5. Subsequently, the demonstration and the different types of IM electrical circuits useful for the self-commissioning algorithm are presented.

The parameters in the T-circuit model the physical behavior of the IM. R_s is the stator winding resistance representing the copper losses. L_{ls} is the total stator leakage inductance that includes all the effects of slot leakage, tooth tip leakage, end-winding leakage, leakage due to harmonics, slot skewing leakage, and pole leakage. The rotor quantities are referred to the stator side. R_r is the rotor resistance which models the copper losses in the winding resistance in the case of wound rotor induction motor and rotor bars' resistance for squirrel cage rotor. L_{lr} is the leakage inductance attributed to flux leakage due to rotor slots, slot skewing, and harmonics. The middle branch consists of a magnetizing inductance L_m, in parallel with the core loss equivalent resistance R_{Fe} (in this case neglected). L_m represents the fundamental harmonic of the rotating magnetic field at the polarity n_p. [2].

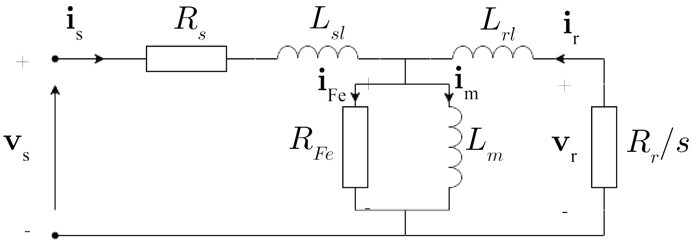

Figure 2.5: Steady-state vector T-equivalent circuit of a squirrel cage IM from the standard 112-2017 [3].

The ideal model is described by following the hypotheses from the reference in [2]:

- no magnetic saturation, so constant inductance;
- stator and rotor windings (and so MMF) with theoretical sinusoidal distribution;
- perfectly isotropic (slot openings neglected);
- perfectly cylindrical rotor with no saliencies;
- perfect stator and rotor laminations, which result in null eddy currents;
- hysteresis effects neglected in both stator and rotor;
- the magnetic flux lines always cross the air gap radially.

Later in the analysis, the saturation effect is introduced in the model in Section 2.3.

$$\begin{aligned} \mathbf{v}_s &= R_s \mathbf{i}_s + \frac{d\boldsymbol{\psi}_s}{dt} \\ \mathbf{v}_r &= R_r \mathbf{i}_r + \frac{d\boldsymbol{\psi}_r}{dt} \end{aligned} \tag{2.18}$$

where

$$\mathbf{v}_s = \begin{vmatrix} v_{sa} \\ v_{sb} \\ v_{sc} \end{vmatrix} ; \quad \mathbf{i}_s = \begin{vmatrix} i_{sa} \\ i_{sb} \\ i_{sc} \end{vmatrix} ; \quad \boldsymbol{\psi}_s = \begin{vmatrix} \psi_{sa} \\ \psi_{sb} \\ \psi_{sc} \end{vmatrix} \tag{2.19}$$

$$\mathbf{v}_r = \begin{vmatrix} v_{ra} \\ v_{rb} \\ v_{rc} \end{vmatrix} ; \quad \mathbf{i}_r = \begin{vmatrix} i_{ra} \\ i_{rb} \\ i_{rc} \end{vmatrix} ; \quad \boldsymbol{\psi}_r = \begin{vmatrix} \psi_{ra} \\ \psi_{rb} \\ \psi_{rc} \end{vmatrix} \tag{2.20}$$

In matrix form, the model of the IM is:

$$\begin{aligned} \begin{bmatrix} v_{sa} \\ v_{sb} \\ v_{sc} \end{bmatrix} &= \begin{bmatrix} R_s & 0 & 0 \\ 0 & R_s & 0 \\ 0 & 0 & R_s \end{bmatrix} \cdot \begin{bmatrix} i_{sa} \\ i_{sb} \\ i_{sc} \end{bmatrix} + \frac{d}{dt} \begin{bmatrix} \psi_{sa} \\ \psi_{sb} \\ \psi_{sc} \end{bmatrix} \\ \begin{bmatrix} v_{ra} \\ v_{rb} \\ v_{rc} \end{bmatrix} &= \begin{bmatrix} R_r & 0 & 0 \\ 0 & R_r & 0 \\ 0 & 0 & R_r \end{bmatrix} \cdot \begin{bmatrix} i_{ra} \\ i_{rb} \\ i_{rc} \end{bmatrix} + \frac{d}{dt} \begin{bmatrix} \psi_{ra} \\ \psi_{rb} \\ \psi_{rc} \end{bmatrix} \end{aligned} \tag{2.21}$$

Subsequently, the electrical equation is transformed into the two-phase model thanks to the transformation matrix T.

$$\mathbf{x}_s^s = \begin{bmatrix} x_{s\alpha} \\ x_{s\beta} \\ x_{s0} \end{bmatrix} = \frac{2}{3} \cdot \begin{bmatrix} 1 & -1/2 & -1/2 \\ 0 & \sqrt{3}/2 & -\sqrt{3}/2 \\ 1/2 & 1/2 & 1/2 \end{bmatrix} \cdot \begin{bmatrix} x_{sa} \\ x_{sb} \\ x_{sc} \end{bmatrix} = \mathbf{T}\mathbf{x}_s \tag{2.22}$$

where x is a generic electric or magnetic quantity (v, i or ψ).

Similarly as for the SPMSM in Section 2.2.1, the stator voltage equation in the stator reference frame is given in Equation (2.23)

$$\mathbf{v}_s^s - R_s\mathbf{i}_s^s - \frac{d\boldsymbol{\psi}_s^s}{dt} = 0 \tag{2.23}$$

Unlike the SPMSM in which the rotor is only characterized by the PM, the rotor in a IM has short-circuited windings or squirrel cage. For this reason, the rotor voltage equation in the rotor reference frame is given in Equation (2.24).

$$\mathbf{v}_r^r - R_r\mathbf{i}_r^r - \frac{d\boldsymbol{\psi}_r^r}{dt} = 0 \tag{2.24}$$

There are two different reference frames: the $\alpha_s\beta_s0_s$ stator reference frame fixed to the stator in Equation (2.23), indicated with the superscript ”s”; the $\alpha_r\beta_r0_r$ rotor reference frame fixed to the rotor in Equation (2.24), indicated with the superscript ”r”. To simplify the notation, all the electrical quantities are referred to one reference frame. The rotor equation is transformed to the stationary reference frame, so the rotor space vectors are rotated at an angle equal to the rotor position with respect to the stationary reference frame θ_r.

The position is

$$\begin{aligned} \mathbf{i}_r^s &= e^{j\theta_r}\mathbf{i}_r^r \\ \boldsymbol{\psi}_r^s &= e^{j\theta_r}\boldsymbol{\psi}_r^r \end{aligned} \tag{2.25}$$

The reference frames of the IM are shown in Figure 2.6 (which is an original hand-drawn representation like all the figures in this report).

Substituting Equation (2.25) in the Equation (2.24) and assuming $\mathbf{v}_r^r = 0$ since the rotor windings are short-circuited, Equation (2.26) is found.

$$\begin{aligned} 0 - R_r e^{-j\theta_r}\mathbf{i}_r^s - \frac{d\left(e^{-j\theta_r}\boldsymbol{\psi}_r^s\right)}{dt} &= 0 \\ \Rightarrow -R_r e^{-j\theta_r}\mathbf{i}_r^s - \left(-j\omega_r e^{-j\theta_r}\boldsymbol{\psi}_r^s + e^{-j\theta_r}\frac{d\boldsymbol{\psi}_r^s}{dt}\right) &= 0 \\ \Rightarrow j\omega_r\boldsymbol{\psi}_r^s - R_r\mathbf{i}_r^s - \frac{d\boldsymbol{\psi}_r^s}{dt} &= 0. \end{aligned} \tag{2.26}$$

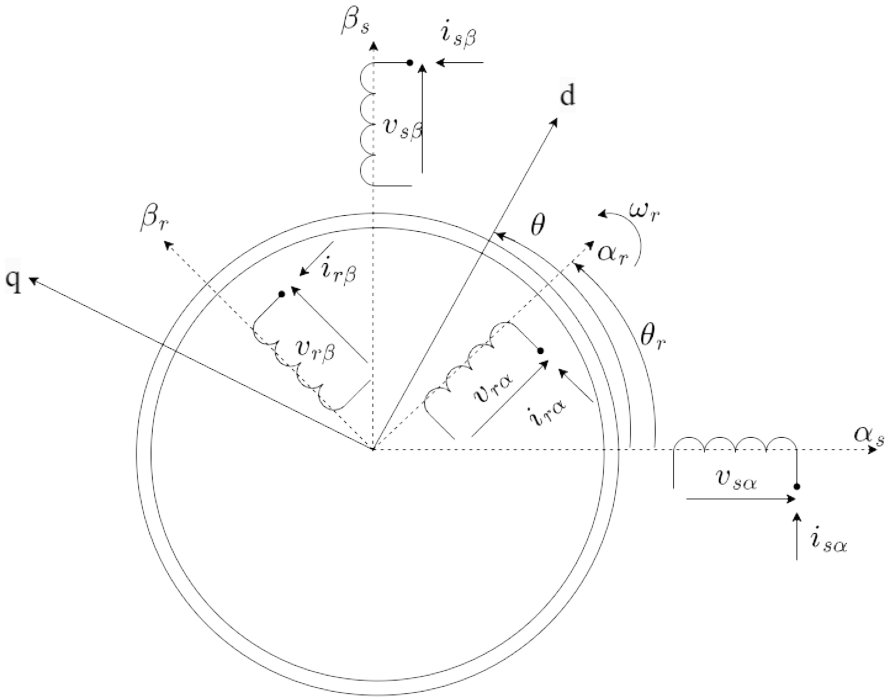

Figure 2.6: Reference frame of the IM.

In conclusion, the voltage equations of the IM in the $\alpha_s\beta_s0_s$ stator reference frame are:

$$\begin{aligned} \frac{d\boldsymbol{\psi}_s^s}{dt} &= \mathbf{v}_s^s - R_s\mathbf{i}_s^s \\ \frac{d\boldsymbol{\psi}_r^s}{dt} &= j\omega_r\boldsymbol{\psi}_r^s - R_r\mathbf{i}_r^s \end{aligned} \tag{2.27}$$

Subsequently, the magnetic equations are specified. The airgap flux $\boldsymbol{\psi}_a^s$ is related to the magnetizing inductance L_m:

$$\boldsymbol{\psi}_a^s = L_m\mathbf{i}_m^s, \tag{2.28}$$

where

$$\mathbf{i}_m^s = \mathbf{i}_s^s + \mathbf{i}_r^s \tag{2.29}$$

The stator flux $\boldsymbol{\psi}_s^s$ and the rotor flux $\boldsymbol{\psi}_r^s$ in $\alpha\beta0$ stator reference frame are

$$\begin{aligned} \boldsymbol{\psi}_s^s &= L_m\mathbf{i}_m^s + L_{sl}\mathbf{i}_s^s \\ \boldsymbol{\psi}_r^s &= L_m\mathbf{i}_m^s + L_{rl}\mathbf{i}_r^s \end{aligned} \tag{2.30}$$

Substituting Equation (2.30) in Equation (2.27) the T-circuit equations are found

$$\begin{aligned} \mathbf{v}_s^s - R_s\mathbf{i}_s^s - L_{sl}\frac{d\mathbf{i}_s^s}{dt} - L_m\frac{d\mathbf{i}_m^s}{dt} = 0 \\ j\omega_r\boldsymbol{\psi}_r^s - R_r\mathbf{i}_r^s - L_{rl}\frac{d\mathbf{i}_r^s}{dt} - L_m\frac{d\mathbf{i}_m^s}{dt} = 0 \end{aligned} \tag{2.31}$$

Although the T-equivalent dynamic model is physically relevant, this circuit is not used for the control because it is over-parametrized. In fact, due to Equation (2.29), the three currents ($\mathbf{i}_m^s, \mathbf{i}_s^s, \mathbf{i}_r^s$) are not linearly independent. For this reason, the circuit can be further simplified by considering one total leakage inductance.

Substituting Equation (2.29) in Equation (2.28), the flux in Equation (2.30) can be rewritten as:

$$\begin{aligned} \boldsymbol{\psi}_s^s = L_s\mathbf{i}_s^s + L_m\mathbf{i}_r^s \\ \boldsymbol{\psi}_r^s = L_m\mathbf{i}_s^s + L_r\mathbf{i}_r^r \end{aligned} \tag{2.32}$$

where,

$$\begin{aligned} L_s = L_m + L_{sl} \\ L_r = L_m + L_{rl} \end{aligned} \tag{2.33}$$

The inverse-Γ equivalent circuit is relevant for the control of the machine. Its parameters are estimated in this work, but as explained before, they do not have a physical meaning. From the T-circuit, the equations for the inverse-Γ equivalent circuit are derived with the position in Equation (2.34),

$$\begin{aligned} \boldsymbol{\psi}_R^s = b\boldsymbol{\psi}_r^s \\ \mathbf{i}_R^s = \frac{\mathbf{i}_r^s}{b} \end{aligned} \tag{2.34}$$

where b is a transformation factor to be chosen.

$$\begin{aligned} \boldsymbol{\psi}_s^s = L_s\mathbf{i}_s^s + bL_m\mathbf{i}_R^s \\ \boldsymbol{\psi}_r^s = bL_m\mathbf{i}_s^s + b^2L_r\mathbf{i}_R^s \end{aligned} \tag{2.35}$$

By choosing b such that the stator and rotor currents have equal coefficients in Equation (2.35) with the rotor quantities,i.e., $bL_m = b^2L_r$ $b = L_m/L_r$, the leakage inductance on the rotor side is eliminated.

$$\begin{aligned} \boldsymbol{\psi}_s^s = L_s\mathbf{i}_s^s + \frac{L_m^2}{L_r}\mathbf{i}_R^s \\ \boldsymbol{\psi}_r^s = \frac{L_m^2}{L_r}\left(\mathbf{i}_s^s + \mathbf{i}_R^s\right) \end{aligned} \tag{2.36}$$

where

$$
\begin{aligned}
L_M &= \frac{L_m^2}{L_r} \\
L_\sigma &= L_s - L_M = L_s - \frac{L_m^2}{L_r} = \frac{L_m\left(L_{sl} + L_{rl} + L_{sl}L_{rl}\right)}{L_m L_{rl}} \approx L_{sl} + L_{rl}
\end{aligned}
\tag{2.37}
$$

$$
\begin{aligned}
\boldsymbol{\psi}_s^s &= L_\sigma \mathbf{i}_s^s + L_M \mathbf{i}_M^s \\
\boldsymbol{\psi}_r^s &= L_M \mathbf{i}_M^s
\end{aligned}
\tag{2.38}
$$

The transformed rotor resistance is:

$$
R_R = \left(\frac{L_m}{L_r}\right)^2 R_r \tag{2.39}
$$

Substituting Equation (2.38) in Equation (2.27) the inverse Γ-circuit equations are found

$$
\begin{aligned}
\mathbf{v}_s^s - R_s\mathbf{i}_s^s - L_\sigma \frac{d\mathbf{i}_s^s}{dt} - L_M \frac{d\mathbf{i}_M^s}{dt} &= 0 \\
j\omega_r \boldsymbol{\psi}_R^s - R_R \mathbf{i}_R^s - L_M \frac{d\mathbf{i}_M^s}{dt} &= 0
\end{aligned}
\tag{2.40}
$$

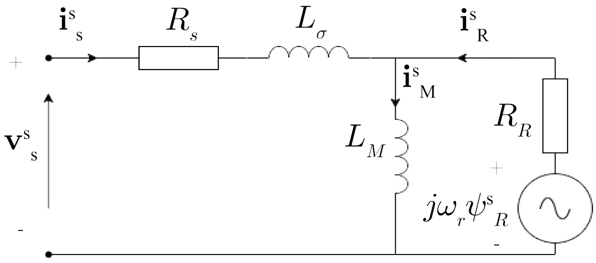

Figure 2.7: Dynamic inverse-Γ equivalent circuit described by Equation (2.40).

Since the control for common electric drives is generally implemented on the stator side of the machine, one state variable is the stator current $\mathbf{i}_s^s$. In fact, the control loop can instead involve rotor currents in particular application such as the the control of a Doubly-Fed Induction Generator (DFIG).

Moreover, in most of the applications, the rotor circuit is not accessible in the case of an IM since it is not externally supplied. For this reason, the measurements of the the rotor currents are not easily available. The rotor flux

$\boldsymbol{\psi}_R^s$ is chosen as the second state variable, following the equation:

$$\mathbf{i}_R^s = \mathbf{i}_M^s - \mathbf{i}_s^s = \frac{\boldsymbol{\psi}_R^s}{L_M} - \mathbf{i}_s^s \tag{2.41}$$

Substituting Equation (2.41) in Equation (2.40), Equation (2.42) is found.

$$\begin{aligned} L_\sigma \frac{d\mathbf{i}_s^s}{dt} &= \mathbf{v}_s^s - R_s\mathbf{i}_s^s - \underbrace{\frac{d\boldsymbol{\psi}_R^s}{dt}}_{\mathbf{E}^s} \\ \frac{d\boldsymbol{\psi}_R^s}{dt} &= R_R\mathbf{i}_s^s - \left(\frac{R_R}{L_M} - j\omega_r\right)\boldsymbol{\psi}_R^s \end{aligned} \tag{2.42}$$

In conclusion:

$$L_\sigma \frac{d\mathbf{i}_s^s}{dt} = \mathbf{v}_s^s - (R_s + R_R)\,\mathbf{i}_s^s - \left(j\omega_r - \frac{R_R}{L_M}\right)\boldsymbol{\psi}_R^s \tag{2.43}$$

Subsequently, Equation (2.42) is transformed into the dq0 synchronous reference frame by rotating the $\alpha_s\beta_s0_s$ reference frame at the synchronization angle θ_e.

$$L_\sigma \frac{d\mathbf{i}_s^{dq0}}{dt} = \mathbf{v}_s^{dq0} - (R_s + j\omega_e L_\sigma)\,\mathbf{i}_s^{dq0} - j\omega_e\boldsymbol{\psi}_R^{dq0} - \frac{d\boldsymbol{\psi}_R^{dq0}}{dt} \tag{2.44}$$

$$\frac{d\boldsymbol{\psi}_R^{dq0}}{dt} = R_R\mathbf{i}_s^{dq0} - \left(\frac{R_R}{L_M} + j\omega_{slip}\right)\boldsymbol{\psi}_R^{dq0} \tag{2.45}$$

where the slip angular speed is $\omega_{slip} = \omega_e - \omega_r = s\omega_e$ and s is the slip.

Finally, the dynamic of the IM is completed with the electromagnetic torque expression in Equation (2.46).

$$\tau_m = \frac{3n_p}{2K^2}\left(\psi_{s,d}i_{s,q} - \psi_{s,q}i_{s,d}\right) \tag{2.46}$$

2.3 Magnetic saturation

When the inductance estimation is performed, its behavior in saturation conditions is studied. The theory in this section is used for the DC+AC method. The reference [8] proposes to study the magnetically saturated machines modelling them as generic inductors, which follows Equation (2.47).

$$v(t) = \frac{d\psi(i(t))}{dt} \tag{2.47}$$

where v, i are the voltage and current in the bipole, and $\psi(i(t))$ indicates the magnetic flux linkage as function of the current. The instantaneous flux linkage is expressed as function of the instantaneous current by Equation (2.48),

$$\psi(i(t)) = L_a(i(t))i(t) \tag{2.48}$$

in which the apparent inductance L_a is function of the current only. Subsequently Equation (2.48) is substituted in Equation (2.47) and the flux derivative is developed.

$$\begin{aligned} v(t) &= \frac{d\psi(i(t))}{dt} = \frac{d\left(L_a(i(t))i(t)\right)}{dt} = \\ &= \left[L_a(i(t)) + i(t)\frac{dL_a(i(t))}{di(t)}\right]\frac{di(t)}{dt} = \\ &= \left[L_a(i(t)) + L_d(i(t))\right]\frac{di(t)}{dt} = \\ &= L(i)\frac{di(t)}{dt} \end{aligned} \tag{2.49}$$

From Equation (2.49), the instantaneous inductance $L(i)$ is the sum of two terms, the apparent inductance L_a and the differential inductance $L_d = i(t)\frac{dL_a(i(t))}{di(t)}$, which graphical interpretation is given in Figure 2.8.

$$L(i) = L_a(i) + i(t)\frac{dL_a(i)}{di} \tag{2.50}$$

The instantaneous inductance $L(i)$ represents the actual inductance around the operating point ($i_{dc}; \psi_{dc}$) and it expresses the derivative of the flux linkage to the current in that point.

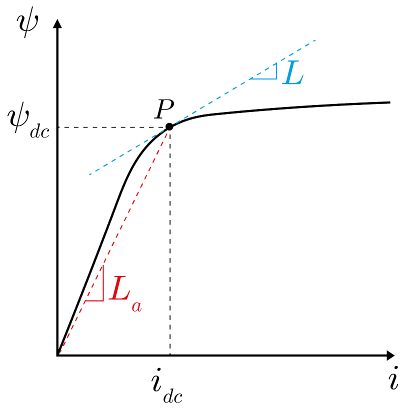

Figure 2.8: Graphical interpretation of L and L_a.

2.4 Inverter non-linearity

Self-commissioning involves the utilization of an inverter for the regulation of voltage waveforms injected into an electrical machine. The presence of the inverter introduces a discrepancy between the reference voltage, administered by the controller, and the voltage received at the machine terminal. Non-idealities, as elucidated by Shafiq [2], encompass:

- the threshold voltage of semiconductor switches, enabling the switch to enter the conduction state.
- the on-state resistance of semiconductor switches, indicative of the voltage drop during operation once the switch is in the conduction state.
- the dead-time [9]. A converter leg consists of two semiconductor devices arranged in series. In an ideal switch, the switching moments are defined by the intersection of the control voltage and the carrier waveform. However, real switches have turn-on (t_{on}) and turn-off (t_{off}) durations, as illustrated in Figure 2.9. Specifically, t_{f} is the fall time, t_{r} is the rise time. They represent the time employed by the switch to go from a state on ($90\% V_{ds}$) to a state off ($10\% V_{ds}$), and vice versa. $t_{\text{d,on}}$ is the turn-on time and $t_{\text{d,off}}$ is the turn-off time, which corresponds to the time employed by the gate signal to be applied on the drain source.

$$\begin{aligned} t_{\text{on}} &= t_{\text{d,on}} + t_{\text{r}} \\ t_{\text{off}} &= t_{\text{d,off}} + t_{\text{f}} \end{aligned} \tag{2.51}$$

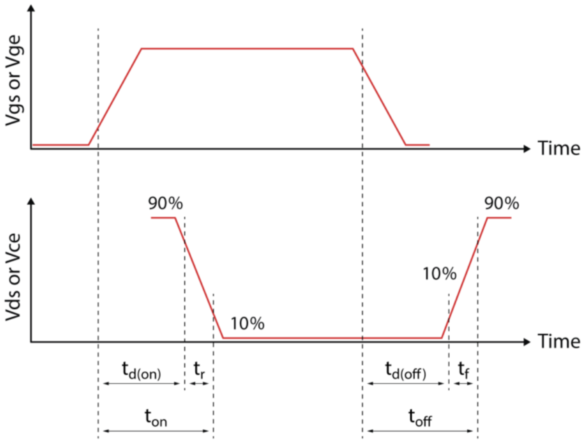

Figure 2.9: Switching delays of a power semiconductor.

To avoid “shoot through” or cross-conduction current through the leg, the dead time $t_\triangle$ is introduced. This is done by delaying the turn-on control input of one transistor to the turn-off control input of the other transistor in the inverter leg, as shown in Figure 2.10. The dead time is conservatively chosen to be greater than the worst-case maximum storage time of the transistors. This dead time introduces an unwanted non-linearity in the converter transfer characteristic.

During the dead time, both the switches are off. The inverter output voltage is not controlled by the switching signals but it depends on the direction of the phase current [10]. The difference between the ideal and the actual output voltage is:

$$v_{ph}^{err} = v_{ph}^{ref} - v_{ph}^{actual} \tag{2.52}$$

By averaging v_{ph}^{err} over one time period of the switching frequency in Figure 2.10, the change (defined as a drop if positive) in the output voltage due to $t_\triangle$ is obtained:

$$\Delta V_{ph} = \begin{cases} +\frac{t_\triangle}{T_s} V_{DC} & i_{ph} > 0 \\ -\frac{t_\triangle}{T_s} V_{DC} & i_{ph} < 0 \end{cases} \tag{2.53}$$

ΔV_{ph} does not depend on the magnitude of the current but its polarity depends on the direction of the current.

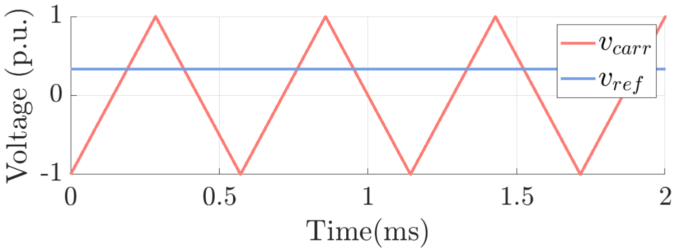

(a) Carrier and reference voltage.

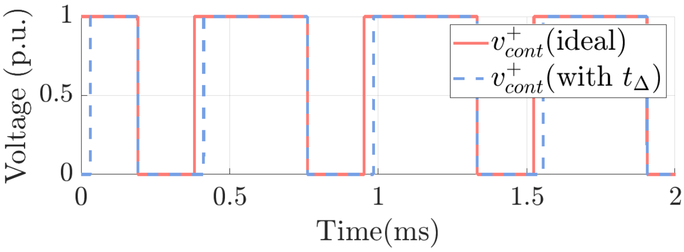

(b) Control voltage of the positive switch of the inverter leg ($i_{ph} > 0$).

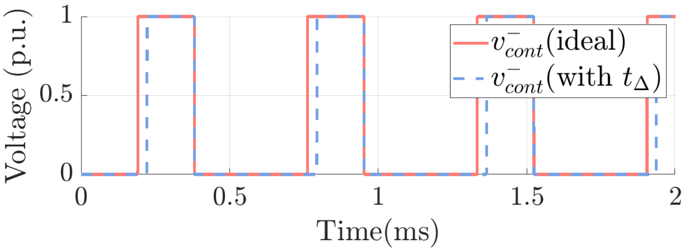

(c) Control voltage of the negative switch of the inverter leg ($i_{ph} < 0$).

Figure 2.10: Effect of blanking time t_Δ.

The self-commissioning procedure is performed at a standstill. For this reason, it involves very low values of voltage and currents, (for instance around 1% of the rated voltage).With such low voltages, the inverter non-linearity effects influence the estimate of the machine parameters. This problem could be solved by adding voltage sensors at the output of the inverter. On the other side, due to the fourth constraint of the self-commissioning definition given in Section 1.5, the procedure is performed using the available sensors, which are the stator currents sensors and the DC voltage sensor. No further voltage sensors are introduced in the system. Indeed, the measurement of the output voltage of the converter results in a switched waveform, which should be processed to extract its fundamental harmonic. For this reason, the voltage sensor is not a practical choice in a self-commissioning procedure. The phase voltages can be then reconstructed by knowing the switch command from the output of the controller and the DC voltage, but an accurate compensation of the inverter non-linearity needs to be performed, as explained in Section 3.2.1.

2.5 Control strategies

2.5.1 Rotor Field Oriented Control (RFOC)

The company Imperix provides the Simulink file for the RFOC of an IM, explained in the knowledge base section [11].

The system model of the RFOC is shown in Figure 2.11.

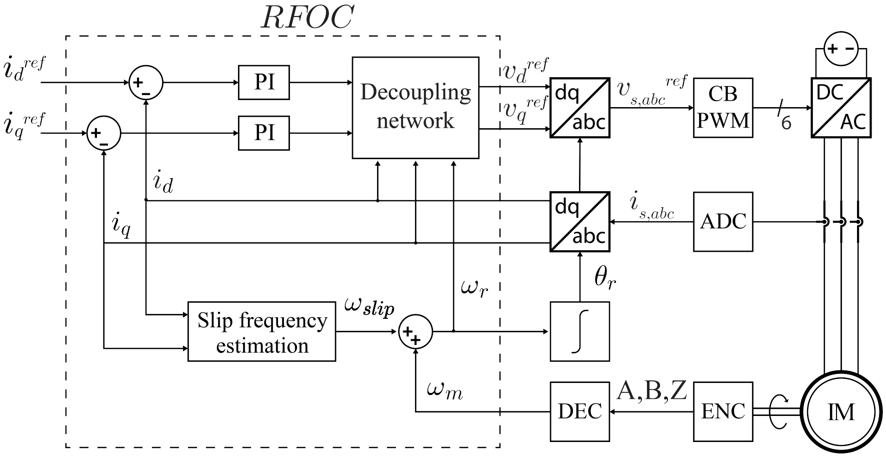

Figure 2.11: Rotor Field-Oriented Control block diagram.

Expressing the Equation (2.45) in components form and assuming perfect field orientation, namely $\theta = \arg \boldsymbol{\psi}_R$ and $\boldsymbol{\psi}_R = \psi_R$, the equations become:

$$\begin{aligned} \frac{d\psi_R}{dt} &= R_R i_{sd} - \frac{R_R}{L_M}\psi_R \\ \omega_{slip} &= \omega_e - \omega_r = \frac{R_R i_{sq}}{\psi_R}. \end{aligned} \tag{2.54}$$

In steady-state, i_{sd} is called the flux-producing current component and should be controlled such that

$$i_{sd} = \frac{\psi_{\text{ref}}}{L_M} \tag{2.55}$$

In the case of perfect field orientation, the flux had only a d-component and the q-component is zero ($\boldsymbol{\psi}_R = \psi_R = \psi_{s,d}$). Hence, the torque equation in Equation (2.46) is simplified as in Equation (2.56).

$$\tau_m = \frac{3n_p}{2K^2}\psi_R i_{s,q} \tag{2.56}$$

So $i_{s,q}$ is called the torque-producing current component and it is controlled to have the desired electromagnetic torque $i_{s,q} = \frac{2K^2\tau_m^{ref}}{3n_p\psi_R}$.

To control constant currents in the dq0 reference frame, the Proportional Integral (PI) Current Controller (CC) are used.

2.5.1.1 Current controller (CC)

In this subsection, the tuning of the CC is explained. First, the d and q axes of Equation (2.44) are decoupled by adding the corresponding compensation terms. The rotor flux is assumed constant, so its time derivative is zero, $\frac{d\boldsymbol{\psi}_R^{dq0}}{dt} = 0$. As a result, the plant system can be modeled as a resistive-inductive impedance in dq0 reference frame in Equation (2.57).

$$L_\sigma \frac{d\mathbf{i}_s^{dq0}}{dt} = \mathbf{v}_s^{dq0} - R_s\mathbf{i}_s^{dq0} \tag{2.57}$$

The transfer function corresponding to Equation (2.57) is given in Equation (2.58). Because of the isotropic nature of the IM, the transfer function is the same in both the d and q axes.

$$H_d(s) = H_q(s) = \frac{I_s(s)}{V_s(s)} = \frac{1/R_s}{1 + sL_\sigma/R_s} = \frac{K_1}{1 + sT_1} \tag{2.58}$$

This type of transfer function in Equation (2.58) allows the use of the magnitude optimum criterion from the reference [12] for the tuning of the PI CC. The CC parameters are set as follows:

$$\begin{aligned} T_n &= T_1 \\ T_i &= 2K_1T_d \\ K_p &= T_n/T_i \\ K_i &= 1/T_i \end{aligned} \tag{2.59}$$

where T_d is the sum of all system delays:

- sensing delay $T_{d,sense}$, due to finite sensor and analog chain bandwidth, and possibly filtering delay;

- control delay, $T_{d,ctrl}$, due to sampling instant and duty-cycle update instant in the PWM modulator (FPGA peripheral);
- modulator delay, $T_{d,PWM}$, average delay between duty-cycle update in the PWM modulator and the resulting change in modulator output;
- switching delay $T_{d,tran}$, between change in the modulator output to actual switching of the power device (can often be neglected).

In conclusion, the controller proportional and integral gains (K_p, K_i) rely on the estimation of the machine parameter (R_s, L_σ). These gains affect the performance of the FOC technique.

Chapter 3

Theory of self-commissioning

The purpose of this chapter is to provide a theoretical overview of the self-commissioning methodologies. After the literature review in Section 3.1, some of the available solutions between those proposed from the state of the art are implemented first for the SPMSM and then for the IM in Section 3.2 and in Section 3.3, respectively.

3.1 Methodological classification

This section provides essential background information concerning parameter identification methods, highlighting their evolution and the diverse techniques developed over time. Primarily, these methods fall into two main categories: offline identification and online identification. The former involves performing identification with the machine at a standstill, and subsequently analyzing the parameters in post-processing. Conversely, the latter entails estimating parameters during normal machine operation, with updates made routinely.

Given the extensive range of parameter identification methods, various criteria can be employed to classify them. For instance, the Ph.D. Dissertation in [2] distinguishes between standstill identification and techniques allowing shaft rotation, with coupling with the load or necessitating rotor locking. In particular, this dissertation serves as one of the main references for this degree project. An updated classification was introduced in 2019 in [4], categorizing the main methods into four groups:

- numerical analysis tools, related to Finite Element Analysis (FEA), difficult to develop in an industrial environment where the geometrical design is not available;

- shaft rotation thanks to a prime mover;
- standstill identification (which includes self-commissioning);
- free shaft rotation.

Signal injection under defined conditions is utilized in this project and it is discussed in the following subsections. However, other potential methods include algebraic algorithms and machine learning approaches. In particular, the latest are predominantly for online identification methods. For instance, a Kalman-filter-based algorithm [13] was tested on an Interior Permanent Magnet Synchronous Machine (IPMSM), while Adaptive Linear Neuron (ADALINE) networks were explored in [14] for the IM.

Most papers on self-commissioning procedures compare methods using either FEA simulations ([8], [15], [16]) or the traditional tests outlined by IEEE ([17], [18]). In this project, the FEA simulations are not used as a benchmark due to the lack of knowledge regarding the machine's geometrical design, so the IEEE standards are chosen. However, the traditional tests provide information mainly on the rated and unsaturated values of the machine, lacking depth in evaluating saturation behavior. Nevertheless, saturation behavior can be integrated into control algorithms using a Lookup Table (LUT). This integration enables the dynamic adjustment of gains, potentially enhancing control performance. For this reason, the methodologies under study also investigate parameters under saturation conditions, even though they cannot be directly compared to the corresponding FEA simulations.

3.1.1 Literature review of parameter identification methods for SPMSM

In this section, the literature that pertains to the SPMSM for offline self-commissioning and standard IEEE 1812-2023 tests in [5] is discussed.

The electrical parameters are the focus of this project. However, some references provide the mechanical parameter estimation like [19], [20].

Already existing methods, developed for other machines, are tested on the SPMSM since the literature on this machine is not as vast as for others, like the IM, Synchronous Reluctance Machines (SynRM).

From Figure 2.2, the SPMSM parameters studied are:

- stator resistance;
- synchronous inductance;

- PM-flux.

In all the references in this subsection, the compensation of inverter non-linearity is exploited.

The methods tested in this work on the SPMSM are summarized in Table 3.7.

3.1.1.1 SPMSM stator resistance

To estimate the stator resistance, a DC test is performed. This technique is widely acknowledged across literature concerning electrical machines, not just for the SPMSM, as also observed for the IM in Section 3.1.2.1.

The references are classified in Table 3.1 based on:

- signal injected;
- control configuration, namely closed or open loop;
- output, i.e., the result extracted from that procedure;
- need for inverter non-linearity compensation to estimate R_s.

First, the Open Loop (OL) procedures are analyzed. [21] uses one-level DC voltage in OL in the stationary reference frame. However, it requires prior identification of inverter non-linearity. Also [8] uses an OL, but in a single-phase configuration. Originally tested on the IM, this study extends its application to the SPMSM. It extracts the stator resistance after identifying the phase voltage-phase current characteristic. Consequently, utilizing the same signal injection, both stator resistance estimation and LUT for inverter non-linearity compensation are achieved. For these reasons, the method in [8] is implemented in this project.

Similarly, the effect of inverter non-linearity can be identified with multiple steps of DC current injected through a CC in a single-phase configuration as in [22], [23], tested on a linear PMSM. The test can be conducted in a closed loop configuration injecting one-level or two-level DC currents as demonstrated in [2]. While the first approach necessitates non-linearity compensation to estimate the stator resistance, the second one does not. However, further DC injection is required to identify the voltage error due to the inverter. Additionally, CC tuning must be performed before starting the self-commissioning procedure. Nevertheless, the procedures outlined in [2] and [8] are developed in this project to analyze the impact of the closed or open loop implementation on the stator resistance estimate.

Another method discussed in [19] identifies the stator resistance from the same sinusoidal signal used to estimate the inductance. However, the skin and proximity effects could increase the resistance value to its DC value. Consequently, this method is not tested in this project.

The drawback of these offline procedures is that none consider thermal drift, relevant during the machine operation, especially for the resistance estimation. The stator resistance is a critical parameter for control performance.

A benchmark for these procedures is the measured stator resistance defined by the standard IEEE 1812-2023 [5].

Table 3.1: Literature overview for IM stator resistance offline self-commissioning identification

References	Signal injected	Control configuration	Output	need of LUT to estimate R_s
[2], [22]	Two-level DC current	with CC	R_s estimate	No
[22]	Multiple-level DC voltage	with CC	LUT for non-linearity compensation	No
[2]	One-level DC current	with CC	R_s estimate	Yes
[21]	One-level DC voltage	OL	R_s estimate	Yes
[21]	Multiple-level DC voltage	OL	LUT for non-linearity compensation	No
[8] (adapted)	Multiple-level DC voltage	OL	R_s estimate and LUT for non-linearity compensation	No
[19]	AC voltage	OL	R_s estimate	Yes

3.1.1.2 SPMSM synchronous inductance

The references are classified in Table 3.2 based on:

- signal injected;
- control configuration, namely closed or open loop;
- analysis of saturation behavior by plotting the corresponding characteristic (yes if considered or no if not).

One methodology for identifying synchronous inductance relies on sinusoidal AC injection. However, variations exist in implementation methods.

[2] proposes a high-frequency signal injection (AC method) thanks to a Proportional Resonant (PR) CC, with which the unsaturated value is identified in this work.

Similarly, [24] utilizes AC voltage injection at rated frequency, yielding only simulation results without considering saturation or non-idealities, making it unsuitable for implementation.

In [21], a DC bias is incorporated into the signal to mitigate inverter non-linearity, despite its compensation. However, this adjustment alters the machine's saturation state, resulting in a value that diverges from the unsaturated value and therefore cannot be directly compared to the chosen benchmark, the Standard IEEE test. This reference does not take into account saturation.

[8] introduces a modified approach using OL single-phase DC+AC method. In this project, this method is adapted for the SPMSM by modifying it in a closed-loop configuration. DC steps are superimposed on the AC signal. Adjusting the DC set point enables variation in the machine's saturation state, thereby designing the saturation characteristic synchronous inductance-current. This procedure is implemented in this project.

An alternative to the sinusoidal signal injection is proposed in [25]. This procedure tracks the flux-current saturation characteristic through hysteresis control. This method has also been applied in several other works, including [26], [27], [28], [29], [30], and [31]. Initially developed for SynRM, this procedure applies to PM machines (tested on the IPMSM but not on the SPMSM).

In conclusion, this work estimates synchronous inductance following [2], [8], [25]. These three procedures are chosen to highlight the difference in machine behavior under saturation and linear conditions. This selection aims to develop the saturation characteristic as said at the beginning of Section 3.1. The benchmark for the synchronous inductance estimate is the short circuit test from the standard IEEE 1812-2023 [5], which returns the unsaturated value.

Table 3.2: Literature overview for SPMSM synchronous inductance offline self-commissioning identification

References	Signal injected	Control configuration	Saturation characteristic
[2]	high frequency AC current	with CC	Yes
[24]	rated frequency DC+AC current	with CC	No
[21]	DC+AC voltage	OL	No
[8]	DC+AC voltage	OL	Yes
[25], [26], [27], [28], [29], [30], [31]	square-wave voltage	with hysteresis control	Yes

3.1.1.3 SPMSM PM-flux

The last parameter for estimation is the PM-flux. This estimation process typically falls into two main categories: quasi-steady-state and shaft rotation procedures.

Different methods have been devised to enable minimal rotation of the rotor shaft. One such method, described in [2], involves controlling the machine speed to zero through a Speed Controller (SC) and exploiting its anisotropy under saturation conditions. However, this method requires accurate saturation characteristics in the d and q axes, difficult to obtain in a mostly isotropic machine. Additionally, the SC must be tuned even when mechanical parameters are neither estimated nor calculated.

Another method is [32] that determines the PM-flux linkage based on minimum saliency tracking with minimal rotor movement. While this method has been tested on PM-assisted SynRM, its application to SPMSM remains unexplored, presenting a potential avenue for future investigation. However, this procedure relies on the saturation of the SynRM bridges, and the saturation effect may differ in the case of SPMSM.

A viable approach for PM-flux identification involves accelerating the SPMSM in OL up to a certain speed and subsequently transitioning to sensorless FOC with zero current references. Since the machine is accelerated, the constraints of the self-commissioning procedure in Section 1.5 are not entirely respected. However, this solution offers a reasonable compromise between the self-commissioning method and the implementation time and it is widely used in the literature.

PM-flux estimation allowing shaft movement is also addressed in [19] and [23]. A benchmark for the PM-flux estimate is the open-circuit test in [5], which also relies on the machine speed.

3.1.2 Literature review of parameter identification methods for IM

This section delves into the literature concerning offline self-commissioning for IM and standard IEEE 112-2017 tests.

The IM parameters, referred to the inverse-Γ equivalent circuit in Figure 2.7 and investigated in this project, include:

- stator resistance;
- stator leakage inductance;
- rotor resistance referred to the stator side.

Although the literature review for the magnetizing inductance is addressed in Section 3.1.2.4, the associated methods are not developed in simulation or experiment due to time constraints. In all the listed references in this subsection tested on an experimental setup, the effect of the inverter non-linearity is taken into account for the reference voltage correction.

The methods analyzed in this study for the IM are summarized in Table 3.8.

3.1.2.1 IM stator resistance

As already stated for the SPMSM in Section 3.1.1.1, the stator resistance is estimated by letting a direct current flow in the machine winding. While this base principle is common to all the references in the literature, the implementation is achieved in several ways. The references are classified in Table 3.3 based on:

- signal injected;
- control configuration, namely closed or open loop;
- output, that is the results extracted from that procedure;
- need for inverter non-linearity compensation to estimate R_s.

One of the early references employing signal injection from a Pulse Width Modulation (PWM) inverter is [33] from 1988. Similarly, [1], published in 1990, lays the groundwork for self-commissioning of the IM.

In [8], an OL procedure is performed, wherein the stator resistance is extracted from the characteristic phase voltage-phase current using a Linear least-squares (LLS). This method not only allows the determination of the stator resistance but also identifies the LUT utilized in the control algorithm for compensating for inverter non-linearity from the same injected signal. Unlike other methods, this procedure does not require tuning of the CC, which is a more time-consuming approach than the OL schemes. Seeing the importance of time for industrial applications, the OL configurations are favored, if possible, and if safety is ensured. Additionally, the stator resistance can be estimated without prior knowledge of voltage errors attributable to inverter non-linearity.

Another possible solution is proposed in [1], [33], [34], [16], [23] and [2]. Two levels of DC current are considered, so no compensation of inverter non-linearity is needed to estimate R_s. However, there is the need to tune the CC. Moreover, this procedure estimates just the stator resistance but not the voltage drop due to the inverter, necessary for the following parameter estimation. Hence, the LUT identification has to be performed in sequence with the R_s estimate as in [16] and [23]. In these last two references, the LUT is identified as performing multiple DC steps in closed loop.

Another proposal is found in the literature. If just one level of DC current is forced through the CC ([35], [2]), the inverter non-linearity is compensated by introducing a LUT. However, this LUT is identified with a procedure as in [8] before starting the self-commissioning routine and the CC has to be tuned.

Despite the results presented in [8] being more efficient in terms of time consumption and result assessment, this project incorporates all three methods. This decision aims to evaluate the impact of both open-loop and closed-loop procedures on resistance estimation, as well as to examine the influence of inverter non-linearity across various injection levels.

A benchmark for the chosen self-commissioning procedures is the stator resistance measurement as suggested by the standard IEEE 112-2017 [3].

Apart from the DC injection and the measurements through a multimeter, there are no other methods presented in the literature that can be used to identify the stator resistance.

Table 3.3: Literature overview for IM stator resistance offline self-commissioning identification

References	Signal injected	Control configuration	Output	need of LUT to estimate R_s
[1], [33], [34], [2], [23], [16]	Two-level DC current	with CC	R_s estimate	No
[35], [2]	One-level DC current	with CC	R_s estimate	Yes
[8], [10]	Multiple-level DC voltage	OL	R_s estimate and LUT for non-linearity compensation	No

3.1.2.2 IM leakage inductance

The references are categorized in Table 3.4 according to the following criteria:

- signal injected;
- control configuration, namely closed or open loop;
- analysis of the influence of frequency by plotting the corresponding characteristic (yes if considered or no if not);
- analysis of saturation behavior by plotting the corresponding characteristic (yes if considered or no if not).

[1] has been one of the widely developed methods in the literature for the stator transient inductance, as shown in [33], [35], [18], [2]. This procedure is based on appropriate short-voltage impulses. Moreover [2] proposes different variations based on the number of impulses and adapting it for low-reactance machines by switching to a closed-loop procedure instead of the traditional open-loop approach. However, using voltage impulses provides just one value and not a description of the saturation behavior, which is of interest in this work, as said at the beginning of Section 3.1.

[36] proposes an identification in closed-loop of the leakage inductance using the T equivalent circuit. Hence, the leakage inductance of the stator is separated from that of the rotor. The first one is estimated with a high-frequency current injection and the low-frequency test is performed to find the rotor leakage inductance. This procedure takes into account the influence of current distribution variation due to different frequencies, not considered in this project. However, it does not provide insight into the saturation behavior of the leakage inductance.

The influence of the frequency on the leakage inductance is studied in [37] through sine-wave excitations in sequence. However, even in this reference, a solution for the saturation characteristic is not proposed.

[2] tests the procedure proposed by [37] but considers just one frequency set point. It does not further develop this method by introducing the study of saturation effects.

[16] follows the same method of two sinusoidal current signals in sequence in [37] but in this case, a DC bias is introduced. The change of the DC component in the signal injected leads to a modification of the saturation state, as already seen in Section 3.1.1.2. The self-saturation characteristic is then built. Even though this represents a possible path, this method could be further simplified by considering just one injection frequency and changing the data post-processing.

Therefore, [8] is analyzed. Similarly to [16], [8] uses DC+AC voltage signals through a single-phase configuration, but in OL, bypassing the need for CC tuning. This method provides insights into the saturation behavior of the leakage inductance. Due to its comprehensive and simple nature, this last method has been selected for implementation in this study.

However, the saturation study could be further deepened. [15] studies the saturation characteristic of the leakage inductance as a function of two variables: the stator flux and the leakage flux. It uses explicit functions to model the mutual saturation, validating it through experimental results. This procedure is also applied for the magnetizing inductance, as explained in Section 3.1.2.4. However, the experimental tests are performed at different rotor speeds in steady state and transient state. For this reason, the constraints imposed by the self-commissioning definition are not respected and this procedure is set aside.

In this project, there is no information available about the saturation behavior of the machine. Hence it has been chosen to focus solely on the self-saturation of the inductance as a first analysis.

A benchmark for the chosen self-commissioning procedure is the locked rotor test from the standard IEEE 112-2017 [3], from which the unsaturated leakage inductance is found.

Table 3.4: Literature overview for IM leakage inductance offline self-commissioning identification

References	Signal injected	Control configuration	Frequency dependent characteristic	Saturation characteristic
[1], [33], [35], [18], [2]	short voltage impulses	OL	No	No
[2]	current ramp	with CC	No	No
[36]	low and high frequency DC+AC current	with CC	Yes	No
[37]	AC voltage	with CC	Yes	No
[16]	DC+AC current	with CC	No	Yes
[8]	DC+AC voltage	OL	No	Yes

3.1.2.3 IM rotor resistance

The references are classified in Table 3.5 based on:

- signal injected;
- control configuration, namely closed or open loop;
- analysis of the frequency influence by plotting the corresponding characteristic (yes if considered or no if not);
- analysis of the current influence by plotting the corresponding characteristic (yes if considered or no if not).

The self-commissioning procedures for rotor resistance identification involve:

- DC step through a CC. While [33], [35], and [2] present the experimental results, [1] mainly presents the theory. However, the accuracy of this method relies on the tuning of the CC, which is based on parameters that still need to be estimated. For instance, if the tuning of the CC is too aggressive there are high overshoot of the reference voltage that could lead to inaccuracy of the parameter estimate.
- two DC-biased sine-wave excitations in sequence with different frequencies in a binary configuration [16]. In addition to the other references, [16] provides the characteristics of the rotor resistance as a function of the DC current. [37] tests this method on the three different configurations of the IM equivalent circuit (T, Γ, inverse-Γ) varying the

frequency. These frequency-dependent characteristics allow the study of the skin effect. [2] also tests experimentally this method. This procedure is useful for the estimation of all the IM equivalent circuit parameters apart from the stator resistance.

The frequency-dependent and the current-dependent characteristics contribute to machine knowledge at a standstill. However, they do not represent a valuable contribution to the enhancement of control performance. Since the resistance is mostly sensitive to temperature variations, an online procedure is suggested to improve the control performance. In this study, the focus of the rotor resistance identification is related to its identification around rated working conditions.

- Low-frequency AC single-phase injection. The literature proposes different variations of these tests. [2] and [8] introduce a DC bias in the low-frequency AC signal to mitigate inverter non-linearity, in contrast to [18]. On the other side, [8] and [18] favor an OL procedure, differently from [2]. [18] present just the simulation results, instead, [2] and [8] validate the method on an experimental setup. The method exposed in [8] is developed in this project because it allows to avoid the need for CC tuning. Moreover, it has been validated on an experimental setup. Additionally, [8] illustrates the trend of rotor resistance varying the slip frequency (in this project just one set point is considered). The frequency characteristic is studied also from other references. For instance, a deeper analysis of this method is presented in [36], which takes into account the influence of the frequency characteristic of the rotor bars. Moreover, it uses a CC for a DC-biased sinusoidal injection. A further contribution results from [36] because of the proposed offline commissioning for phase delay compensation due to the drive, which significantly affects estimation precision.

A benchmark for the chosen self-commissioning procedures is the locked rotor test from the standard IEEE 112-2017 [3].

Table 3.5: Literature overview for IM rotor resistance offline self-commissioning identification

References	Signal injected	Control configuration	Frequency dependent characteristic	Current dependent characteristic
[1], [33], [35], [2]	DC step	with CC	No	No
[2]	low-frequency DC+AC current	with CC	No	No
[8], [36]	low-frequency DC+AC voltage	OL	Yes	No
[16]	DC+AC current at two frequencies	with CC	No	Yes
[37]	DC+AC current at two frequencies	with CC	Yes	No
[2]	DC+AC current at two frequencies	with CC	No	No

3.1.2.4 IM magnetizing inductance

The common element between all the techniques validated on an experimental setup listed in this subsubsection is the compensation for the inverter non-linearity. As seen for the leakage inductance in Section 3.1.2.2, the magnetizing characteristic based on the current variations is interesting from a controller point of view and it is an object of study in this project.

The references are classified in Table 3.6 based on:

- signal injected;
- control configuration, namely closed or open loop;
- analysis of the frequency influence by plotting the corresponding characteristic (yes if considered or no if not);
- analysis of the saturation effect by plotting the corresponding characteristic (yes if considered or no if not).

In [1], the magnetizing inductance of the inverse-Γ equivalent circuit is found knowing the rotor resistance and the rotor time constant. While [1] provides theoretical insight, [2] tests it on the experimental setup but [2] does not provide an estimate for the magnetizing inductance and it just gives insight for the rotor time constant. The rotor time constant is estimated from a single phase excitation through CC of the stator. The signal switches to a DC current equal to the reference value of the rotor flux-producing current component. However, this current value is obtained from the no-load test, which has to be performed before the self-commissioning procedure, violating the constraints. For this reason, this procedure is not adopted.

Variations of this method are then proposed in [2]. It tests two iterative methods based on both a sinusoidal current as well as a DC current injected through CC.

The iterative procedures until here listed do not track the magnetizing characteristic but just one value of magnetizing current is considered. These methods are suitable for control in which the machine works at constant rotor flux. This condition is not verified in the flux-weakening range for instance.

A widely tested method is proposed by [18]. It extracts the magnetizing inductance using the same single-phase low-frequency AC test used for the rotor resistance with an OL procedure. Since it is based on simulation, the non-idealities are not considered, such as compensation of voltage error due to inverter and saturation. For this reason it is not developed in this project.

However, the traditional single-phase test gives an error as described in [38]. The inherent error above the rated saturation level comes from the fact that the static magnetizing inductance is alternating in a wide range. A direct numerical integration method is proposed to effectively correct the differential inductance effect. Moreover, this is one of the procedures that allow for building the magnetizing characteristic. In [38] the DC bias is introduced in the traditional AC injection in single phase configuration to change the saturation state of the machine. The injection current signal is regulated through a CC.

However, some methods identify the magnetizing characteristic through a single-phase test with CC without any DC bias, varying just the amplitude of the sinusoidal reference signal, such as in [39].

The traditional sinusoidal single-phase test with or without the DC bias is a possible self-commissioning procedure to be tested in simulation and experiment. However, due to time constraints, this is not done in this project.

Another alternative to develop the magnetizing characteristic in OL instead of in a closed loop is in [17], which proposes a voltage ramp tested on Self-Excited Induction Generator (SEIG). A similar approach, based on a voltage ramp injection in OL is in [16]. However [16] shows that, despite the compensation of inverter non-linearity, this method is sensitive to the voltage error caused by the inverter and the stator resistance estimation.

An alternative to the voltage ramp is a step down for the magnetizing inductance estimation with single-phase OL procedure from [8].This allows tracking the saturation characteristic based on the current amplitude. However, this method requires high accuracy of the voltage measurements to build a good point of comparison for the magnetizing curve. This accuracy is difficult to achieve by recording the measurement from a scope. Other methods for the tracking of the magnetizing curve are the explicit functions like in [15]. It considers the mutual saturation effect. Traditionally the self-saturation effect is modeled as a function of one variable, instead with mutual saturation two variables are considered. The magnetizing inductance may saturate as a function not only of the stator flux but also as a function of the flux leakage. This method allows shaft rotation, hence it is not considered as a self-commissioning procedure.

A benchmark for the chosen self-commissioning procedures is the no-load test from the standard IEEE 112-2017 [3].

Table 3.6: Literature overview for IM magnetizing inductance offline self-commissioning identification

References	Signal injected	Control configuration	Frequency dependent characteristic	Saturation characteristic
[1], [2]	Iterative procedure from τ_r	with CC	No	No
[2]	Iterative procedure from τ_r	OL	No	No
[18]	low-frequency DC+AC current	with CC	No	No
[38]	low-frequency DC+AC current	with CC	No	Yes
[39]	AC current	with CC	No	Yes
[17], [16]	voltage ramp	OL	No	Yes
[8]	step down voltage	OL	No	Yes

3.1.3 Summary

Table 3.7: Identification techniques for SPMSM.

Offline self-commissioning			
Standstill			Shaft Rotation
Parameters	OL	CC	
R_s	multiple levels voltage DC injection. [8]	- one-level DC current injection [2]. - two-level DC current injection [2].	–
L_s	–	- AC current injection [2]. - DC+AC current injection [8]. - hysteresis control [25].	–
ψ_{PM}	–	–	I-f OL startup + sensorless FOC at $\mathbf{i}_s^{ref} = 0$.

IEEE Standard 1812-2023 [5]	
R_s	DC measurement.
L_s	Short circuit test.
ψ_{PM}	Open-circuit test.

Table 3.8: Identification techniques for IM.

Offline self-commissioning			
Standstill			Shaft Rotation
Parameters	OL	CC	
R_s	multiple levels voltage DC injection. [8]	- one-level DC current injection [2]. - two-level DC current injection [2].	–
L_σ	DC+AC voltage injection [8].	–	–
R_R	DC+AC voltage injection [8].	–	–
L_M	–	–	–

IEEE Standard 112-2017 [3]	
R_s	DC measurement.
L_σ	Locked rotor test.
R_R	Locked rotor test.
L_M	No-load test.

3.2 Parameter Estimation for SPMSM

3.2.1 SPMSM stator resistance

Three different methods are used to estimate the resistive part.

1. One-level DC injection.
2. Two-level DC injection.
3. Single phase multiple levels DC voltage injection.

The following considerations are made:

- The estimated resistance (R_s) is not only the resistance of the machine phase, but it also includes the resistance of the entire system, which comprises the machine, cables, and inverter. There is no need to separate the resistance of the machine from the other components of the setup since the CC operates based on the entire system.
- The DC injection is suitable for resistance estimation because the derivative of the constant current during the time is zero, so there is no voltage drop on the inductors and the terminal voltage is equal to the resistive drop.
- The test is at a standstill. As a consequence the rotor speed ω_r, and so the back-EMF, are zero.
- To prevent the generation of torque, a constant current is injected solely in the d-axis ($i_{s,d}$), while the q-axis current remains at zero. Additionally, the voltage of the equivalent circuit terminal in Figure 3.1 represents the reference voltage in the d-axis ($v_{s,d}$), the output of the controller.

Applying these assumptions, the equivalent circuit in the d-axis is drawn in Figure 3.1, because in the q-axis all the quantities are null. The dq0 reference frame is used for the first and second methods. Instead, the abc reference frame is used for the third method.

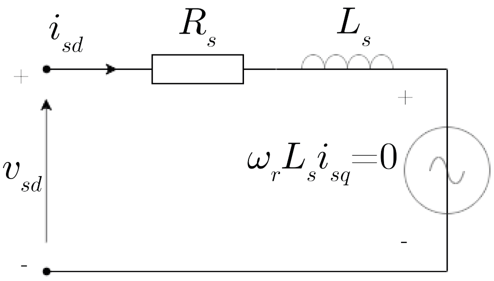

Figure 3.1: Equivalent circuit of the entire system under test in the d-axis for one-level and two-level DC injection.

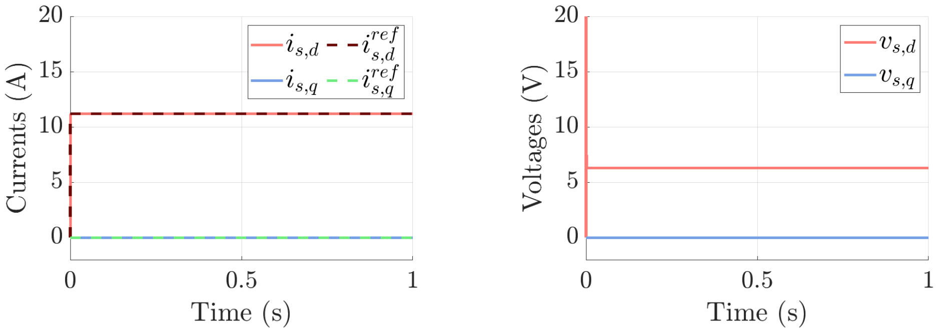

(a) Reference currents.

(b) Output voltages.

Figure 3.2: One-level DC injection with CC, step at 0 s from zero Ampere to the rated value I_{sn}, ideal case, with no dead time simulation, and so, no compensation.

3.2.1.1 One-level DC injection

In the first method [2], the rated current of the machine is injected in the d-axis in Figure 3.2 (a). The voltage output of the CC is recorded as in the simulation in Figure 3.2 (b). The steady-state behavior of the machine is then evaluated.

The voltage equation can be derived from Figure 3.1 to calculate the stator resistance R_s:

$$v_{s,d} = R_s i_{s,d} \Rightarrow R_s = \frac{v_{s,d}}{i_{s,d}} \tag{3.1}$$

For this reason, the nameplate data of the machine has to be known before performing this procedure. Moreover, the current is applied through a CC, which needs to be tuned a priori. It can be tuned manually or, if the parameters are available from the datasheet, with the magnitude optimum criterion, as in this case. On the other side, accurate parameters of the machine are still not available, which can result in a long settling time for the controlled current. For this reason, the time window in which the current step is performed needs to be long enough to allow the current to stabilize. On the other side, if the step lasts too long, for example, more than two minutes, the machine risks heating up, leading to erroneous estimation. To ensure accurate testing, it is necessary to perform the test with the rotor at ambient temperature since the machine parameters are temperature-dependent. The machine should be at rest for a sufficient amount of time to ensure that its windings are also at ambient temperature. However, it is important to note that this work does not take into account the influence of temperature, as stated in Section 1.5.

In this case, to avoid the influence of the CC, the measured current is considered in the calculation, and not the reference one, so that any difference between the two values does not affect the estimation of the machine parameters.

The test is conducted both with and without the inclusion of dead time to assess its impact.

The voltage at the output terminals of the inverter is lower than the reference voltage due to the internal voltage drop (in the simulation caused by the dead time), as explained in Section 2.4. As a consequence, the current rise is slower than the ideal one (see Figure 3.3 (a)). When dead time is integrated into the system, the output voltage of the CC (v_{sd} with t_{Δ}) is higher than the voltage drop on just the resistance of the system (v_{sd} ideal), as depicted in Figure 3.3 (b). The mismatch between the reference voltage and the actual voltage represents a drawback. There are usually no voltage sensors installed at the output of the inverter to measure the actual voltage applied to the stator. For this reason, the output voltage must be estimated from the voltage reference, taking into account the effect of non-linearities, by using the LUT generated with the method in Section 3.2.1.3.

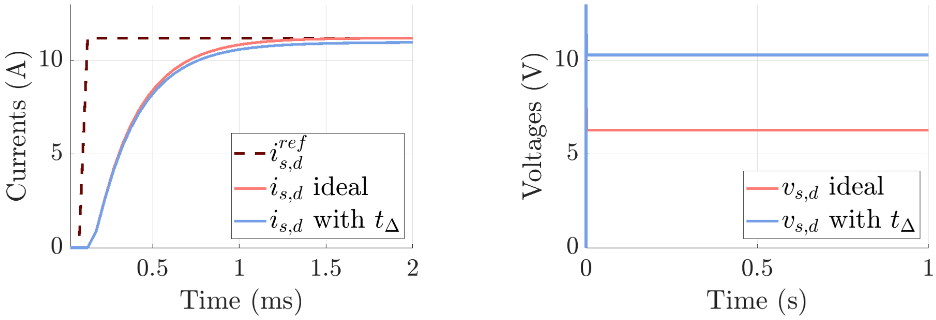

(a) Reference currents.

(b) Output voltages.

Figure 3.3: Effect of simulated dead time t_Δ on control performances in the d-axis.

3.2.1.2 Two-levels DC injection

The second method [2] uses two levels of direct current in the d-axis. The slope of the characteristic voltage-current of the machine represents the stator resistance in the linear region and is computed with the Equation (3.2).

The CC is still used to set the current references, so the considerations regarding it, done for the first case, are still valid. The two-level DC injection method has a drawback in that the selection of set points is random. The choice of the second set point relies on the expert who performs the self-commissioning procedure. The main feature to take in mind is to remain at current levels close to the nominal value to avoid the nonlinear region of the characteristic phase current-phase voltage ($v_{ph}(i_{ph})$) in Figure 3.4. In this work, the first set point $i_{sd,1}$ is half of the rated current and the second one is the rated current $i_{sd,2}$. The simulated signals are shown in Figure 3.5.

$$R_s = \frac{v_{sd,2} - v_{sd,1}}{i_{sd,2} - i_{sd,1}} = \frac{\Delta v_{sd}}{\Delta i_{sd}} \tag{3.2}$$

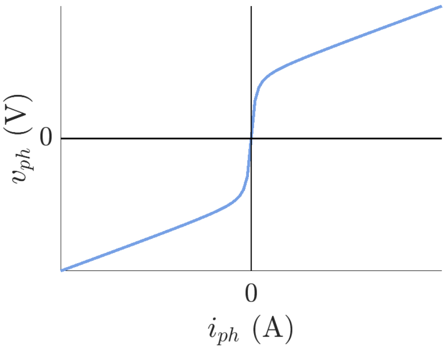

Figure 3.4: Characteristic $i_{ph} - v_{ph}$.

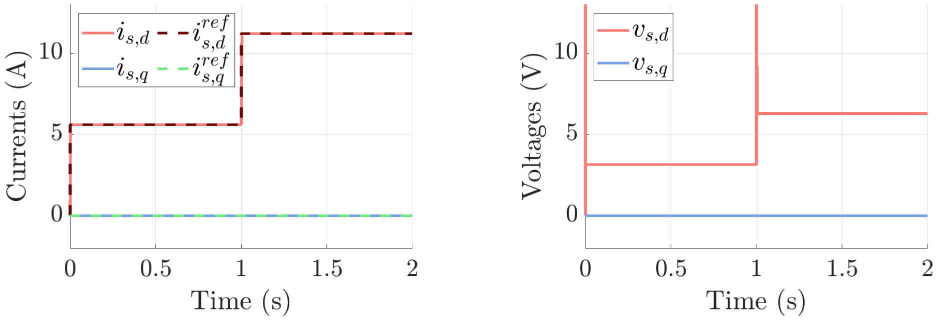

(a) Reference currents.

(b) Output voltages.

Figure 3.5: Two levels DC injection with CC, step at 1 s from $0.5I_{sn}$ to I_{sn}, ideal case, without t_{Δ} simulation.

3.2.1.3 Multiple levels DC injection

This last procedure is performed in [8] and it consists of the characterization of the phase voltage-phase current to identify the inverter non-linearities. This is an OL method, so no CC is used and no tuning of it is done before performing this procedure. A set of reference values of phase voltage is chosen to span the range between zero and the rated phase current of the machine. For this reason, the nameplate data needs to be known as in the previous methods. Per each step of voltage, the phase current is measured, to finally create the map voltage-current of the system under study, similarly as in the example waveform in Figure 3.4.

The maximum phase voltage that can be applied needs to be carefully known to avoid damaging the machine phase. One way is to increase the voltage by small steps until the measured current reaches the rated value.

Another difference to the previous methods is the reference frame of the equivalent circuit. In fact, for the first two cases the calculations are performed in the dq0 reference frame, in this last procedure the abc reference frame is considered.

The goal of this method is to create a single-phase circuit by applying no voltage in phase c, so the voltage in phase a is going to be equal in the module and opposite in sign to that in phase b. The inverter acts as a full-bridge converter. The advantage is that phase c is virtually open, but the physical configuration does not change. This feature makes the procedure feasible for machines placed already on site. The resulting equivalent electrical configuration is shown in Figure 3.6.

$$\begin{aligned} v_{s,b} &= -v_{s,a}, v_{s,c} = 0 \\ i_{s,b} &= -i_{s,a}, i_{s,c} = 0 \end{aligned} \tag{3.3}$$

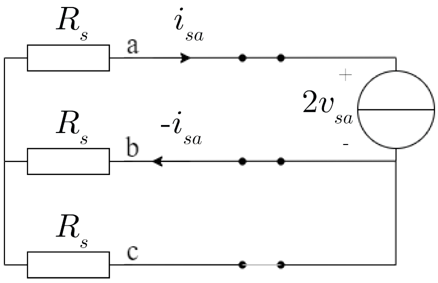

Figure 3.6: Selected single-phase topology for IM voltage supply with phase c ”virtually” opened.

The other element that has to be carefully chosen is the number of voltage steps. The voltage is stepped very finely when the current approaches zero. the steps are wider at higher values of currents. This allows an accurate characterization of the knee of the curve at low currents (see Figure 3.4). Moreover, as for the previous methods, the duration of a step should be long enough (for instance one second) to allow the current to settle per each set point, removing the inductive component. This is also the reason why current steps are chosen to identify the set points and not a current ramp, where the time derivative of the current is not null. As a consequence, the impedance becomes partly inductive.

To further reduce the noise influence on the resistance estimation, a linear least square is performed on the last five samples, making sure to be far enough away from the nonlinear area. The slope of the linearization represents the stator resistance.

The voltage error is due to the difference between the reference phase voltage $v_{s,a}^{ref}$ and the linear component $R_s I_{s,a}$, as in Equation (3.4). If the curve of v_{err} presents some irregularities (for instance due to noise, especially at low currents), a linear least square is performed to maintain the monotonicity.

$$v_{err} = v_{s,a}^{ref} - R_s I_{s,a} \tag{3.4}$$

The v_{err} data are used to build the LUT to compensate for the voltage difference. The LUT takes the current as input and it outputs the voltage error v_{err}. This error is added to the voltage reference $v_{s,a}$, output of the current controller. If the phase current is positive the error is added, if the current is negative it is subtracted. The LUT corrects the three phases a, b, and c.

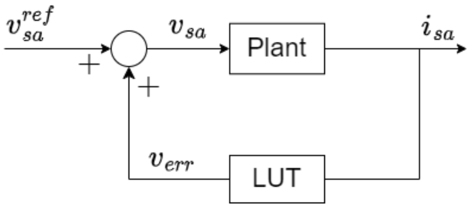

Figure 3.7: Schematic of the inverter non-linearity compensation.

After recording the experimental voltage and current values, the data is averaged within a specified window of observation, in this work arbitrarily one-twentieth of the sampling rate of 20 kHz. In this way, the transient of the voltage step is avoided and just the steady-state behavior is considered. On the other side, the number of samples for the average allows accurate results without requiring big computational efforts from the CPU.

In the final analysis, R_s is estimated from v_{sa}^{ref} and the measured current i_{sa}. Subsequently, v_{err} is computed to construct the LUT. This implies that the LUT is not required specifically for R_s estimation; instead, it proves valuable for other testing purposes.

In this work, the characterization of the inverter is performed before starting the self-commissioning routine. The last presented method is chosen for resistance estimation as it directly extracts resistance from the LUT without applying any further methods.

3.2.2 SPMSM synchronous inductance

3.2.2.1 AC method

The high-frequency injection is used to estimate the impedance of the equivalent circuit in the d-axis. The AC method is based on the reference [2]. A sinusoidal current of known magnitude and known frequency is injected in the d-axis, keeping to zero the q-axis current, as in Equation (3.5).

$$\begin{aligned} i_{sd}^{ref} &= I_{sd,ac}\cos(\omega_h t) \\ i_{sq}^{ref} &= 0 \end{aligned} \tag{3.5}$$

In this way, the rotor is kept in a steady state $\omega_r = 0$, so the equivalent circuit under study is presented in Figure 3.8. The Discrete Fourier Transform (DFT) is used to extract the fundamental voltage and current from the waveform in the d axis ($\dot{v}_{sd}^{fund}$, $\dot{i}_{sd}^{fund}$). According to Kirchhoff's law:

$$\dot{v}_{sd}^{fund} = \dot{Z}_s \dot{i}_{sd}^{fund} \Rightarrow \dot{Z}_s = \frac{\dot{v}_{sd}^{fund}}{\dot{i}_{sd}^{fund}} \tag{3.6}$$

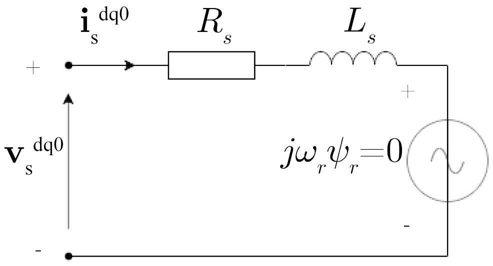

Figure 3.8: Vector equivalent circuit in case of AC injection in dq0 reference frame.

Knowing the circuit impedance $\dot{Z}_s$ and the phase shift between the voltage and the current θ_h, the resistance and the reactance are calculated as projections to the real and imaginary axes. From which the synchronous inductance L_s is known:

$$\begin{aligned} R_s &= |\dot{Z}_s|\cos\theta_h \\ X_s &= |\dot{Z}_s|\sin\theta_h \Rightarrow L_s = \frac{X_s}{2\pi f_h} \end{aligned} \tag{3.7}$$

A PI controller is not able to track a sinusoidal reference. To overcome this problem, a PR is used instead. The PR controller is provided by imperix and it is available in the knowledge base website [40].

Even though this method can estimate both the resistance and the inductance, it is not accurate for the resistance. Skin and proximity effects increase the resistances at high frequency, giving erroneous results for the estimation.

How to choose the injection frequency?
The chosen value should be close to the machine's rated operating. A too-high injection frequency can alter the resistance due to the skin effect of the conductor. This causes a displacement of the test results from the normal operating conditions of the machine. In this work, 300 Hz is arbitrarily chosen.

However, the AC method is only valid in linear work conditions. In case of saturation, linearity is lost and the Thévenin impedance becomes irrelevant due to current distortion. The behavior of the inductance in saturation condition is studied in Section 3.2.2.2.

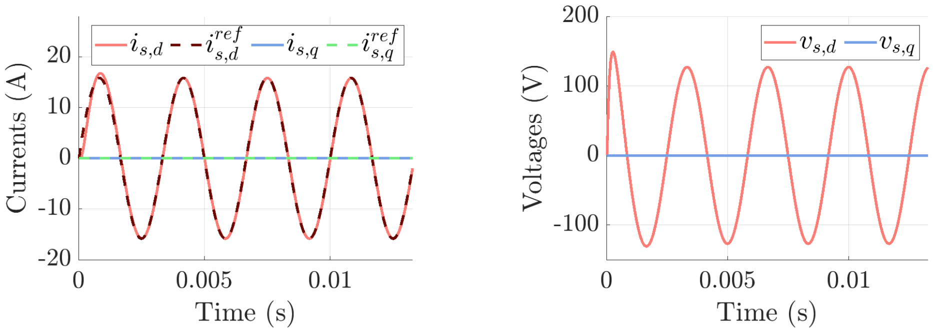

(a) Actual and reference currents.

(b) Reference voltages.

Figure 3.9: Current injection with frequency of 300 Hz in dq0 reference frame, ideal case with no dead time simulation.

3.2.2.2 DC+AC method for SPMSM

The DC+AC injection presented in the reference [8] is based on the theory in Section 2.3. This method was developed for IM, but it can be adapted to synchronous machines. Some differences are applied, for instance, for the IM the method is OL: voltage references are injected and currents are measured. Control is not explicitly applied over the flux vector orientation in synchronous machines operated in OL. For this reason, the current is controlled in a closed loop with a PR controller. Hence, the DC+AC signal is applied in the dq0 reference frame, as in Equation (3.8).

It consists of a small sinusoidal current ($i_{sd,ac}(t)$) superimposed to a predefined set of increasing DC levels ($i_{sd,dc}$) in the d-axis. The q-axis current is kept to zero to avoid torque production and maintain stationary conditions.

$$\begin{aligned} i_{sd}^{ref} &= i_{sd,dc} + i_{sd,ac}(t) = i_{sd,dc} + I_{sd,ac}\cos(\omega_h t) \\ i_{sq}^{ref} &= 0 \end{aligned} \tag{3.8}$$

The DC component is chosen to cover the entire current range based on prior knowledge of R_s, and it establishes the operating point (marked as P in Figure 2.8). The AC signal's low amplitude nature allows for using small-signal theory, assuming linearity around the operating point P. AC voltages and currents are utilized to determine the instantaneous inductance $L_s(i)$. The amplitude ($I_{sd,ac}$) and frequency (f_h) of the current are predetermined and known, while the voltage is obtained from the output of the CC. Moreover, the inverter non-linearity is compensated through the LUT from Section 3.2.1.3, such that the actual phase voltage can be estimated from the reference voltage from the CC. The DFT is used to extract the fundamentals of voltage and current, so the synchronous inductance L_s is calculated as in Equation (3.7).

3.2.2.3 Hysteresis control

The DC+AC method in Section 3.2.2.2 is very sensitive to phase shift error caused by time delays introduced by the PWM and the experimental setup. Furthermore, a good compensation of the inverter non-linearity has to be achieved due to the low voltages. This section aims to analyze a more robust method for estimating the saturation characteristic of SPMSM using hysteresis control. The corresponding reference is N. Bedetti [25].

From Equation (2.13), if the saturation is considered in the model, the inductance is a function of the current and so it is considered inside the flux. The equations are

$$\begin{aligned} v_{sd} &= R_s i_{sd} + \frac{d\psi_{sd}}{dt} - \omega_e \psi_{sq} \\ v_{sq} &= R_s i_{sq} + \frac{d\psi_{sq}}{dt} + \omega_e \psi_{sd} \end{aligned} \tag{3.9}$$

The square wave reference voltage is applied on the d-axis, keeping to zero the voltage in the q-axis, following Equation (3.10) (see Figure 3.11 (a)). Zero q-current results in no torque production and stand-still condition of the machine ($\omega_e = 0$).

$$
\begin{aligned}
v_{\mathrm{d}}^{ref}(t) &= \begin{cases} V_{\mathrm{d}} & \text{if } i_{\mathrm{d}}(t) < -i_{\mathrm{d}}^{\max} \\ -V_{\mathrm{d}} & \text{if } i_{\mathrm{d}}(t) > i_{\mathrm{d}}^{\max} \\ v_{\mathrm{d}}^{ref}(t-1) & \text{otherwise} \end{cases} \\
v_{\mathrm{q}}^{ref}(t) &= 0
\end{aligned}
\tag{3.10}
$$

where V_{d} is the test-voltage magnitude, $i_{\mathrm{d}}^{\max}$ is the current limit.

Applying the assumption of stand-still condition $\omega_e = 0$ to Equation (3.9) and considering just the d-axis circuit, since $v_{\mathrm{q}}^{ref}(t) = 0$, the flux in the d-axis is found from the inverse formula.

$$
\psi_{sd} = \int \left(v_{sd}^{ref} - R_s i_{sd} \right) dt \tag{3.11}
$$

where v_{sd}^{ref} can be approximated to the actual voltage because of the compensation of inverter non-linearity. However, this method results in being more robust than the presented method in Section 3.2.2.2. The high voltages make the procedure less sensitive to errors in the stator resistance estimate and dead-time compensation [27]. The block diagram of the hysteresis control and the voltage integration is shown in Figure 3.10.

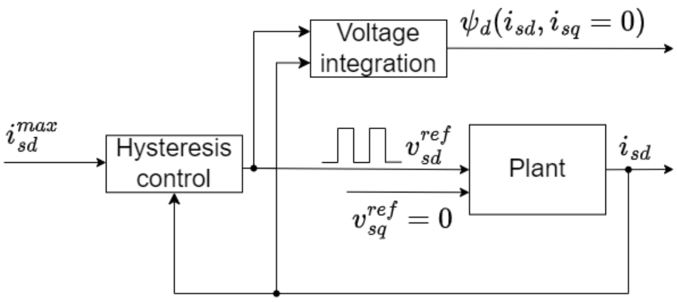

Figure 3.10: Block diagram of the hysteresis controller.

The simulated waveform of the reference voltage, measured current, and estimated flux are shown in Figure 3.11. The saturation of the machine is not simulated, for this reason, the d-axis current waveform has a triangular shape. As a consequence the characteristic (i_{sd}, ψ_{sd}) results in a linear development.

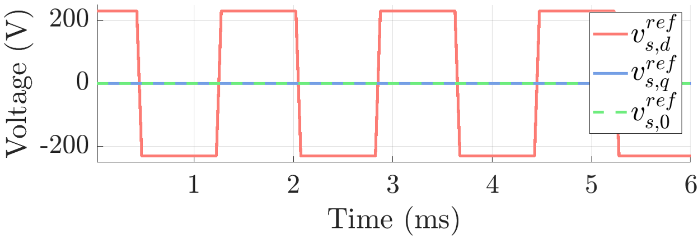

(a) Voltage.

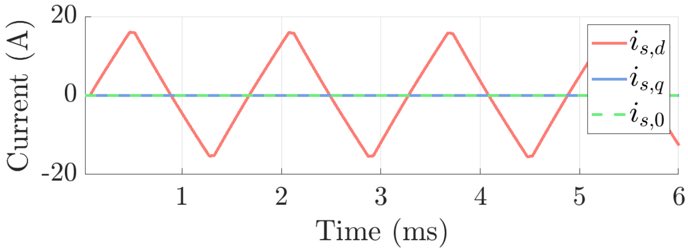

(b) Current.

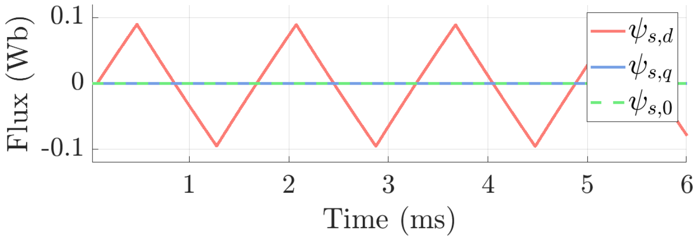

(c) Flux.

Figure 3.11: Hysteresis control simulation waveforms in dq0 reference frame.

From Figure 3.12, the flux and the current are zero at the same moment. A possible problem that can be experienced is not seeing the flux null at the same moment as the current. This offset is a consequence of the drift of the flux integrator. This drift changes with the initial condition in the integrator. The effect of the integrator offset is to translate the saturation characteristic on the y-axis, but the slope of the curve is not affected by this.

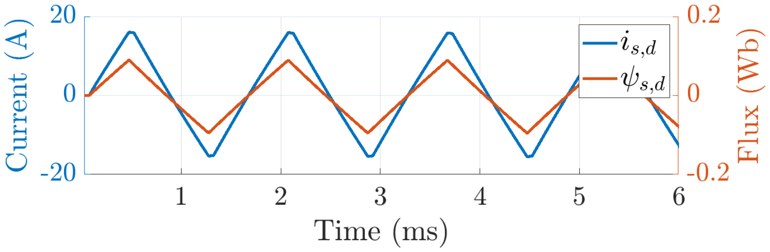

Figure 3.12: Current and flux in the d-axis in hysteresis control simulation.

How can the inductance be extracted from the saturation characteristic? The reference [25] uses Multiple Linear Regression (MLR) for the data post-processing to reduce the computational weight of the algorithm. The method is based on the identification of the slopes of two areas, saturation and linear region. However, MLR applied on the saturation characteristic not as curved as in a SynRM does not provide satisfying results because it is not able to track the small variation of the inductance. On the other side, the definition of the inductance in Equation (3.12) can not be used because once the current goes towards zero, L_s diverges to infinity.

$$L_s = \frac{\psi_{sd}}{i_{sd}} \tag{3.12}$$

For this reason, the discrete derivative in Equation (3.13) has been chosen to identify the slope of the saturation characteristic.

$$L_s = \frac{\psi_{sd}(k) - \psi_{sd}(k-1)}{i_{sd}(k) - i_{sd}(k-1)} = \frac{\Delta\psi_{sd}}{\Delta i_{sd}} \tag{3.13}$$

3.2.2.4 Short-circuit test

The short-circuit test is proposed by the standard IEEE 1812-2023 [5]. It is not a self-commissioning procedure but it is used to find a benchmark for the SPMSM synchronous inductance L_s.

In the short-circuit test, the SPMSM is driven to a desired speed with the help of a prime mover (in this case, the IM), while short-circuiting its phases. The steady-state Equation (2.15) are modified by imposing $\mathbf{v}_s^{dq0} = 0$, because of the short circuit. The steady-state short circuit equations are given in Equation (3.14).

$$\begin{aligned} 0 &= R_s i_{s,d} - \omega_e L_s i_{s,q} \\ 0 &= R_s i_{s,q} + \omega_e \left(L_s i_{s,d} + \psi_r \right) \end{aligned} \tag{3.14}$$

If the resistance R_s is negligible or if the rotational frequency is high, the short-circuit equations can be simplified as in Equation (3.15).

$$\begin{aligned} 0 &= \omega_e L_s i_{s,q} \\ 0 &= \omega_e \left(L_s i_{s,d} + \psi_r \right) \end{aligned} \tag{3.15}$$

In conclusion, the current is null in the q-axis $i_{s,q} = 0$, and the short-circuit current I_{sc} is just in the d-axis.

$$I_{sc} = \frac{V_{oc}}{\sqrt{3} X_s} \tag{3.16}$$

where the synchronous reactance at rated speed is $X_s = \omega_s L_s$. $V_{oc} = \sqrt{3}\omega_s \psi_r$ is the line-to-line open circuit voltage.

The rotor excitation in a SPMSM is fixed due to the PM. As a consequence, the short circuit current cannot be controlled or varied as in a wound-field synchronous machine. For this reason, the steady-state short circuit current is expected to be higher than the rated current of the SPMSM. This leads to heating of the machine with risk of PM demagnetization and damages of electrical insulation.

A prior analysis is performed to ensure safe operating conditions, avoiding damage to the SPMSM. The short-circuit current is calculated with the Equation (3.16). If the I_{sc} exceeds the maximum allowable value for the SPMSM, the current can be limited by adding an external impedance $\dot{Z}_{ext}$. $\dot{Z}_{ext}$ is reactive to avoid increasing the I_{sc}. The new short circuit current can be estimated by

$$I_{sc} = \frac{V_{oc}}{\sqrt{3} \left(\left| jX_s + \dot{Z}_{ext} \right| \right)} \tag{3.17}$$

Furthermore, the IM should be able to supply the necessary short-circuit torque to the SPMSM. If yes, the short circuit is applied before starting the test. If not, the short circuit is applied after the SPMSM reaches the desired speed through an open-circuit test, which is described in Section 3.2.3.2. However, in this case, the current may significantly exceed the rated value, even up to five times higher than the rated value, which poses a high risk of damage to the SPMSM. [7].

The test configuration in Figure 3.13 shows how the measurements are performed. Three differential current probes measure the line-to-line voltage of the SPMSM and three current sensors are used to measure the phase currents. The short circuit is applied before the test begins. Knowing voltages, currents, and speed, the synchronous inductance is estimated:

$$L_s = \frac{V_{oc}}{\sqrt{3}\omega_e I_{sc}} \tag{3.18}$$

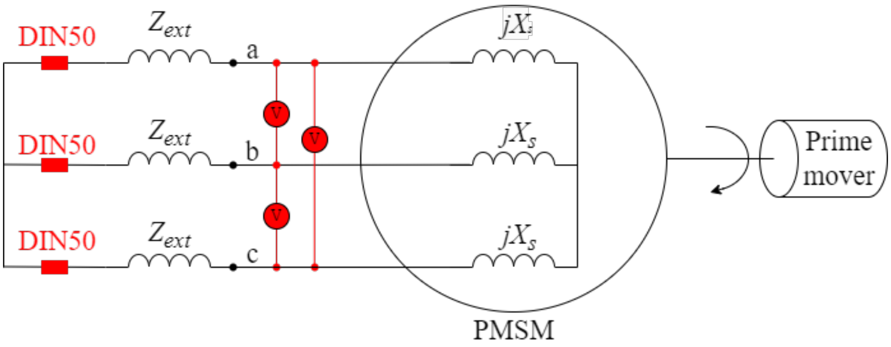

Figure 3.13: Short-circuit test configuration [5].

3.2.3 SPMSM PM-flux

3.2.3.1 I-f startup + sensorless FOC

The PM-flux ψ_R is estimated using the voltage equation in the q-axis in Equation (2.13), where it is related to the electrical rotor speed ω_r. To create a voltage drop in the q-axis due to the presence of the PM, the rotor speed has to be different from zero. For this reason, the constraint of a standstill procedure imposed by the self-commissioning definition cannot be respected. On the other side, the drawback of accelerating the machine at high speed is the temperature increment that can lead to a distortion in the PM-flux estimation since the magnetization of the PM is temperature dependent.

The I-f start-up procedure is then chosen to accelerate the machine. Once a constant speed is reached, a sensorless control is applied and the current is set to zero with a CC. The block diagram for the control method is presented in Figure 3.14. This method was already developed by imperix and it is available on its online knowledge base [41].

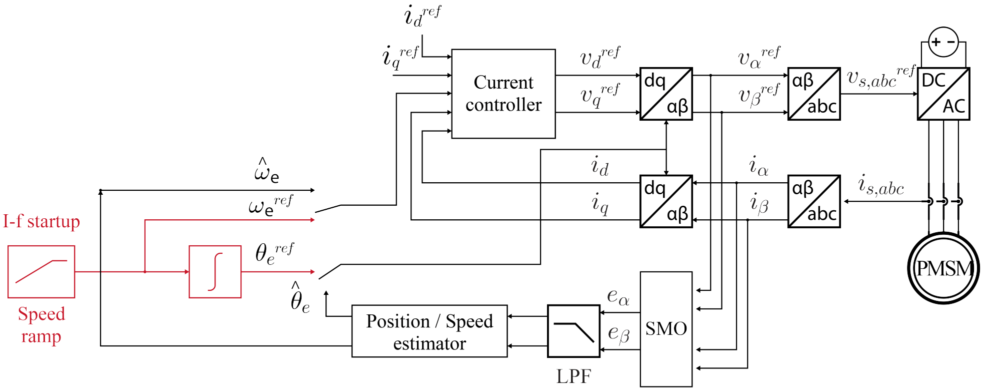

Figure 3.14: Block diagram of an Sliding-Mode Observer (SMO)-based sensorless FOC with I-f startup for a PMSM.

The i-f start-up is an OL procedure based on a virtual reference rotating frame. A speed ramp is set as a reference and integrated to find the position of the virtual reference frame.

$$\begin{aligned} \omega_m^{ref} &= \frac{d\omega_m^{ref}}{dt} \cdot t \\ \theta_e^{ref} &= \int_0^t \omega_e^{ref} dt = n_p \int_0^t \omega_m^{ref} dt \end{aligned} \tag{3.19}$$

The reference current i_{sq}^{ref} in the q-axis is set around the rated value, to provide enough power for the acceleration of the machine. Once the virtual ω_m^{ref} is higher than a minimum speed, the reference speed is kept constant, and i_{sq}^{ref} starts decreasing. The simulated waveforms are shown in Figure 3.16.

How this minimum speed is selected?

The sensorless FOC is based on the knowledge of machine parameters to perform the field alignment. Since the parameters are not accurately known before the commissioning procedure, the inaccurate field alignment can result in poor performance of the speed control. At low speeds, this method is more sensitive to motor parameters. Moreover, at low currents, the measurements are not accurate enough to estimate the back-EMF and extract the position. To reduce the parameter sensitivity, the minimum constant speed is set ”high enough”, as a rule of thumb between 1/3 and 1/2 of the nominal speed.

The second step is to align the virtual reference frame with the real dq0 reference frame. This is achieved by canceling the error between their respective speeds. The error alignment θ_{err} and its variation are defined in

Equation (3.20), respectively.

$$\begin{aligned} \theta_{err} &= \theta_e - \theta_e^{ref} \\ \frac{d\theta_{err}^{ref}}{dt} &= \omega_e - \omega_e^{ref} \end{aligned} \tag{3.20}$$

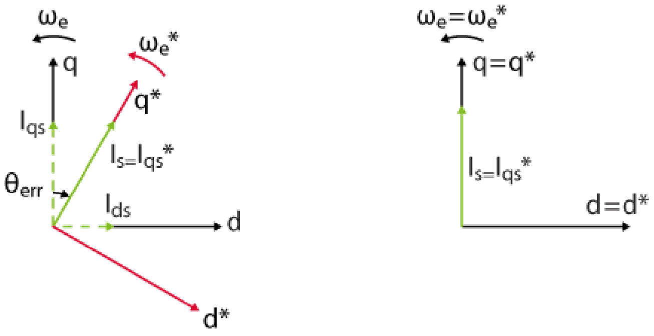

Figure 3.15: (left) rotational frame and current reference from the I-f method (right) rotational frame and current reference from the sensorless FOC.

Once that θ_{err} and i_{sq}^{ref} are within a desired tolerance, the control is switched to a sensorless FOC with the current references set to zero. If no current flow in the dq0 equivalent circuit, there is no voltage drop on the impedance of the machine and Equation (2.13) become:

$$\begin{aligned} v_{s,d} &= 0 \\ v_{s,q} &= \omega_e \psi_r \end{aligned} \tag{3.21}$$

Finally, the PM-flux is calculated from Equation (3.21).

$$\psi_r = \frac{v_{s,q}}{\omega_e} \tag{3.22}$$

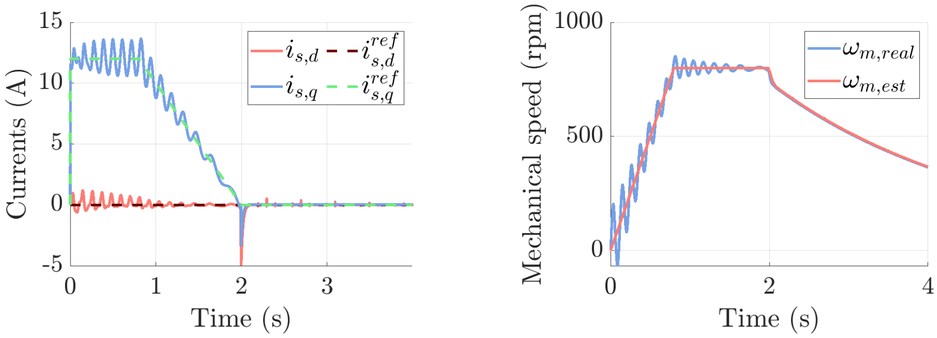

(a) Actual and reference currents.

(b) SPMSM mechanical speed ramp.

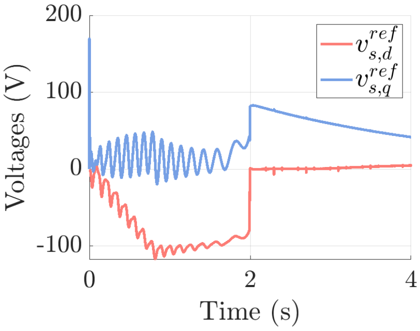

(c) Reference voltages.

Figure 3.16: Simulated I-f startup from $t = 0$s and sensorless FOC at null references in dq0 reference frame introduced at $t = 2$s.

3.2.3.2 Open-circuit test

The second method is to accelerate the SPMSM up to a constant speed thanks to a prime mover (in this work the IM), as in Figure 3.17 (a). The reference speed is arbitrarily chosen following the same considerations as in Section 3.2.3.1. The SPMSM is in an open circuit so the currents $\mathbf{i}_s^{dq0}$ are null and the Equation (3.21) is valid. The voltage measured at the phase of the SPMSM represents the induced voltage due to the PM, which simulated waveforms are in Figure 3.17 (b). Once the machine reaches steady-state conditions, the PM-flux is estimated from Equation (3.21).

$$\psi_r = \frac{v_{sq}}{\omega_e} \tag{3.23}$$

The line-to-line voltage is measured since the neutral of the SPMSM is not user accessible. Three differential voltage probes are placed as shown in the schematic in Figure 3.17. The speed is known by derivating the measured position from the resolver described in Section 5.3. Figure 3.18 represent the simulated mechanical IM speed and the SPMSM voltages.

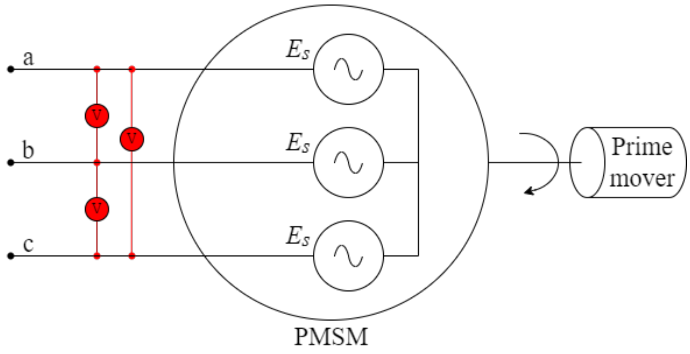

Figure 3.17: Open circuit electrical configuration.

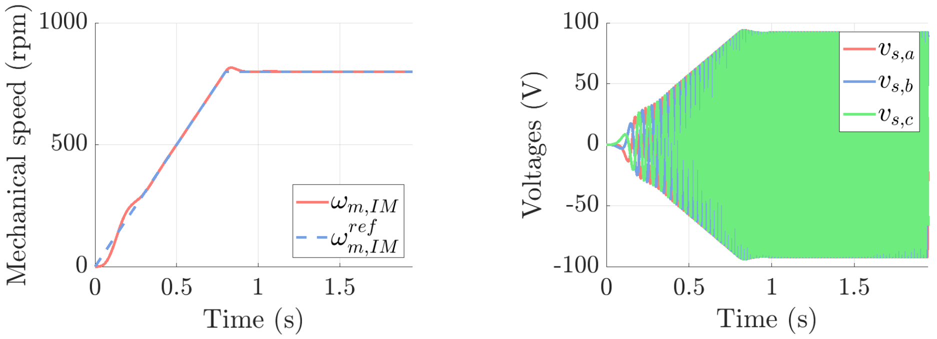

(a) IM mechanical speed.

(b) SPMSM back-EMF measurements.

Figure 3.18: Simulation of the open-circuit test.

3.3 Parameter Estimation for IM

In all the IM self-commissioning procedures the single-phase configuration, represented in Figure 3.6 and described in Section 3.2.1.3, is used.

3.3.1 IM stator resistance

The stator resistance is estimated with the same method used for the SPMSM through the DC injection in section Section 3.2.1. The theory is the same, the only difference is the equivalent circuit in which the voltage signals are injected. Because the electrical frequency ω_e is null due to DC injection, the inductances are short-circuited. Specifically, the magnetizing inductance is short-circuited, so no current flow in the rotor branch. The only element in the equivalent circuit that causes a voltage drop is the stator resistance R_s.

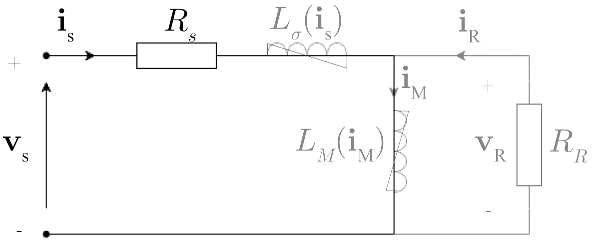

Figure 3.19: Electrical vector configuration in the abc three-phase reference frame in case of DC injection at stand-still ($\omega_r = 0$).

3.3.2 IM leakage inductance

3.3.2.1 DC+AC method for IM

Figure 2.7 is the dynamic IM inverse-Γ equivalent circuit in case of linear conditions. If the stator teeth and yoke of the machine saturate, the current becomes a nonlinear function of the stator flux. If the iron saturation is considered and at a standstill, Equation (2.40) in the three-phase reference frame becomes:

$$\begin{cases} \mathbf{v}_s = R_s\mathbf{i}_s + L_\sigma\left(\mathbf{i}_s\right)\dfrac{d\mathbf{i}_s}{dt} + L_M\left(\mathbf{i}_M\right)\dfrac{d\mathbf{i}_M}{dt} \\ 0 = R_R\mathbf{i}_R + L_M\left(\mathbf{i}_M\right)\dfrac{d\mathbf{i}_M}{dt} \end{cases} \tag{3.24}$$

The saturation can be modeled by splitting its effect into two inductors: the leakage inductance $L_\sigma(i_s)$ and the magnetizing inductance $L_M(i_M)$. At standstill, the rotor angular speed ω_r is zero, by adding saturation, the circuit in Figure 2.7 becomes as in Figure 3.20.

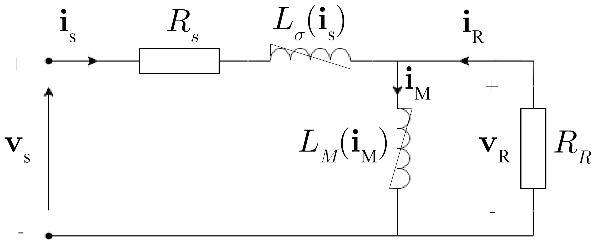

Figure 3.20: Inverse-Γ vector equivalent circuit including stator iron saturation in abc reference frame, at standstill ($\omega_r = 0$).

At steady state, the Thévenin equivalent impedance of the circuit in Figure 3.20 is:

$$Z(j\omega_h) = R_s + j\omega_h L_\sigma + \frac{j\omega_h L_M R_R}{j\omega_h L_M + R_R} \tag{3.25}$$

where $\omega_h = 2\pi f_h$, with f_h frequency of the injected signal. The last term of Equation (3.25) converges to R_R for sufficiently high values of frequency [42]. Subsequently, the approximation of the Thévenin equivalent impedance in Equation (3.25) is given in Equation (3.26).

$$Z(j\omega_h) \approx R_s + R_R + j\omega_h L_\sigma \tag{3.26}$$

As for the SPMSM, the DC+AC method explained in Section 3.2.2.2 is employed to estimate the instantaneous inductance. All the considerations already done in Section 3.2.2.2 are valid. The difference is the reference frame in which the procedure is performed. The single-phase configuration in Figure 3.6 is considered. Since it is an OL method, the injected signal in Equation (3.27) is the sum of a small sinusoidal voltage with a predefined set of increasing DC voltage levels while measuring the phase currents at each stage.

$$v_{sa}(t) = v_{sa,dc} + v_{sa,ac}(t) = v_{sa,dc} + V_{sa,ac}\cos(\omega_h t) \tag{3.27}$$

Applying the DFT on the reference phase voltage v_{sa} and phase current i_{sa}, measured from the current sensor in the PEB 8038, the fundamental component is extracted. Knowing the Thévenin impedance with Equation (3.28), the instantaneous leakage inductance is calculated using Equation (3.29).

$$v_{sa}^{fund} = \dot{Z}(j\omega_h)\, i_{sa}^{fund} \Rightarrow \dot{Z}(j\omega_h) = \frac{v_{sa}^{fund}}{i_{sa}^{fund}} \tag{3.28}$$

$$X_\sigma = |\dot{Z}\left(j\omega_h\right)| \sin\theta_h \Rightarrow L_\sigma = \frac{X_\sigma}{2\pi f_h} \tag{3.29}$$

The leakage inductance is calculated per each set point defined bu the direct current so that the characteristic curve $L_\sigma\left(i_{sa}\right)$. Notice that the injected voltage in the system is corrected by applying the compensation to the reference voltage with the apposite lookup table to overcome inverter non-linearity.

As for the SPMSM in Section 3.2.2.1, the high-frequency test is not indicated for the resistance estimation. The rotor resistance R_R can be extracted from the real part of the Thévenin impedance $\dot{Z}\left(j\omega_h\right)$, by subtracting the stator resistance R_s. However, the high frequency can result in increasing resistance due to the skin effect and proximity effect.

3.3.2.2 Locked rotor test

The locked rotor test is performed by following the standard IEEE 112-2017 [3]. It is used to estimate the leakage impedance and the rotor resistance of the IM. This test is not a self-commissioning procedure, but it represents a benchmark for the self-commissioning method explained in Section 3.3.2.1.

The rotor of the IM is locked by a mechanical mean. It contrasts with self-commissioning techniques that ensure the standstill condition through control. The phase voltage at the rated frequency is increased until the phase currents reach the rated load value. This allows to have the same saturation condition as normal operation. In locked rotor condition the phase voltage is below its rated value. Special care should be taken when increasing the voltage as there is a risk of damaging the machine due to the low value of the machine impedance resulting in high currents and so overheating. Once the steady-state condition is reached, the measurements of the phase voltages are taken with three differential voltage probes. The current is measured with a current probe directly at the IM phases.In the post process, the DFT is applied to the current and voltage waveform, finding the real and imaginary part of the impedance.

$$v_s^{fund} = Z\left(j\omega_e\right) i_s^{fund} \Rightarrow Z\left(j\omega_e\right) = \frac{v_s^{fund}}{i_s^{fund}} \tag{3.30}$$

$$Z\left(j\omega_e\right) \approx R_s + R_R + j\omega_e L_\sigma \tag{3.31}$$

The magnetizing inductance L_M is neglected because It is much higher than leakage phase inductance L_σ. As a consequence, it can be assumed that there is no current floating to L_M parallel branch. The vector electrical configuration of the locked rotor test is given in Figure 3.21.

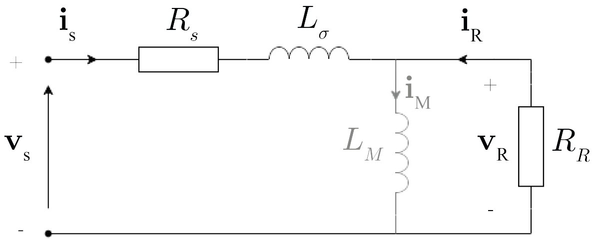

Figure 3.21: Vector electrical equivalent circuit for locked rotor test in the three-phase reference frame.

The reactive impedance is directly related to the leakage inductance L_σ, as shown in Equation (3.31). Instead, the resistive impedance represents the rotor and stator resistance $R_R + R_s$.

$$\begin{aligned} R_s + R_R = |Z(j\omega_e)|\cos\theta_e \Rightarrow R_R = |Z(j\omega_e)|\cos\theta_e - R_s \\ X_\sigma = |Z(j\omega_e)|\sin\theta_e \Rightarrow L_\sigma = \frac{X_\sigma}{2\pi f_e} \end{aligned} \tag{3.32}$$

The stator resistance is already known from the DC test described in Section 3.2.1.

3.3.3 IM rotor resistance

In this section, the method by L. Peretti in [8] for the rotor resistance estimation is studied. The rotor resistance is calculated by knowing the voltage drop over it and the corresponding rotor current. First, the current is found. A single-phase OL voltage at low frequency f_l is injected into the IM circuit. The configuration is the same already used for the multiple DC injection shown in Figure 3.6. Since it is a single-phase injection, just phase a is considered, with its corresponding equivalent circuit. A single-phase injection does not create a rotating magnetic field, so the machine is not rotating, the rotor angular speed (ω_r) is null and the slip is one.

The injected voltage is

$$v_{sa} = V_{sa,dc} + V_{sa,ac}\cos(\omega_l t) \tag{3.33}$$

Under normal working conditions, the frequency of the injected signal is below its rated slip value. Furthermore, at low frequencies, the skin effect of rotor bars is limited.For these reasons, The frequency is arbitrarily chosen to be 5% of the nominal slip $f_{slip} = f_e - f_r$.

$$f_l = 0.05 f_{slip} \tag{3.34}$$

Looking at the inverse-Γ equivalent circuit at a standstill in Figure 3.22, the rotor side is composed of just the rotor resistance R_R, since the rotor leakage inductance L_{lr} is shifted on the stator side.

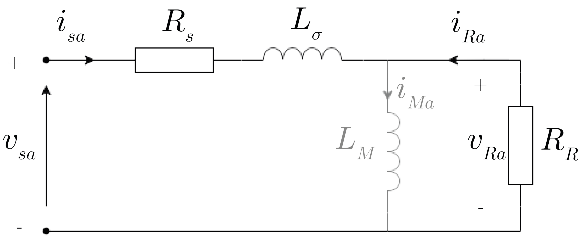

Figure 3.22: Single phase electrical equivalent circuit in phase a for locked rotor test.

As a consequence, the rotor current $\mathbf{i}_R$ is a resistive current in phase with the voltage in phase a. The magnetizing inductance is neglected for the same reason as in Section 3.3.2.2. So, the α (or a) component of the rotor current corresponds to the α (or a) component of the stator current. Moreover, the a-axis overlaps with the α-axis, as shown in the transformation.

$$\mathbf{i}_R = i_{Ra} = i_{sa} = i_{s\alpha} \tag{3.35}$$

The voltage on the stator is assigned. To find the voltage on the rotor resistance, the inverse formula from Equation (3.24). In the case of a sinusoidal constant frequency injection, the Equation (3.24) is written in phasor form.

$$\begin{aligned} \dot{V}_{Ra} = (V_{R\alpha} + jV_{R\beta}) = \dot{V}_{sa} - (R_s + j\omega_l L_\sigma)\, \dot{I}_{sa} = \\ = V_{s\alpha} - (R_s + j\omega_l L_\sigma)\,(I_{s\alpha} + jI_{s\beta}) \end{aligned} \tag{3.36}$$

where the stator resistance and the leakage inductance were previously estimated.

Knowing the voltage on the rotor resistance and the rotor current, the rotor resistance of the inverse-Γ equivalent circuit is:

$$R_R = \frac{\left|\dot{V}_{Ra}\right|}{\left|\dot{I}_{Ra}\right|} \tag{3.37}$$

$$\cos\left(\theta_R\right) = \frac{V_{R\alpha}I_{s\alpha} + V_{R\beta}I_{s\beta}}{\left|\dot{V}_{Ra}\right|\left|\dot{I}_{sa}\right|} \tag{3.38}$$

$$R_R = \frac{V_{R\alpha}^2 + V_{R\beta}^2}{V_{R\alpha}I_{s\alpha} + V_{R\beta}I_{s\beta}} \tag{3.39}$$

The rotor resistance, as the stator resistance, is very sensitive to temperature variation. For this reason, an online estimate is suggested also in this case.

From the standard IEEE 112-2017 in [3], the rotor resistance is found by performing the locked rotor test described in Section 3.3.2.2, whose result represents a benchmark for R_R.

Chapter 4

Software tools

4.1 Simulation and ACG

The first step to applying the methods chosen from the state-of-the-art self-commissioning in Section 3.1 is by creating simulation models for each of the electrical machines in analysis. These are later validated through the experimental setup, described in Chapter 5.

The primary software used is Matlab Simulink, which is directly linked with the Imperix Software Development Kit (SDK). With the help of the SDK, a unified development environment is created that can be used to simulate the control and generate code for experiments through the Automated Code Generation (ACG). This highlights the ability to easily switch between simulations and experiments. Each simulation file comprises a Controller block and a Plant model block. A typical scheme of the simulation model is presented in Figure 4.1.

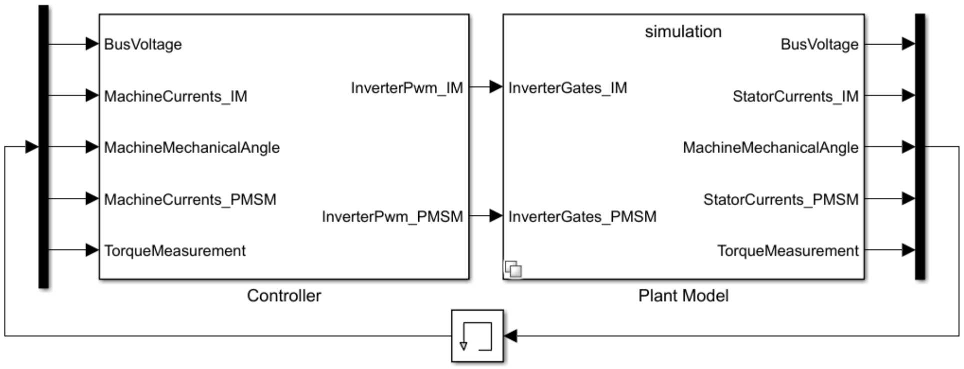

Figure 4.1: Simulink model of dual Imperix motor testbench.

Two modes are available for each Imperix file (Figure 4.2): Simulation mode and ACG mode. In Simulation mode, the model is simulated using the plant model drawn inside the Plant model block. In ACG mode, Simulink keeps the same control and ignores the plant model. C++ code is automatically generated by the Simulink Coder engine when the model is built.

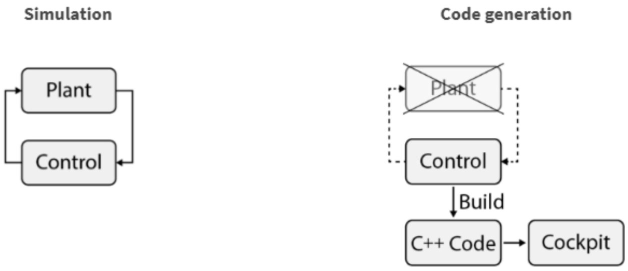

Figure 4.2: Simulation mode and code generation mode.

The control inputs are on the left. They come from the output of the plant model in Simulation mode, or the sensors in ACG mode. Once the signals, such as measured current and measured DC voltage, are taken from the real system, they are translated from analog to digital thanks to the appropriate Imperix block, like the Analog to Digital Converter (ADC) block. Each analog measured quantity is interfaced in the controller subsystem with the appropriate Imperix block, for instance, the torque with the torque sensor block, the mechanical angular position with the resolver block, and the machine temperature with the temperature sensor block.

The subsystem on the left models the digital Controller block, inside which different control strategies, such as RFOC, are built, through blocks from Simulink libraries. In ACG mode, once the C++ code is generated and compiled, the Cockpit software opens automatically and the code is executed on the Imperix target (B-Box Rapid Control Prototyping (RCP)). The controller is sampled at a rate equal to the interrupt frequency that is 20 kHz, and with a phase corresponding to the sampling phase.

The controller outputs on the right represent the Carrier-based PWM (CB PWM) signals generated through the Imperix CB PWM block, thanks to which the voltage waveforms (inputs of the electric drive) are created. Specifically, the controller outputs in Figure 4.1 are two because the plant models the dual Imperix motor testbench, so both IM and SPMSM are controlled.

The plant in Simulation mode is shown in Figure 4.3. It is built thanks to the Simscape Electrical library and it represents the system in a time-continuous domain. From the right to the left, its components are the DC-link, the three-phase inverter, the current and voltage sensors, the electrical machine under study, its position sensor (resolver), and its torque sensor.

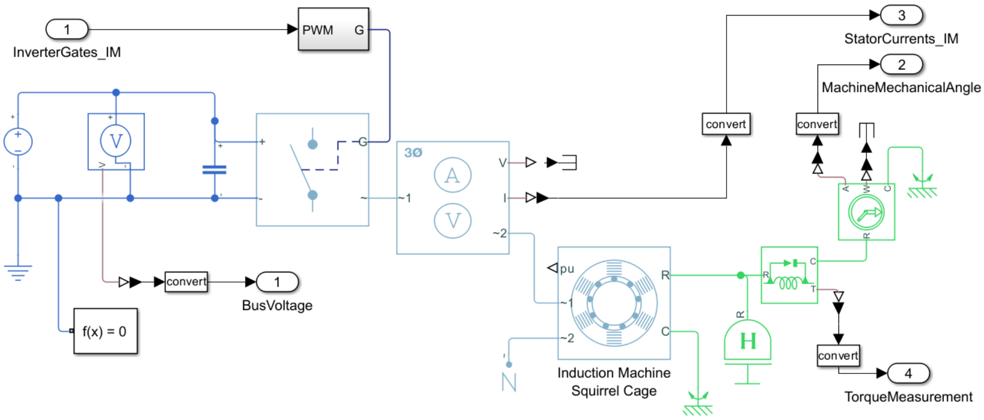

Figure 4.3: Plant model of an electric machine.

Additionally, Imperix provides a built-in software tool for real-time access, monitoring, and tuning of the controllers' variables, named Cockpit, that allows also a graphical visualization of the model variables from the host PC, as in Figure 4.4. The acquired signals are visualized on Cockpit from a rolling plot (sampling at 20 Hz) or a scope module (sampling at 20 kHz) and can be exported through a CSV file or a MATLAB figure.

TN139_MOTOR_TB_RFC

10.10.13.33 BLOCKED

PWM DISABLED CPU 12.6%

USER VARIABLES

Name	Data
desired_speed	800
Speed_Ki	30
Speed_Kp	1,2
block_rotor	0
im_rpm	0
angle_offset	0,40813
i0_pmsm	-0,1613
speed_rate	1000
id_pmsm	0,01950
iq_pmsm	0,01873
Is_a_im	-0,0457
im_rpm_ref	0
Is_a_pmsm	-0,1895
Is_b_im	-0,0259

SCOPE

TRIGGER

Window [ms] 200
Edge Rising
Signal Is_a_pmsm [Pl
Mode Auto
Level 0,0000000000
Position [ms] 100,000000000

TRANSIENT EVENTS

Variable -- none --
Position [ms] [100, 200, 300]
Step (±) [1.0, -4.0, 3.0]

CURSORS

Enable cursors
Cursor 1 [ms] 40,000000
Cursor 2 [ms] 160,000000
ΔT –
1/ΔT –

X AXIS

PLOT -1 Y AXIS

PLOT 0 Y AXIS

PLOT 1 Y AXIS

Severity: Info ☑ Warning ☑ Error ☑ Source: BBOS ☑ User ☑

Sev	Date	Source	Message
i	04.01.2024 14:29:44:778	BBOS	Configuration completed successfully.
i	04.01.2024 14:29:44:778	BBOS	Ready to operate.

Figure 4.4: Overview of Cockpit's interface.

Figure 4.5 clarify the Imperix ACG SDK. More information regarding the implementation details of ACG SDK and Cockpit can be found on the website in [43].

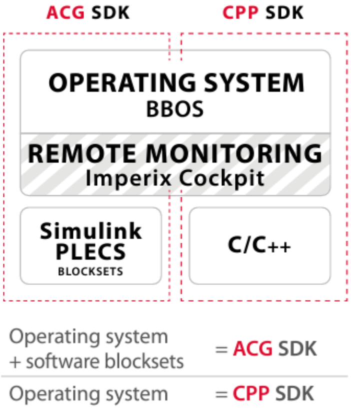

Figure 4.5: Imperix ACG SDK.

4.2 Full self-commissioning routine

Imperix provided files in which some control strategies, used in this work, are developed, for instance, RFOC for IM, FOC for SPMSM, PR controller for AC injection and I-f start-up (employed for PM-flux estimation). Figure 4.6 represent the flowchart of the entire self-commissioning routine for the SPMSM (a) and the IM (b). The procedure is composed of a set of sequential steps, since the estimation of a parameter depends on the knowledge of another one, for instance, to estimate the magnetizing inductance L_M the leakage inductance L_σ has to be known. Once the parameters are found, the control gains of the CC for the FOC are tuned. The only information that has to be entered into the algorithm by the user is the rated values from the nameplate data.

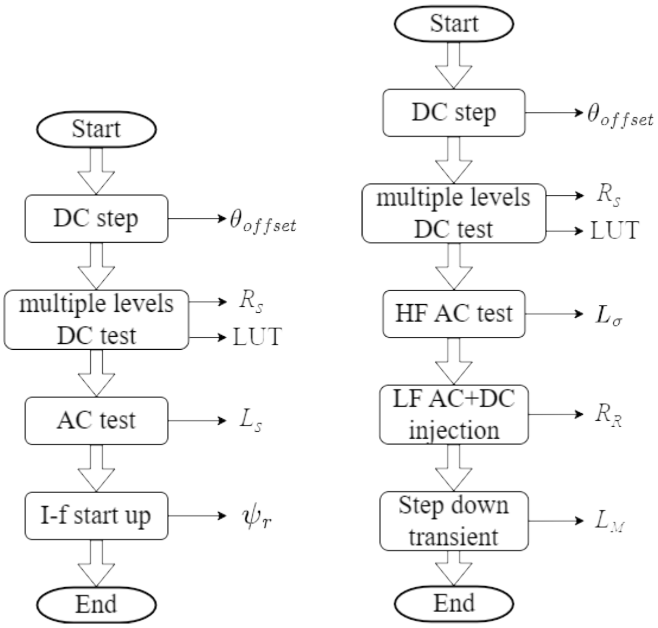

(a) SPMSM. (b) IM.

Figure 4.6: Algorithm flowchart of self-commissioning routine.

Chapter 5

Experimental design

The motor drive bundle, presented in the knowledge base section [44] of the Imperix website, is employed to experimentally verify the state-of-the-art self-commissioning. The motor drive bundle in Figure 5.1 is composed, from top to bottom, of the control stage and the power stage. The control stage in Figure 5.4 is represented by a B-Box RCP (a) and its motor interface (b). The power stage in Figure 5.6 is composed of two inverters, in this project 4U Closed Rack – Type C (a), and a reversible DC supply (b).

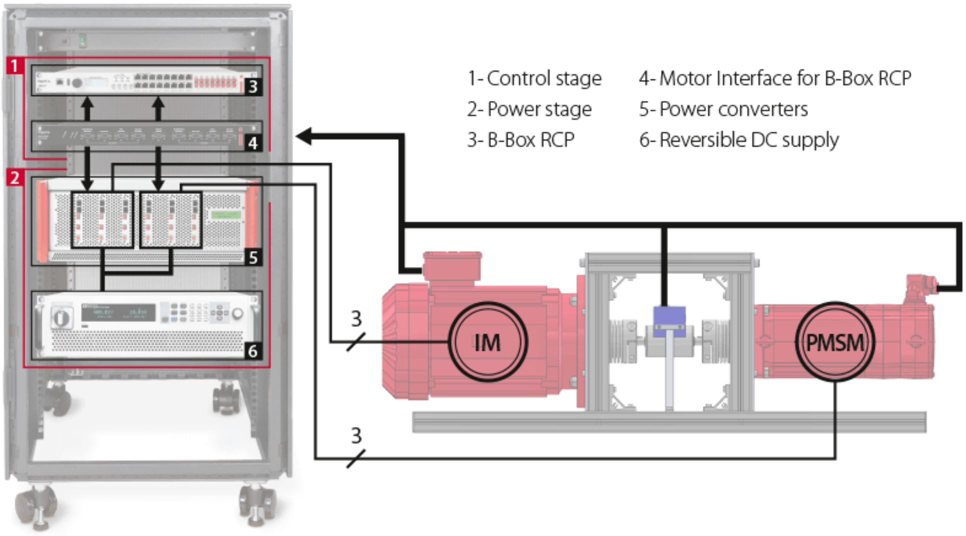

Figure 5.1: Default configuration of the motor drive bundle.

5.1 Control stage

The first element of the control stage is the B-Box RCP. The B-Box RCP is a fully programmable modular digital controller. In this work, it is programmed by drawing a block diagram in Simulink (ACG SDK), but it is possible to program directly in C/C++ thanks to the CPP SDK. The converter is connected to the host PC through a Gigabit Ethernet connection, thanks to which the user code built in Cockpit is loaded. B-Box RCP has high processing power thanks to a 1 GHz dual-core ARM processor Xilinx Zynq 7030 SoC (CPU) mated with a Kintex-based programmable logic (FPGA).The control task (user code) runs on the CPU, whereas the low-level and time-critical tasks (such as PWM modulators or safety logic) run in the FPGA. CPUs and FPGA are placed in the B-Board, inside the B-Box. Figure 5.2 clarify how B-Box RCP interact with the host PC.

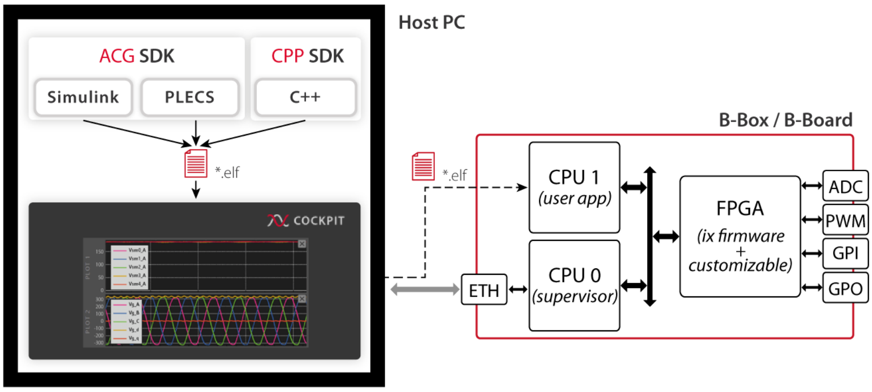

Figure 5.2: Interaction between B-Box RCP and host PC.

A dedicated hardware protection circuit in the B-Box RCP blocks all its PWM outputs in case of dangerous or faulty operating conditions. The faults can come from the hardware, for instance in case the configured threshold is reached, or the software, like excessive interrupt frequency considering the code complexity. Threshold conditions are set through a fully programmable analog front end with 16 input channels ADC on the front panel (for RJ45 optical connection with the power rack) and 16 General Purpose Inputs (GPI) on the back panel (for the VHDC connection with the motor interface). The outputs of the B-Box are analog, digital General Purpose Outputs (GPO), and optical PWM to allow communication with the power rack, as in Figure 5.3. The B-Box controller generates the control signals for the converter (PWM gate signals), based on the feedback of motor currents and DC bus voltage, measured with the embedded sensors on the PEB 8038. The gate signals are transmitted to the PEB 8038 modules through optical fibers, where the switches apply the signal by adjusting the duty cycle of the machine phase current waveform. The motor currents and the DC bus voltage are then fed back to the controller through RJ45 optical cables. To complete the loop the signal employs a delay time (T_d) equal to one switching period (T_s) and a half ($T_d = 1.5T_s$) due to PWM time delay. This delay is translated in an undesired rotation of the dq0 reference frame by the angle $-\omega_s T_d$. The transformation angle θ_s is than corrected by adding the compensation term $\omega_s T_d$ as $\theta'_s = \theta_s + \omega_s T_d$. Figure 5.3 indicates the assignation of the analog and PWM channels.

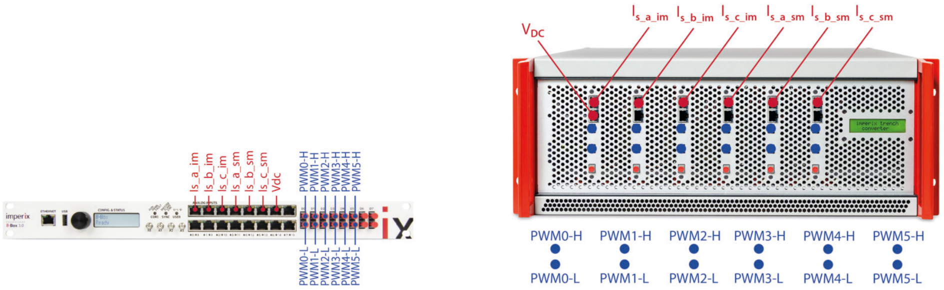

(a) Channel assignation on the B-Box RCP.

(b) Channel assignation on the converter rack.

Figure 5.3: Connection of the B-Box with the power rack.

The second element of the control stage is the Motor Interface. The Motor Interface is an extension of the B-Box RCP and supports a wide variety of sensors relevant to motor control applications. It is designed for use with a dual motor setup such as the Imperix Motor Testbench. The position and speed of each motor can be measured either by an incremental encoder, a resolver, hall sensors, or a sin/cos encoder. The Motor Interface also supports temperature measurements, as well as an optional torque sensor. Finally, a 24Vdc brake command and an interlock are available for safety purposes.

(a) Imperix B-Box RCP.

(b) Imperix motor interface for the B-Box RCP.

Figure 5.4: Control stage. [44]

The B-Box RCP communicates with the Motor Interface through a single VHDCI cable placed on the back panel, as in Figure 5.5 (b). The front panel of the motor interface in Figure 5.5 (a) is connected to the Imperix motor testbench. The Motor Interface includes a brake control unit, which can be linked to an emergency stop button, improving the safety features of the B-Box.

(a) Connection of the motor measurements to the Motor Interface, front view.

(b) Connection the motor interface to the B-Box RCP, back view.

Figure 5.5: Connections of the motor interface.

5.2 Power stage

The power stage in Figure 5.6 is composed of the power converters, in this project 4U Closed Rack – Type C (a), and the reversible DC supply (b).


(a) Imperix power converter 4U Closed Rack – Type C.

(b) Reversible DC source.

Figure 5.6: Power stage. [44]

The type C enclosure is composed of six PEB power modules and provides IP20 protection from the surroundings. The system also provides power supply to the modules as well as variable-speed air cooling. Finally, the enclosure is equipped with an LCD screen allowing to monitor the status of the modules.

The half-bridge Power Module 8038 is shown in detail in Figure 5.7. Specifically it is composed of:

1. on-board voltage and current sensors outputs, from which the analog signal of machine phase current and of DC bus voltage is sent to the digital controller. Moreover, over-current/voltage/temperature protections are embedded in the power module to prevent possible damage.

2. gate drivers inputs, from which the optical signal coming from the digital controller is received.

3. fault output, connected to an optical fiber emitter for fault feedback signal.

4. board-to-board link.

5. power supply (5/12 V), for local control and cooling fan.

6. speed-regulated cooling fan (120 W).

7. DC link terminals, for the DC bus connection.

8. power switches, two Silicon Carbide (SiC) MOSFETs with a drain-source on-state resistance $R_{DS(on)}$ of 20 mΩ.

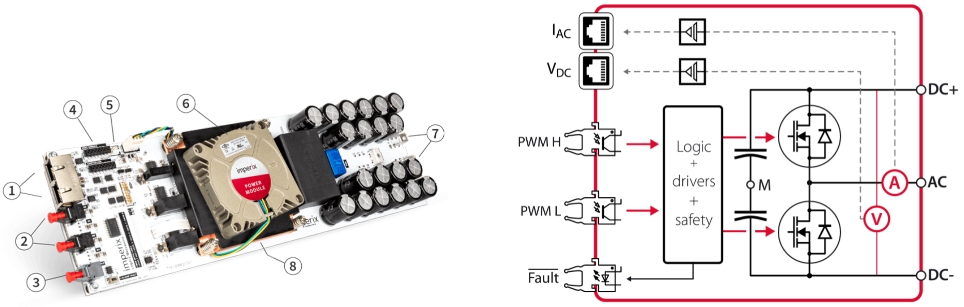

(a) Overview. (b) Schematic.

Figure 5.7: Half bridge power module PEB8038. [44]

The power converter is connected to the DC bus from the back panel. The DC bus in Figure 5.6 (b) is already connected to the DC source out of the box in Figure 5.8. The electrical machine phases are connected to the back panel of the power rack, and the built-in brake of the PMSM is connected to the brake control unit of the motor interface.

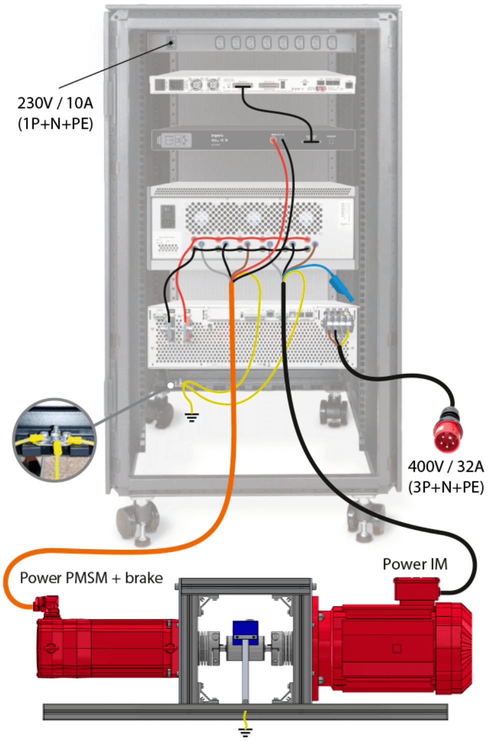

Figure 5.8: Wiring of the power stage and earthing connection.

The electrical equivalent circuit in Figure 5.9 shows the entire system composed of the motor testbench, two inverters, and a DC bus. One machine is the Device Under Test (DUT), working as a motor (M) or as a generator (G), while the other one acts as a controllable load.

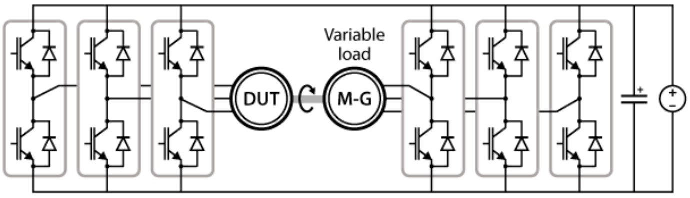

Figure 5.9: Dual-motor configuration with a shared DC bus.

5.3 Dual Motor testbench

The Motor Testbench shown in Figure 5.10 is composed of:

1. IM terminal box, in which the stator winding ends are connected to a terminal block for the IM power supply.
2. Squirrel cage DRN112M4 IM from SEW Eurodrive [45], consisting of a laminated rotor core attached to a steel shaft. The stator winding, encapsulated with synthetic resin, is inserted into the half-closed slot on the laminated stator core. This laminated core and the motor housing form the stator. The stator is star-connected at the factory. However, since the windings (and the neutral) are user-accessible, it is possible to wire them in a double-star or delta configuration. The temperature feedback is provided by a 4-wire PT1000 sensor installed on one of its windings. The main specifications are given in Table 5.1.
3. Flexible couplings. Both machines are coupled to the torque sensor using KB4HC/80-89-N14-N28 bellows couplings from KBK Antriebstechnik GmbH. They provide a high torsional stiffness while allowing shaft misalignments. The use of flexible couplings allows a small misalignment of the shafts. As a result, the torque sensor has some backlash by design and can vibrate a little bit. This translates into an oscillation in the measurement at the mechanical frequency of the rotor.
4. Bidirectional torque sensor series 2200 from NCTE 2.

5. Mechanical brake, installed on the PMSM. It is activated by default to hold the rotor in place, but it is also suitable for repetitive emergency braking. The brake is released by energizing its coils with a 24 V signal.

6. CM3C80L PMSM from SEW Eurodrive [46] with a star connection. The three-phase stator winding is user accessible but, unlike the IM, not the neutral cable. The rotor is characterized by surface mounted PM. Like the IM, it features a 2-wire PT1000 sensor for temperature feedback directly installed on the motor winding. The main specifications are given in Table 5.3.

7. Power and signals plugs for PMSM.

8. Resolver, installed on the PMSM for the measurements of absolute mechanical rotor angular position. Since PMSM and IM are coupled on the same shaft, the resolver provides the position of both machines. Following IEC 60034-8 [47], the position angle increases when the shaft rotates in the clockwise direction of the PMSM. The resolver has to be aligned with the pole of the machine. For this reason, the resolver offset is found with the apposite calibration procedure before starting the self-commissioning routine. A direct current is injected into phase a of the PMSM to force the alignment of the rotor and stator fluxes. Once the rotor reaches a steady state, the measured mechanical angle representing the resolver offset is registered. This procedure is performed only once since the absolute zero of the resolver is fixed, consequently the offset angle is constant.

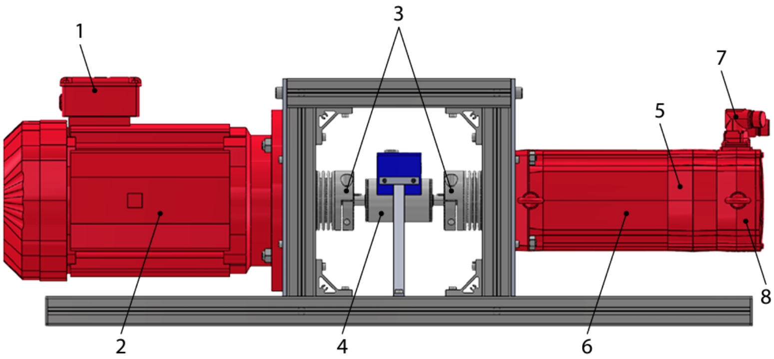

Figure 5.10: Overview of the dual motor testbench.

Table 5.1: Main specifications of the IM.

Characteristic	Symbol	@50 Hz	Unit
Pole pairs	n_p	2	-
Rated line voltage	$V_{\mathrm{LL,\,N}}$	380	V
Rated power	P_N	4	kW
Rated torque	τ_N	26	Nm
Rated speed	n_N	1464	rpm
Rated current	I_N	8.4	A
Power factor	$\cos\varphi$	0.81	-
Starting torque ratio	τ_A/τ_N	2.4	-
Starting current ratio	I_A/I_N	8.2	-
Moment of inertia	J	178	kg cm^2

Table 5.2: Parameters of the IM steady-state T-equivalent circuit.

Characteristic	Symbol	Value	Unit
Stator resistance	R_s	1.24	Ω
Stator leakage inductance	L_{ls}	11.5	mH
Mutual inductance	L_m	183	mH
Rotor resistance	R_r	0.73	Ω
Rotor leakage inductance	L_{lr}	11.5	mH

Table 5.3: Main specifications of the SPMSM.

Characteristic	Symbol	@50 Hz	Unit
Pole pairs	n_p	4	-
Rated line voltage	$V_{\mathrm{LL,\,N}}$	400	V
Rated power	P_N	4.8	kW
Rated torque	τ_N	22.8	Nm
Rated speed	n_N	2000	rpm
Rated current	I_N	11.2	A
Maximum torque	τ_m^{max}	68.4	Nm
Maximum speed	n_m^{max}	2750	rpm
Maximum current	I_N^{max}	34.9	A
Moment of inertia	J	40.6	kg cm^2

Table 5.4: Parameters of the SPMSM steady-state equivalent circuit.

Characteristic	Symbol	Value	Unit
Stator resistance	R_s	0.559	Ω
Synchronous inductance	L_s	4.24	mH
PM-flux	ψ_r	0.2748	Wb

5.4 Assessing validity of the data collected

The validity of the collected data is analysed looking at the accuracy of the measurements. The current sensor inside the power module PEB8038 has a sensitivity of 50.0 mV/A. Instead, the sensitivity of the DC voltage sensor in the PEB8038 is 4.99mV/V. The noise is translated from the measurement to the estimated parameters. In this work, the noise is rejected by taking the average value of the data of interest inside a window of observation.

To double-check the correctness of the experimental data, external measurement devices are used. Subsequently, the accuracy of these external measurement instruments is described.

The resistance and inductance of the motor are measured with an LCR meter, Matrix MCR-5200 Measurements can be done with 8 different test signal levels at a measurement accuracy of 0.1% as shown in the datasheet [48].

In the case of DC injection, the value of interest is only the resistance. For this reason, the multimeter Brymen BM785 is used, with an accuracy of 0.03%, showing two digits after the decimal point. More information can be found in the datasheet in [49].

A digital oscilloscope (RIGOL MSO5074 [50]) is used for the visualization of voltage and current waveform. They are directly measured from the phase of the electrical machine thanks to differential voltage probes and current probes, respectively. The window of observation of the scope needs to be carefully chosen to ensure the validity of the measurements.

The voltages and the currents are visualized in the scope thanks to differential voltage probes (Micsig DP10013 [51]) thanks to the current probes (Micsig CP2100B [52] and Tektronix A6304XL [53]), respectively.

Chapter 6

Results and Analysis

In this chapter, the results from the method described in Chapter 3 are presented and discussed. They are performed using the experimental setup in Chapter 5, mated with the software environment in Chapter 4. The differences between the ideal case and the real case are highlighted.

During all the experimental tests, these values are set:

- the DC bus voltage is 300V.
- the value of deadtime of the MOSFET shown in Section 5.2 is $t_{\triangle} = 500$ ns.
- the switching frequency is 20 kHz.

6.1 Results for SPMSM

6.1.1 SPMSM stator resistance

6.1.1.1 One-level DC injection

The signal employed for the one-level DC injection method is depicted in Figure 6.1. No dead-time compensation is applied in this experiment. This setup can be compared with the corresponding simulation presented in Figure 3.2, which lacks any dead time. This comparison aims to demonstrate the extent to which the d-axis component of the reference voltage in Figure 6.1 (b) increases compared to the ideal scenario in Figure 3.2 (b) (indicated by the red curves).

In both instances, the actual currents accurately follow their respective references. However, in the ideal scenario depicted in Figure 3.2 (b), the voltage is lower than in the experimental test shown in Figure 6.1 (b) (as indicated by the red curves, approximately half). This discrepancy arises because, in the ideal case, only the machine resistance contributes to the voltage drop. Conversely, in the experimental scenario, the total resistance is higher due to external factors such as the setup outside the machine and the non-linearity of the inverter. This observation confirms the theory presented in Section 3.2.1.

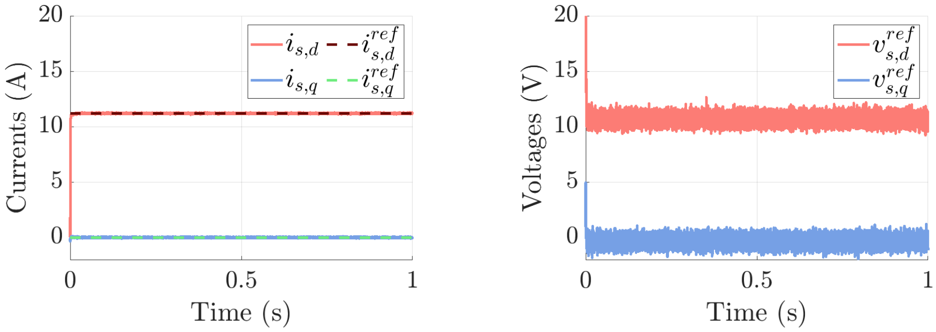

(a) Reference currents.

(b) Output voltages.

Figure 6.1: One level DC injection with CC, step at 0 s from zero Ampere to the rated value I_{sn} without dead time compensation.

Following this, compensation for the inverter non-linearity is introduced by incorporating the LUT depicted in Figure 6.6 into the system. The effect of this compensation is demonstrated in Figure 6.2. The corresponding simulated scenario is shown in Figure 3.3.

Initially, the voltages with and without compensation for inverter non-linearity are compared (represented by the red and blue curves in Figure 6.2 respectively). When the LUT is integrated into the system, the voltage (v_{sd}^{ref} (LUT)) is lower compared to the case where no LUT is employed (v_{sd}^{ref} (No LUT)). With the inclusion of the LUT, the reference voltage more closely aligns with the actual phase voltage as it compensates for the non-linear drop ($v_{sd} \approx v_{sd}^{ref}$). This allows to use of the reference voltage for the estimation of the stator resistance from Equation (3.1).

Subsequently, the comparison between the simulated waveform (Figure 3.2) and the experimental waveform with compensated inverter non-linearity (Figure 6.2) is examined. Despite compensating for the inverter's non-linearity, the experimental voltage slightly exceeds the ideal case. This discrepancy arises because the resistance of the system in the experimental setup is higher than the simulated resistance, which only considers the machine resistance.

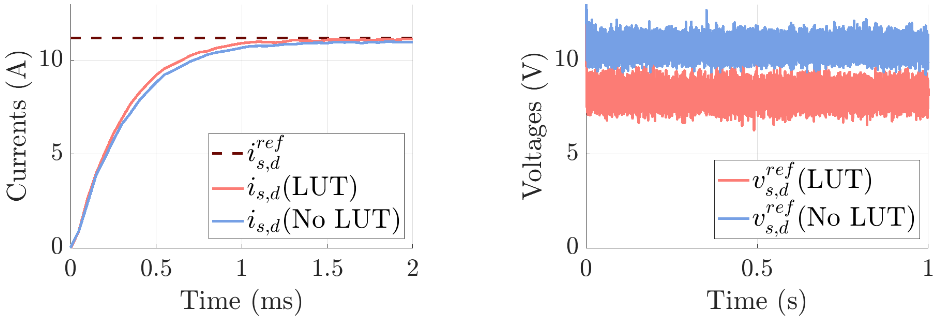

(a) Reference currents.

(b) Output voltages.

Figure 6.2: Effect of the LUT on control performances in the d-axis.

6.1.1.2 Two-level DC injection

The theory in Section 3.2.1.2 is subsequently analyzed in the experimental setup. The signal utilized for the two-level DC injection method is displayed in Figure 6.3. The corresponding simulation is presented in Figure 3.5. In Figure 6.3 (a), the dq currents accurately adhere to their references.

In the experimental setup shown in Figure 6.3 (b), the voltage on the d-axis appears higher compared to the ideal scenario depicted in Figure 3.5 (b), as expected. This difference stems from the fact that, in the former case, the voltage drop is influenced by both the system's overall resistance and the inverter's non-linearity, whereas in the latter case, it is primarily governed by the machine's resistance.

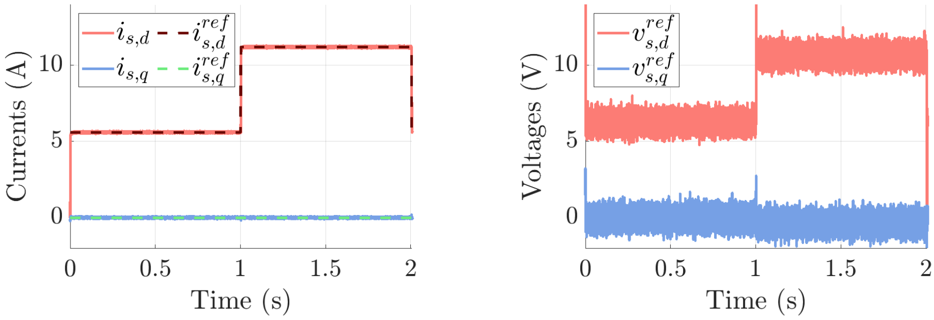

(a) Reference currents.

(b) Output voltages.

Figure 6.3: Two levels DC injection with CC, step at 1 s from $0.5 I_{sn}$ to I_{sn}, without $t_{\triangle}$ compensation.

The system resistance is identified with Equation (3.2). In this method, there is no need to apply the LUT for the R_s estimate because Equation (3.2) gives directly the slope in the linear region of the characteristic voltage-current in Figure 3.4.

6.1.1.3 Multiple-level DC injection and LUT identification

For the multiple-level DC injection, the reference voltage and the measured current are shown in Figure 6.4. The number of steps is determined visually. Initially, 30 steps are taken between zero and a phase voltage of 5 V, followed by 12 steps until reaching the maximum value of 12 V, which corresponds to the rated current. For each step, the current and voltage values are recorded by averaging the samples within an observation window once the signals reach a steady state. These recorded data points are represented as dots in Figure 6.5 and Figure 6.6.

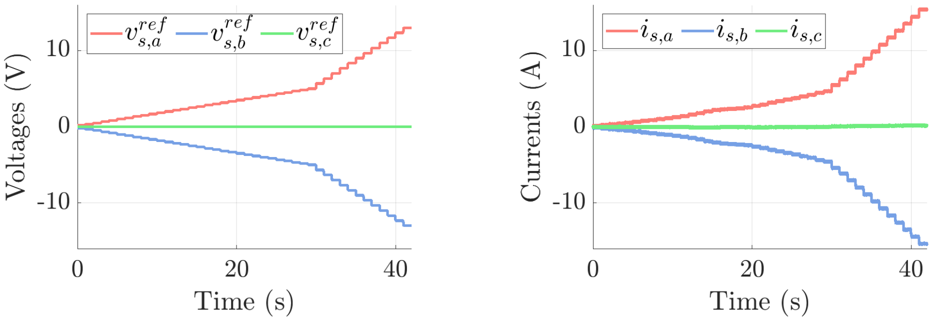

(a) Reference voltages.

(b) Measured currents.

Figure 6.4: Multiple levels DC injection in OL, steps of 1 s.

Figure 6.5 reports the characteristic phase voltage-phase current ($v_{s,a}^{ref}$, $I_{s,a}$) and the ideal linear curve $R_s I_{s,a}$. The slope of the linear curve represents the motor and cables' linear resistive elements. The difference between the ideal ($R_s I_{s,a}$) and the reference curve ($v_{s,a}^{ref}$) represents the non-linearity, and it is used to compensate for the voltage reference values generated by the control algorithm, to obtain a close match between the reference and the real phase voltage.

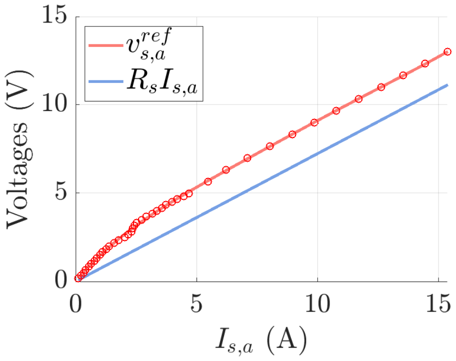

Figure 6.5: $v_{sa}^{ref} = f(I_{s,a})$ for R_s estimation.

The voltage error $v_{err} = v_{s,a}^{ref} - R_s I_{s,a}$ is then shown in Figure 6.6, where the blue dots are the data and the red curve represents the fit.

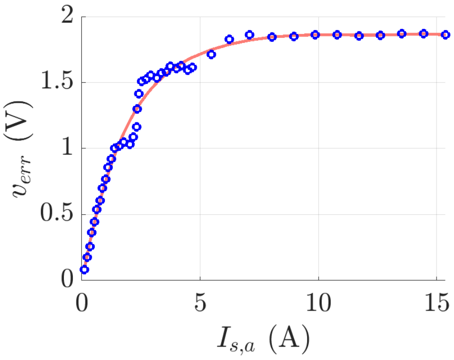

Figure 6.6: $v_{err,a} = f(I_{s,a})$ for inverter non-linearity compensation.

6.1.1.4 Comparison between the different DC tests

The numerical results of the system resistance for the three estimation methods are given in Table 6.1 (second column). The errors to the measured value are calculated in the third column. The last method performs better than the others. For this reason, its result is suggested as a value to take into account for the tuning of the gains for the FOC.

Table 6.1: Comparison between stator resistance resulting from different methods, measured value of $0.705\ \Omega$ (Brymen BM785 multimeter).

Method	Estimate (Ω)	$\frac{estmate-measure}{measure}$ (%)
One-level DC current injection (No LUT)	0.937	32.9
One-level DC current injection (With LUT)	0.729	3.4
Two-level DC current injection	0.759	7.7
Multiple-level DC voltage injection	0.724	0.0

6.1.2 SPMSM synchronous inductance

6.1.2.1 AC method

In the SPMSM, the currents are injected in the stator winding generating a rotating magnetic field. Unlike externally supplied rotors, the rotor in an SPMSM incorporates surface-mounted PM. Consequently, the synchronous inductance L_s is primarily associated with the fluxes on the stator side.

The AC method detailed in Section 3.2.2.1 involves injecting a high-frequency (300 Hz) signal of d-axis current, with a peak current value equal to the rated value of $11.2\sqrt{2}$ A. The q-current is kept to zero to avoid torque generation. Voltage compensation is performed using the LUT depicted in Figure 6.6.

The actual current follows the sinusoidal reference in the d-axis thanks to the PR controller, as shown in Figure 6.7 (a). The action of the PR controller results in a distorted output voltage (v_{sd}^{ref}) in Figure 6.7 (b). Its fundamental component (v_{sd}^{fund}), used in the calculation of the synchronous inductance, is hence extracted with the DFT.

The result of the synchronous inductance with the AC method is $L_s = 5.5$ mH.

This method is very sensitive to the phase shift errors of the measured waveform. Compensation for the PWM delay ($T_d = 1.5T_s$) is conducted according to the theory outlined in Section 5.1. This phase delay is introduced by the analogs set up, by the PWM and the ADC block, due to the sampling process.

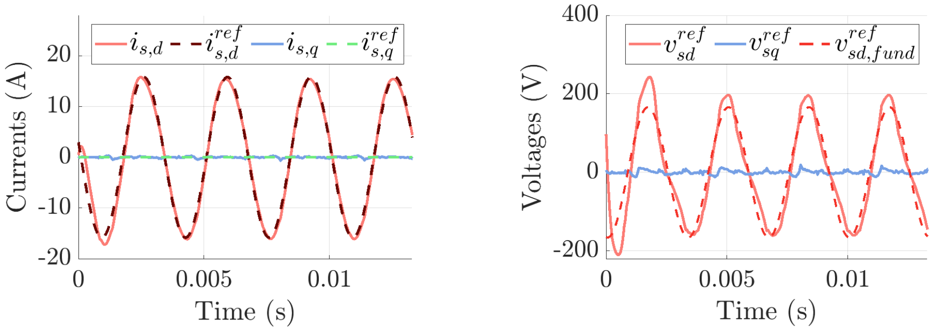

(a) Measured and reference currents.

(b) Reference voltages.

Figure 6.7: Current injection at a frequency of 300 Hz in dq0 reference frame.

6.1.2.2 DC+AC method

This section presents the experimental outcomes corresponding to the theory outlined in Section 3.2.2.2. The DC component of the reference current undergoes nine arbitrary steps, ranging from zero to the rated peak value of $11.2\sqrt{2}$ A. Additionally, an AC component, with a peak of 2 A, is superimposed onto the DC current. For each setpoint, the data concerning the reference voltage and reference current, utilized for the inductance calculation, are recorded. To ensure steady-state conditions, each step is maintained for a duration of three seconds. Subsequently, upon extracting the fundamental component of voltage and current using the DFT, the synchronous inductance is calculated for each setpoint. The resultant characteristic (i_{sd}, L_s) is depicted in Figure 6.8. The experiment produces the same result, regardless of the peak AC current value.

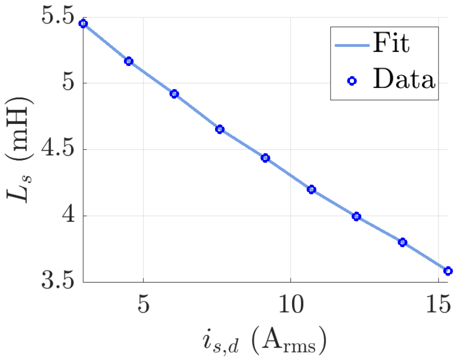

Figure 6.8: d-axis saturation characteristic with AC+DC injection at frequency of 300 Hz.

Due to the design of the SPMSM, the flux primarily travels through the air gap. Consequently, the saturation characteristic depicted in Figure 6.8 exhibits minimal saturation effects of the stator. This contrasts with the behavior observed in the IM, as will be discussed in Section 6.2.2.

6.1.2.3 Hysteresis control

The outcomes about the theory discussed in Section Section 3.2.2.3 are outlined in this section. The square wave reference voltage injected into the d-axis is depicted in Figure 6.9 (a). The output voltage of the hysteresis controller is arbitrarily chosen as ± 230 V for the d-axis and zero for the q-axis, intended to prevent torque generation and hence rotor movement. Subsequently, the corresponding measured current in the dq0 reference frame is presented in Figure 6.9 (b). This waveform can be juxtaposed with the simulated current depicted in Figure 3.11 (b), where constant inductance is assumed. Through this comparison, the smoothing effect of saturation on the rising fronts of the triangular waveform becomes evident, with the zero current marking an inflection point. Lastly, the flux resulting from the voltage integrator is illustrated in Figure 6.9 (c).

Once the experimental waveforms in Figure 6.9 are recorded, the resulting inductance can be extracted from the flux and the current with the discrete derivative in Equation (3.13). In conclusion, the saturation characteristic in Figure 6.10 (a) is obtained by plotting the flux versus current of the d-axis. The synchronous inductance, the slope of the saturation characteristic, is plotted versus the d-axis current in Figure 6.10 (b).

From Figure 6.10 (b), the unsaturated value of synchronous inductance, taken at zero current, is 6.7 mH. As observed in the simulation conducted in Section Section 3.2.2.3, the drift of the voltage integrator is also evident in the experimental tests, manifesting as an offset in the characteristic depicted in Figure 6.10 (a). The integrator's behavior is influenced by the initial condition of the reference voltage and the sampling frequency. Furthermore, the drift worsens with increasing time, necessitating the limitation of the acquisition window.

In this study, the voltage is injected for a duration of 100 ms. This duration corresponds to 2000 time samples based on the switching period. Following the 100 ms period, the reference voltage is reset to zero.

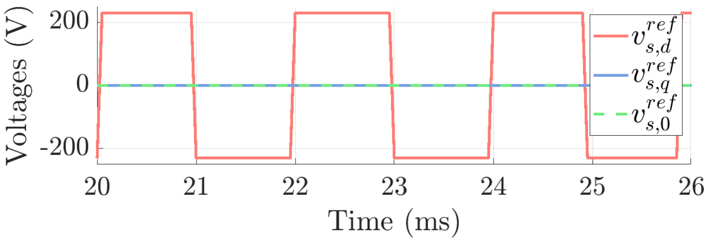

(a) Voltage.

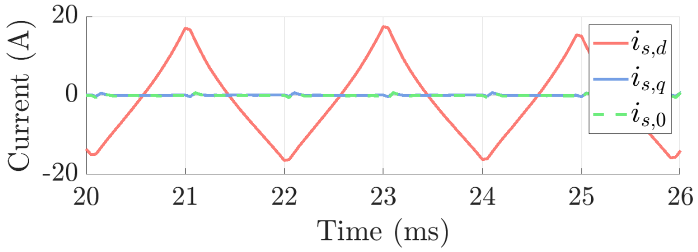

(b) Current.

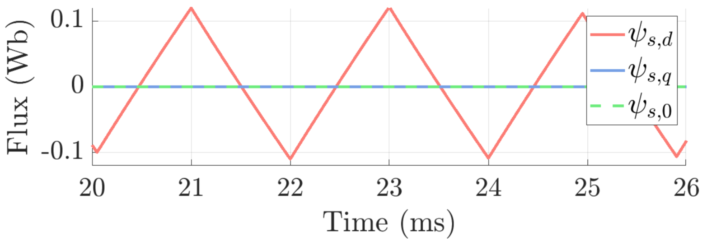

(c) Flux.

Figure 6.9: Hysteresis control experimental waveform in dq0 reference frame.

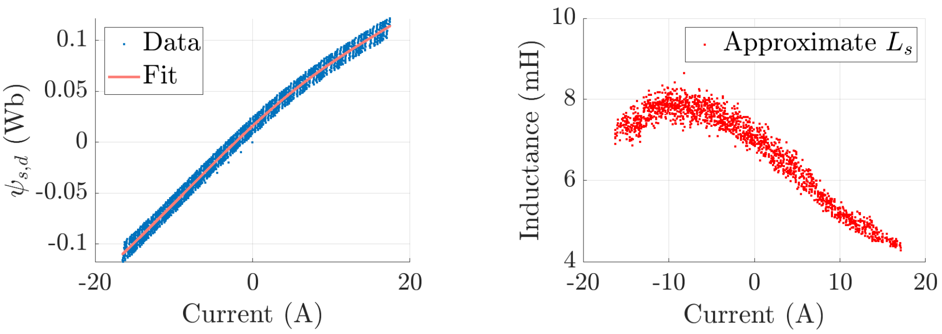

(a) d-axis saturation characteristics at $i_{s,q} = 0$.

(b) Slope of the d-axis saturation characteristics at $i_{s,q} = 0$.

Figure 6.10: Hysteresis control on the d-axis.

6.1.2.4 Short-circuit test

The experimental results corresponding to the theory exposed in Section 3.2.2.4 are subsequently presented.

First, the safety conditions are verified by calculating the short circuit current, which results to be double the maximum allowed current value from the datasheet in Table 5.3 ($I_N^{max} = 34.9$ A$_{\text{pk}}$, $I_{sc} = 67$ A$_{\text{pk}}$). For this reason, a mainly inductive external impedance of around 4 mH is placed in series to each machine phase. The resistive part of the external impedance is roughly $0.1\ \Omega$. The three external impedances are measured with the LCR. From these measurements, it is noticed that the load is unbalanced, so the results correspond to the average values between the phases. From the datasheet, the SPMSM impedance is 4.24 mH. As a result, the impedance of the entire system is almost doubled and the safety conditions are satisfied. The new short circuit current is calculated based on the new system impedance to verify it satisfies the safety conditions. Notice that the theoretical calculations of the peak value of the phase current are confirmed by the experiment in Figure 6.11 (b).

To prevent the SPMSM from over-current, the protection system in the B-Box (depicted in Figure 5.4 (a)) is set to the maximum allowed current ($I_N^{max} = 34.9$ A$_{\text{pk}}$ from Table 5.3).

By testing, the torque capability of the IM is enough to supply the short-circuit torque to the SPMSM. Hence, the short circuit is applied before the start of the experiment. For this reason, the high currents at the start of the machine are avoided, as shown in Figure 6.11 (b).

From the theory, the short-circuit current is estimated to be just in the d-axis, and its negative value led to possible risks of demagnetization. This is confirmed by the experimental waveform in Figure 6.11 (a).

The shown test in this section is performed by accelerating the IM up to 2000 rpm, which corresponds to the rated speed of the SPMSM. To investigate the impact of varying machine speeds on test performance, the test was conducted multiple times at different speeds (lower than the rated value); however, the result remained unaffected by the speed.

Once the IM is accelerated, the induced voltages in Figure 6.12 are recorded with differential voltage probes and visualized on the oscilloscope.

The unsaturated synchronous inductance from the short circuit test is $L_s = 4.28$ mH, confirmed by the LCR measurement.

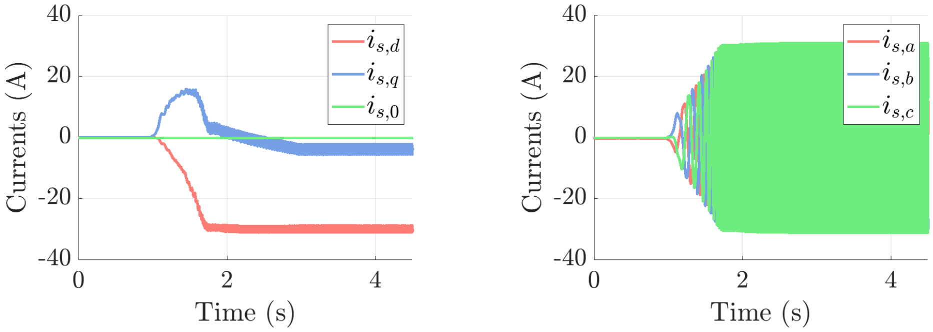

(a) SPMSM currents in dq0 reference frame.

(b) SPMSM currents in the abc reference frame.

Figure 6.11: Measured current with DIN50 at rated frequency during the short circuit test.

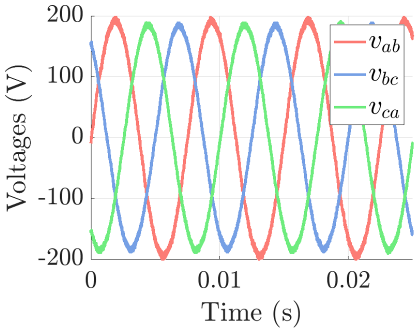

Figure 6.12: Short circuit test SPMSM line-to-line induced voltages at rated speed in the abc reference frame recorded with differential voltage probes and visualized on the oscilloscope.

6.1.2.5 Comparison between the different identification methods for the synchronous inductance

In this section, the results from the three estimation methods are summarized in Table 6.2. The estimates of the unsaturated synchronous inductance are in the second column. The errors to the datasheet value and the short circuit value are calculated in the third and fourth columns respectively.

The short circuit value is chosen as a benchmark for the unsaturated value because by short-circuiting the stator winding, the stator magnetic field is almost completely neutralized by the reaction of the rotor. It would be perfectly canceled out if there were no resistors. As a consequence, the magnetic material under these conditions is almost linear, even at the rated current.

In the AC+DC injection and hysteresis control method the unsaturated value corresponds to the set point of the saturation characteristic in which the current is around zero. Specifically, notice that the unsaturated value of the AC+DC injection corresponds to the value estimated with the AC method.This result confirms the theory that the amplitude of the injected sinusoidal signal does not change the saturation state of the machine and hence, it does not affect the estimation of the synchronous inductance.

The confidence in the synchronous inductance result from the standard tests is increased by the LCR measurement instrument, which has very high accuracy. A possible explanation for the discrepancy in inductance identification could be found considering that the SPMSM is a low reactance machine. In fact, during the study of the saturation characteristic, the impedance phase monotonically increases with the current in a range between $78°$ and $88°$. Hence the SPMSM inductance is very sensitive to compensation of PWM phase delay introduced by the experimental drive system. Another observation is that due to its mostly isotropic structure, the SPMSM is not particularly sensitive to the saturation effect, with a reduction of inductance of around 35% from the estimated unsaturated value. A possible way to understand if this error is acceptable for control performance is to check its effect on the dynamic response of the FOC.

Table 6.2: Comparison between the unsaturated values of the synchronous inductance resulting from different methods, datasheet value of 4.24 mH and the measured value of 4.28 mH from the short circuit test.

Method	Estimate (mH)	$\frac{estmate-datasheet}{datasheet}(\%)$	$\frac{estmate-measure}{measure}(\%)$
AC injection	5.5	29.7	28.5
AC+DC injection	5.5	29.7	28.5
Hysteresis control	6.7	58.0	56.5

6.1.3 SPMSM PM-flux

6.1.3.1 I-f startup + sensorless FOC

In this section, the results related to the theory presented in Section 3.2.3.1 are described. The experimental test in Figure 6.13 matches the corresponding simulation in Figure 3.16. First, a reference mechanical ramp speed $\omega_{m,est}$

is set at t=0 s. The measured mechanical speed $\omega_{m,real}$ rises in OL. As a consequence, the tracking of the reference results in high oscillations of real speed. During the speed ramp, the q-axis current is controlled close to the rated peak value to provide the power necessary to the SPMSM to speed up. The rated value is not set as a reference of the CC because the current oscillations trigger the protection system in the power modules set to 1.2 the rated value of the current.

At 0.8 s, the constant speed of 800 rpm is reached. This value is arbitrarily chosen because it allows for a reduction of the amplitude of the speed oscillations at constant speed. These oscillations are due to a misalignment of the shafts in the test bench. This choice of speed prevents the SPMSM from heating up. Additionally, sensorless control mainly relies on the estimate of machine parameters for the back-EMF estimate. At higher speeds, the sensorless control is less sensitive to errors in the machine parameter estimate. As a consequence, the tracking of the estimated speed better matches the real one.

After 0.8 s the q-axis current starts to decrease, while the speed is kept constant. At t=2 s the reference current and the angle of the alignment error between the real and the virtual rotating reference frame are close to zero. So the control is switched to a sensorless FOC. The machine is not OL controlled anymore. Since the current is zero, the speed starts decreasing, as well as the phase voltage.

Their ratio results in the PM-flux estimate of 0.2814 Wb.

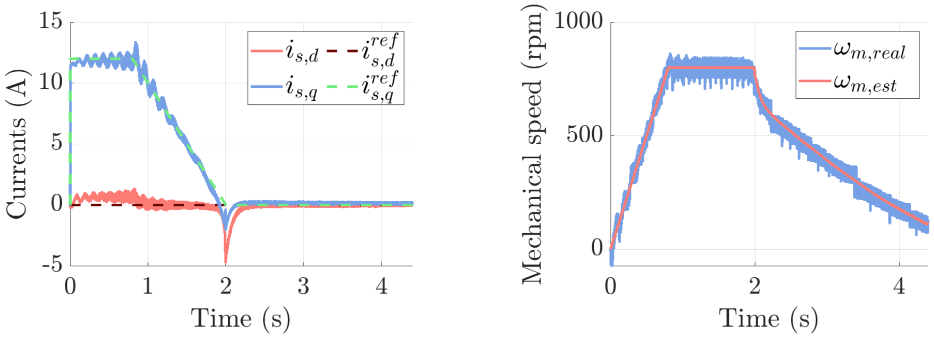

(a) Measured and reference currents.

(b) SPMSM mechanical speed ramp.

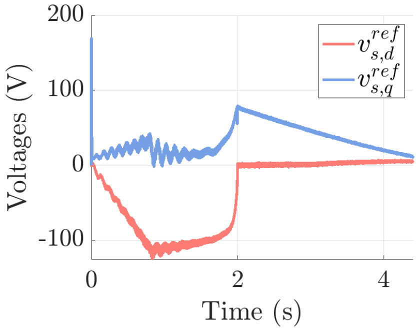

(c) Reference voltages.

Figure 6.13: Experimental I-f startup from t = 0 s and sensorless FOC at null references in dq0 reference frame introduced at t = 2 s.

6.1.3.2 Open-circuit test

The experimental results corresponding to the theory in Section 3.2.3.2 are shown in Figure 6.14. These match with the corresponding simulated test is in Figure 3.18.

In Figure 6.14 (a), the IM mechanical speed ω_{IM} follows the reference ω_{IM}^{ref} of 800 rpm. This value is chosen following the same reasoning presented in Section 6.1.3.1.

The SPMSM line-to-line voltages are shown in Figure 6.14 (b). They are measured with three differential voltage probes and visualized with an oscilloscope. Subsequently, the rms phase voltage is calculated per each phase. The resulting PM-flux estimation is given by the ratio between the average value of the three rms phase voltages and the synchronous electrical speed of the SPMSM. This speed is calculated knowing the IM mechanical speed and the pole pairs of the SPMSM.

In conclusion, the PM-flux estimation is 0.2814 Wb.

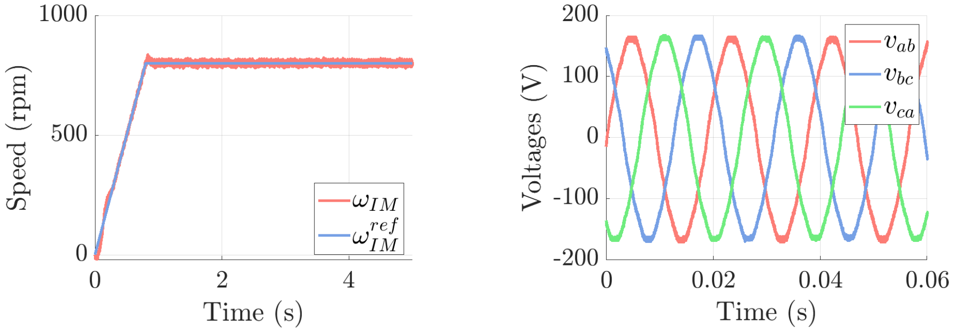

(a) IM mechanical speed.

(b) SPMSM back-EMF measurements.

Figure 6.14: Open-circuit test.

6.1.3.3 Comparison between the different identification methods for PM-flux

The result for the PM-flux is presented in table 6.3 where the estimated value using the I-f startup + sensorless FOC is in the first column. In the second column, this value is compared with the datasheet parameter provided by the machine's manufacturer SEW Eurodrive. In the third column, the error between the estimate and the result from the open-circuit test from the Standard IEEE 1812-2023 [5] is given.

Table 6.3: Comparison between PM-flux, datasheet value of 0.2748 Wb and value from the open-circuit test of 0.2814 Wb.

Estimate (Wb)	$\frac{estmate-datasheet}{datasheet}$ (%)	$\frac{estmate-measure}{measure}$ (%)
$0.281\,4$	2.4	0

6.2 Results for IM

6.2.1 IM stator resistance

The same methods used for the SPMSM in section 6.1.1, namely one-level, two-level, and multiple-level DC injection, are implemented for the IM.

The numerical results of the system resistance for the three estimation methods are given in Table 6.4 (second column). The errors to the measured value are calculated in the third column.

As for the SPMSM, the last method performs better than the first two. For this reason, just the waveforms related to the multiple-level DC injection method are subsequently shown.

Table 6.4: Comparison between stator resistance resulting from different methods, measured value of $1.115\ \Omega$ (Brymen BM785 multimeter).

Method	Estimate (Ω)	$\frac{estmate-measure}{measure}$ (%)
One level DC current injection (No LUT)	1.357	21.7
Two-level DC current injection	1.145	2.7
Multiple-level DC current injection	1.135	0.0

In Figure 6.15 (a), a total of 20 steps of reference voltages are executed, ranging up to 10 V. Subsequently, the number of steps is halved within the linear region between 10 V and 20 V. The number of steps is visually chosen. The phase currents, measured with the current sensors embedded in the power modules, are shown in Figure 6.15 (b).

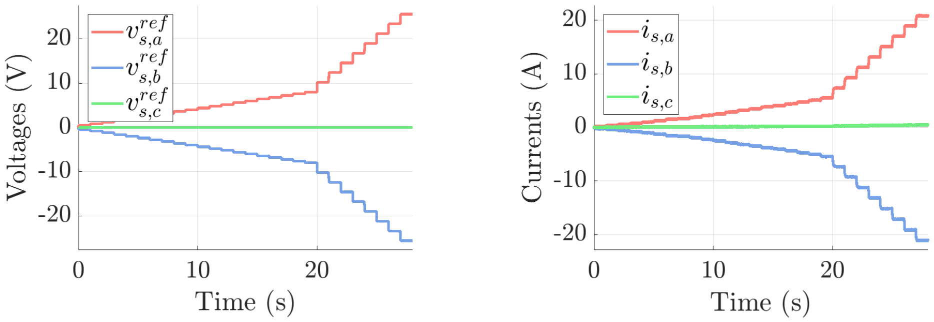

(a) Reference voltages.

(b) Measured currents.

Figure 6.15: Multiple levels DC injection in OL, steps of 1 s.

The characteristic phase current-phase voltage is shown in Figure 6.16.

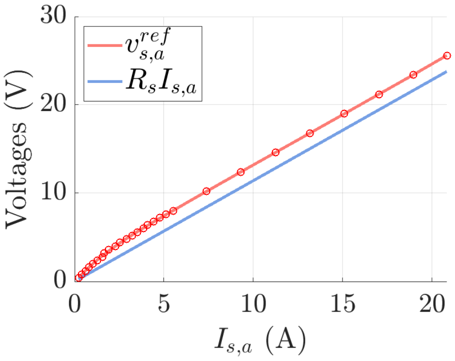

Figure 6.16: $v_{sa}^{ref} = f(I_{s,a})$ for Rs estimation.

The voltage error versus phase current characteristic, used to build the LUT for the inverter non-linearity compensation, is finally shown in Figure 6.17.

The channels of the power rack depicted in Figure 5.6 (a), to which the IM is connected, differ from those used for the SPMSM. Consequently, distinct power modules are utilized for the IM and the SPMSM, potentially introducing different non-linear behaviors into the system. Hence, the LUT is re-estimated for the IM. Upon comparing the LUT constructed for the SPMSM in Figure 6.6 with that built for the IM in Figure 6.17, it becomes apparent that the voltage error trend is similar. This observation enhances confidence in these experimental findings.

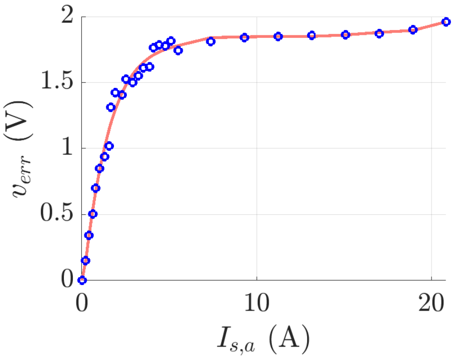

Figure 6.17: $v_{err,a} = f(I_{s,a})$ for inverter non-linearity compensation.

6.2.2 IM leakage inductance

6.2.2.1 DC+AC method

The first method to estimate the leakage inductance is the DC+AC injection presented in Section 3.3.2.1. The reference voltages, shown in Figure 6.18 (a), are injected in OL to create a single-phase configuration, ensuring a balanced load. The frequency of the injected signal is 300 Hz, chosen because of the reasons given in Section 3.3.2.1. An AC voltage component of arbitrarily 4 V peak is overlapped on 12 steps of the DC component. Each step lasts for 3 seconds, ensuring the inductance estimation is performed in steady state condition. The maximum voltage is chosen to give the rated peak current. The IM phase currents in Figure 6.18 (b) are then measured through the sensors in the power modules in Figure 5.7. For each set point the inductance is calculated from the fundamental components of voltage and current.

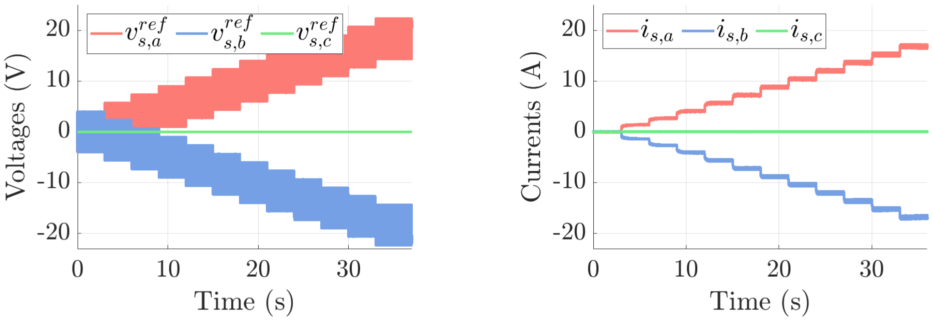

(a) Reference voltage.

(b) Measured current.

Figure 6.18: High frequency injection at 300 Hz.

The saturation characteristic of the leakage inductance is shown in Figure 6.19. The saturation behavior of the machine is related to the structure of the rotor. Specifically, the IM stator winding is inserted into the half-closed slot on the laminated stator core, as stated by the machine's manufacturer SEW Eurodrive [45].

In the case of a semi-closed slot, the bridges saturate by increasing the current. This phenomenon is modeled from a magnetic point of view by an increase in the opening. Without saturation, all the magnetic lines would have passed inside the bridge. In saturation conditions, the bridge has a permeability similar to that of the air.

For this reason, a semi-closed slot design is sensitive to saturation and the behavior shown in Figure 6.19 is compatible with the theory presented in

Electrical Machine by Cavagnino in [7].

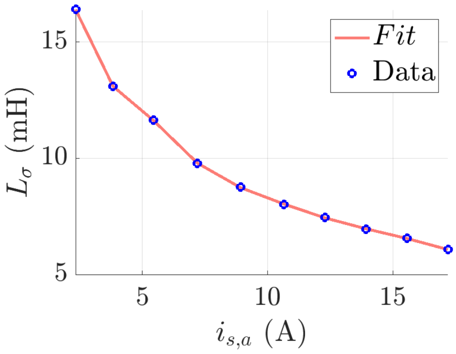

Figure 6.19: Saturation characteristic at a frequency of 300 Hz by DC+AC method.

In conclusion, the unsaturated value of the leakage inductance from Figure 6.19, corresponding to the set point at zero DC current injection, is 16.4 mH.

6.2.2.2 Locked rotor test

The second method used to identify the leakage inductance is the locked rotor test presented in Section 3.3.2.2. The current is measured through a current probe and the phase voltage with a differential voltage probe placed at the output of the inverter. The DFT is used to extract the fundamental component of phase voltage and current. The harmonic spectrum of the measured voltage and current is in Figure 6.20. These are used to calculate the impedance of the IM from Equation (3.30), which imaginary part is 16.7 mH. The real component of the IM impedance is 0.59 Ω.

6.2.2.3 Comparison between the different identification methods for the leakage inductance

The results from the two identification procedures are summarized in Table 6.5. The estimate of the unsaturated leakage inductance, from the self-commissioning method, is in the second column. The errors to the datasheet value and the locked rotor test result are presented in the third and fourth columns respectively.

During the locked rotor test, the magnetizing inductance is neglected because it is assumed to be much larger than the leakage inductance. However,

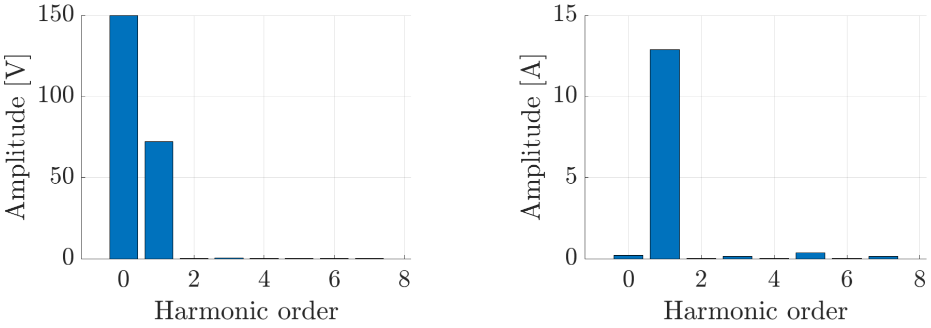

(a) Harmonic content of the measured voltage in the a-axis (v_{sa}).

(b) Harmonic content of the measured current in the a-axis (i_{sa}).

Figure 6.20: Harmonic content resulting from the DFT of current and voltage measurement in phase a.

in the experimental test, there may be some magnetic saturation, depending on the profile of the magnetization inductance. Despite this, the result from the locked rotor test is assumed to be the unsaturated value, since this eventual effect of magnetic saturation is negligible. This result is taken as a benchmark and it is compared to the set point in Figure 6.19 corresponding to a DC current component close to zero for the self-commissioning procedure.

Unlike the SPMSM, the IM is more sensitive to the saturation effect, as shown by the reduction of its leakage inductance of around 60% between zero and rated current. For this reason, the effect of saturation on control performance could result in larger variations of the control gains than in the SPMSM applications.

Table 6.5: Comparison between the unsaturated values of the leakage inductance resulting from different methods, datasheet value of 22.3 mH and the value of 16.7 mH from the locked rotor test.

Method	Estimate (mH)	$\frac{estmate-datasheet}{datasheet}(\%)$	$\frac{estmate-measure}{measure}(\%)$
AC+DC injection	16.4	-27.3	-2.3

6.2.3 IM rotor resistance

The results corresponding to the theory in Section 3.3.3 are presented. The three-phase reference voltages are injected in OL in a single-phase configuration. As shown in Figure 6.21 (a), the voltage in phase a is equal and opposite to the voltage in phase c. The amplitude of the DC component of the injected signal is arbitrarily chosen as 7 V to shift the signal to the linear region of the characteristic current - voltage. The AC component of the injected signal is arbitrarily chosen as 2 V. In this analysis, just one frequency is considered. However, the rotor resistance referred to the stator side (R_R) changes with the slip, and hence with the frequency of the injected signal. For a more complete analysis, the characteristic (R_R, f_l) has to be built as in the reference [8]. The measured current in the three-phase reference frame is finally given in Figure 6.21 (b). The waveforms are presented in the $\alpha\beta0$ reference frame, where the calculation for the rotor resistance estimation in Equation (3.39) is performed.

The rotor resistance estimated with this method is $0.63\ \Omega$.

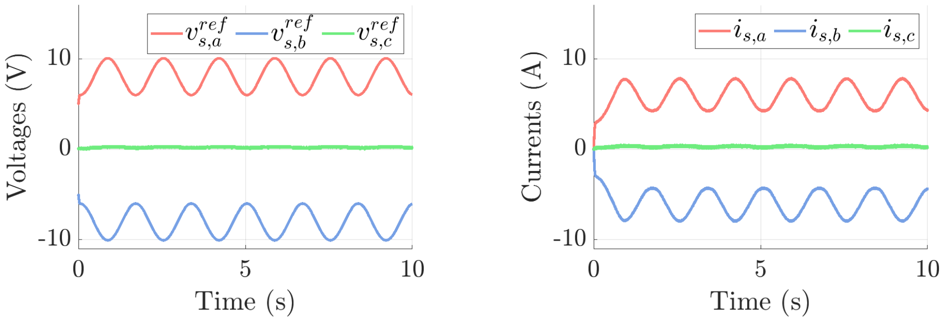

(a) Reference voltage.

(b) Measured current.

Figure 6.21: Single phase injection at a frequency of $f_l = 0.6$ Hz, $V_{sa,dc} = 7$ V, $V_{sa,ac} = 2$ V$_{\text{pk}}$ in the abc reference frame.

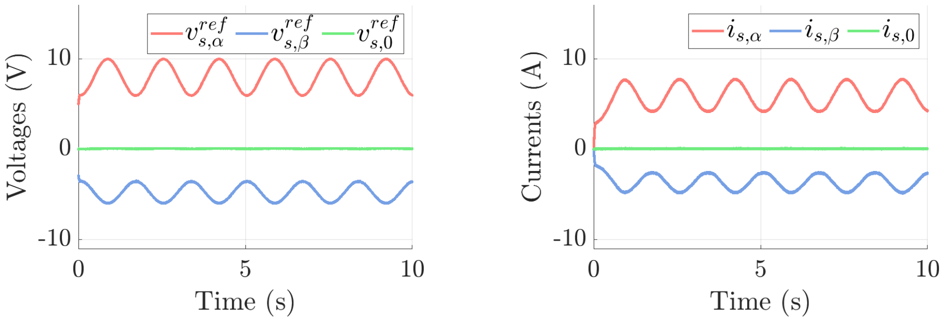

(a) Reference voltage.

(b) Measured current.

Figure 6.22: Single phase injection at a frequency of $f_l = 0.6$ Hz, $V_{dc} = 7$ V, $V_{ac} = 2$ V$_{\text{pk}}$ in the $\alpha\beta0$ reference frame.

The second identification method of rotor resistance is the standard locked rotor test from IEEE 112-2017 [3] given in Section 3.3.2.2. The total value of the machine resistance R_{tot} is given by this test. By subtracting the stator resistance R_s, the rotor resistance referred to the stator side in the inverse-gamma equivalent circuit is $R_R = R_{tot} - R_s$.

6.2.3.1 Comparison between the different identification methods for the rotor resistance

The results for the rotor resistance are summarized in table 6.6. The estimated value with the self-commissioning procedure from the reference [8] is presented in the first column. In the second column, this value is compared with the rotor resistance calculated from the datasheet parameter provided by the machine's manufacturer SEW Eurodrive from Table 5.2. The datasheet provides information on the standard T-equivalent circuit. So the rotor resistance from the datasheet is transformed into the inverse-gamma equivalent circuit by using the formula in Equation (2.39). In the third column, the error between the estimate and the result from the locked rotor test is given.

Table 6.6: Comparison between rotor resistance resulting from different methods, datasheet value of $0.65\ \Omega$ and locked rotor test result of $0.59\ \Omega$.

Estimate (Ω)	$\frac{estmate-datasheet}{datasheet}$ (%)	$\frac{estmate-measure}{measure}$ (%)
0.63	3	6.8

Chapter 7

Conclusions and Future work

7.1 Conclusions

In industrial settings, a common challenge associated with electrical machines is the lack of parameters, which are not always available from the machine manufacturer. These parameters play a crucial role in tuning the control gains for the Field Oriented Control (FOC).

Traditional parameter identification methods often rely on standard IEEE tests. However, implementing these tests can be impractical as they necessitate additional equipment that may be costly and not readily accessible. Additionally, they may require specific configurations, such as coupling with the load, which can be challenging for machines already installed on-site.

The self-commissioning procedures propose a solution to this problem. Self-commissioning for AC motor drives, addressed in this thesis, typically refers to the process of calibration, identification of machine parameters, and automatic tuning of control gains for a motor drive system. It is a standstill procedure that utilizes signal injection through a power converter and the available sensors with minimal operator intervention. It can be performed when the machine is operated (online) or one time before it starts up (offline).

This thesis aims to answer the research question of how can a state-of-the-art automatic identification procedure of parameters be implemented for the Imperix motor testbench, which is composed of Induction Machine (IM) and Surface Mounted Permanent Magnet Synchronous Machine (SPMSM).

To answer this research question the following goals were reached.

First, the electrical parameters to be identified were selected, based on the machine equivalent circuit used for the FOC. For the SPMSM the studied parameters were the stator resistance, the synchronous inductance, and the Permanent Magnets (PM)-flux. For the IM the stator resistance, the leakage inductance, the rotor resistance, and the magnetizing inductance were identified.

A literature review regarding the parameter identification was performed. The references were analyzed and categorized based on the control configuration (open or closed-loop), and whether the method considers non-idealities on parameter identification, such as the effects of inverter non-linearity, saturation, or frequency.

Per each parameter, suitable methods were selected and implemented in simulation first, and then experimentally tested. To validate the self-commissioning procedure, the obtained results had to conform to those obtained following the IEEE standards, which were chosen as a benchmark.

The stator resistance was identified with one-level, two-level, and multiple-level DC steps. This parameter is sensitive to inverter non-linearity, whose effect was compensated through the characteristic voltage error-phase current used to build the Lookup Table (LUT) inserted in the control algorithm. The IEEE standards identify the stator resistance through measurements from the multimeter.

The result of the stator resistance analysis is that the multiple DC identification method aligned better with the standard than the first two estimation procedures. For this reason, its result was suggested as a value to take into account for the tuning of the gains for the FOC. Other benefits of the multiple-level DC injection were that both stator resistance and inverter non-linearity characteristic were identified from the same signal injected and its Open Loop (OL) nature. Unlike the one and two-level injection, the multiple-level injection avoids the necessary Current Controller (CC) tuning, leading to a more time-efficient identification routine.

Then, the high-frequency sinusoidal injection, with and without the DC bias, and the square wave voltage injection through hysteresis control were used to identify the synchronous inductance and its saturation characteristic. The IEEE standard suggests the short circuit test to obtain the unsaturated synchronous inductance.

This result was compared with the unsaturated value from the three self-commissioning methods, resulting in considerable errors between them.

The last SPMSM parameter under study was the PM-flux, which was identified by rotating the SPMSM using the IM as a prime mover in open circuit configuration. This deviation from the standstill constraint of the self-commissioning procedure was necessary as the PM's effect becomes visible only when the rotor speed is non-zero. The result of this procedure aligns with the result from the standard open circuit test IEEE, increasing the confidence in the hypothesis.

It can be concluded that, for the SPMSM, the self-commissioning procedure allows parameter identification with results almost aligned with the standard tests, except for discrepancies in unsaturated SPMSM synchronous inductance estimation. The confidence in the synchronous inductance result from the standard tests is increased by the LCR measurement instrument, which has very high accuracy. A possible explanation for the discrepancy in inductance identification could be that the self-commissioning method applied to low reactance machines is very sensitive to the PWM phase delay introduced by the experimental drive system.

Subsequently, the IM parameters are discussed. The stator resistance was identified with the same procedures described for the SPMSM. The conclusions drawn for the SPMSM were confirmed also for the IM.

The leakage inductance of the IM was identified with the high-frequency sinusoidal injection with stepped DC bias to build the saturation characteristic. The unsaturated value, corresponding to the set point of the characteristic at zero direct current, aligned with the imaginary part of the impedance obtained from the locked rotor test as recommended by the IEEE standard.

The rotor resistance referred to the stator side was estimated with low-frequency sinusoidal injection with DC bias. The outcome of this identification method matched with the real part of the impedance identified from the locked rotor test.

The magnetizing inductance was not determined in this work because of the extensive nature of the problem and time constraints.

It can be inferred that the self-commissioning strategies tested on the IM are technically relevant because their outcomes are comparable with the IEEE standard tests, widely accepted by the scientific community. Unlike the SPMSM, the IM is more sensitive to the saturation effect. For this reason, the effect of saturation on control performance could result in larger variations of the control gains than in the SPMSM applications.

Overall, this work has given rise to the following general conclusions:

- The use of reference voltage for parameter estimation is possible if the inverter non-linearity is carefully compensated by including a LUT in the control algorithm, eliminating the need for additional voltage measurements. This highlights the benefit of using self-commissioning to the standard tests, which necessitate additional equipment that may be costly and not readily accessible.

- According to the literature, saturation is frequently overlooked in control algorithms. However, its integration (simply using a LUT) enables the dynamic adjustment of gains, potentially enhancing control performance. Unlike conventional tests, the self-commissioning procedure provides insight into both unsaturated and saturated machine behavior.

7.2 Limitations

This section discusses the limitations of the results presented in Chapter 6.

- Investigate why the compensation of the inverter non-linearity is achieved at around 60% of the expected theoretical drop (1.8 V instead of 3 V).
- Investigate the reason why the inductance results in higher values if estimated with the self-commissioning algorithms.

7.3 Future work

This section addresses the possible improvements that should be prioritized in future work.

- Estimate the magnetizing inductance. The corresponding literature review is given in Section 3.1.2.4 in which some potential methods are proposed. The traditional sinusoidal single-phase test with ([54]) or without ([39]) the DC bias is a possible self-commissioning procedure to be tested in simulation and experiment. A benchmark for the magnetizing inductance estimate is given by the no-load test from the Standard IEEE 112-2017 [3].
- Automate the procedure. Once the parameters are identified with good accuracy, the procedure should be automated for both machines. The signals are sequentially injected into the electrical drive. This can be done with a state machine in Simulink. A prototype is created for the SPMSM. However, the estimation for the SPMSM synchronous inductance can be improved. So the final version of the procedure could be further developed. Similarly, the procedure can be automatized for the IM once all the techniques for the parameter identification are defined.

Notice that, once the self-commissioning algorithm becomes more complex, the states and their interaction would result in a chaotic vision. A directly coded function is for this reason suggested in place of the state machine.

- Validate the effectiveness of the FOC utilizing the newly identified machine parameters obtained through the self-commissioning procedure. Next, contrast this performance with that achieved using gains tuned based on parameters provided by the manufacturer. Finally, assess whether there is an enhancement in control performance.
- Extension to the online estimation of machine parameters, especially for the resistances. As already stated in this report, the temperature considerably affects the value of the resistance, which is a key parameter for control performance. For instance, its variations can be tracked by a resistance observer like in [55].
- Extension to other machines. In this work, both machines have a similar power rating of around 4 kW. A possible future analysis would be to validate the proposed self-commissioning procedure on machines of different power ratings.
- Extension to mechanical parameters identification, important for the tuning of the SC in the FOC strategy. This project focuses on the electrical parameters as said in Section 1.5. However, the control performance can be further improved if the mechanical aspects are taken into account. Some already existing works present a solution for this problem such as in [19], which uses signal injection for the parameters estimation.
- Evaluate the impact of the frequency variations on control performance. Possible solutions are proposed in [8] by analyzing the characteristic rotor resistance-slip frequency, or considering the influence on the impedance due to current distribution in the rotor bars like in [36].
- Investigate the effect on control performance of saturation characteristic, if it is considered as a two-variable function of both flux and current such as in [15].
- Test the feasibility of the quasi-steady state technique for the PM-flux identification on the SPMSM, normally developed for the SynRM like in [32].

References

[1] P. Vas, *Vector control of AC machines*, ser. Monographs in electrical and electronic engineering ;, 22, Oxford science publications. Clarendon Press ; Oxford University Press, Oxford [England], New York, 1990, 1990. ISBN 0198593708 [Pages 1, 34, 35, 37, 39, and 41.]

[2] S. A. Odhano, "Self-commissioning of ac motor drives," *Porto Institutional Repository*, 2014. doi: https://iris.polito.it/handle/11583/2543100 [Pages 2, 12, 20, 27, 29, 30, 31, 32, 34, 35, 36, 37, 38, 39, 40, 41, 42, 44, 46, and 50.]

[3] I. Societies and the Standards Coordinating Committe, "Ieee standard test procedure for polyphase induction motors and generators," *IEEE Std 112-2017 (Revision of IEEE Std 112-2004)*, pp. 1–115, 2018. doi: 10.1109/IEEESTD.2018.8291810 [Pages 2, 4, 12, 34, 36, 38, 41, 42, 64, 67, 104, and 108.]

[4] S. A. Odhano, P. Pescetto, H. A. A. Awan, M. Hinkkanen, G. Pellegrino, and R. Bojoi, "Parameter identification and self-commissioning in ac motor drives: A technology status review," *IEEE Transactions on Power Electronics*, vol. 34, no. 4, pp. 3603–3614, 2019. doi: 10.1109/TPEL.2018.2856589 [Pages 2 and 27.]

[5] IEEE, "Ieee guide for testing permanent magnet machines," *IEEE Std 1812-2023 (Revision of IEEE Std 1812-2014)*, pp. 1–88, 2023. doi: 10.1109/IEEESTD.2023.10352399 [Pages 4, 28, 30, 31, 33, 42, 55, 57, and 97.]

[6] L. Harnefors, M. Hinkkanen, and O. Wallmark, *Control of Voltage-Source Converters and Variable-Speed Drives*, Course of Control in Electrical Energy Conversion EJ2230, KTH, 2023. [Page 6.]

[7] A. Cavagnino, "Electrical machines ii, part of electromechanical constructions, three-phase induction machine," 2019. [Pages 7, 56, and 101.]

[8] L. Peretti and M. Zigliotto, "Automatic procedure for induction motor parameter estimation at standstill," *Electric Power Applications, IET*, vol. 6, pp. 214–224, 04 2012. doi: 10.1049/iet-epa.2010.0262 [Pages 8, 18, 28, 29, 30, 31, 32, 34, 35, 36, 37, 38, 39, 41, 42, 47, 51, 65, 103, 104, and 109.]

[9] N. Mohan, T. M. Undeland, and W. P. Robbins, *Power Electronics: Converters, Applications and Design*. John Wiley & Sons Inc 1989, 1989. [Page 20.]

[10] M. Ruff, A. Bunte, and H. Grotstollen, "A new self-commissioning scheme for an asynchronous motor drive system," in *Proceedings of 1994 IEEE Industry Applications Society Annual Meeting*, vol. 1, 1994. doi: 10.1109/IAS.1994.345457 pp. 616–623 vol.1. [Pages 21 and 35.]

[11] S. Strobl, N. Cherix, and G. Fernandez, "Rotor field-oriented control (rfoc) of an induction machine," Jul 2023. [Online]. Available: https://imperix.com/doc/implementation/rotor-field-oriented-control [Page 23.]

[12] K. J. Åström and T. Hägglund, *Advanced PID Controls*. CRC Press, Boca Raton, FL, 1995, 1995. [Page 24.]

[13] Y. Shi, K. Sun, L. Huang, and Y. Li, "Online identification of permanent magnet flux based on extended kalman filter for ipmsm drive with position sensorless control," *IEEE Transactions on Industrial Electronics*, vol. 59, no. 11, pp. 4169–4178, 2012. doi: 10.1109/TIE.2011.2168792 [Page 28.]

[14] A. Bechouche, H. Sediki, D. Ould Abdeslam, and S. Haddad, "A novel method for identifying parameters of induction motors at standstill using adaline," *IEEE Transactions on Energy Conversion*, vol. 27, no. 1, pp. 105–116, 2012. doi: 10.1109/TEC.2011.2175393 [Page 28.]

[15] T. Tuovinen, M. Hinkkanen, and J. Luomi, "Modeling of saturation due to main and leakage flux interaction in induction machines," *IEEE Transactions on Industry Applications*, vol. 46, no. 3, pp. 937–945, 2010. doi: 10.1109/TIA.2010.2045210 [Pages 28, 36, 41, and 109.]

[16] K. Wang, W. Yao, B. Chen, G. Shen, K. Lee, and Z. Lu, "Magnetizing curve identification for induction motors at standstill without assumption of analytical curve functions," *IEEE Transactions on Industrial Electronics*, vol. 62, no. 4, pp. 2144–2155, 2015. doi: 10.1109/TIE.2014.2354012 [Pages 28, 34, 35, 36, 37, 39, 40, and 41.]

[17] L. Kalamen, P. Rafajdus, P. Sekerak, and V. Hrabovcova, "A novel method of magnetizing inductance investigation of self-excited induction generators," *IEEE Transactions on Magnetics*, vol. 48, no. 4, pp. 1657–1660, 2012. doi: 10.1109/TMAG.2011.2173312 [Pages 28, 40, and 41.]

[18] J. Kania, T. Panchal, V. Patel, and K. Patel, "Self commissioning: A unique feature of inverter-fed induction motor drives," *IEEE Transactions on Industrial Electronics*, 12 2011. doi: 10.1109/NUiConE.2011.6153302 [Pages 28, 35, 37, 38, 40, and 41.]

[19] C. Yang, B. Song, Y. Xie, S. Lu, and X. Tang, "Speed-controller-independent mechanical parameter identification in spmsm drive achieved via signal injection," *IEEE Transactions on Industrial Electronics*, vol. 70, no. 2, pp. 1282–1297, 2023. doi: 10.1109/TIE.2022.3161760 [Pages 28, 30, 33, and 109.]

[20] Y.-S. Lai and M.-H. Ho, "Self-commissioning technique for high bandwidth servo motor drives," in *2017 IEEE Energy Conversion Congress and Exposition (ECCE)*, 2017. doi: 10.1109/ECCE.2017.8095802 pp. 342–349. [Page 28.]

[21] M. Marchesoni, M. Passalacqua, L. Vaccaro, M. Calvini, and M. Venturini, "Low speed performance improvement in a self-commissioned sensorless pmsm drive based on rotor flux observer," in *2019 21st European Conference on Power Electronics and Applications (EPE '19 ECCE Europe)*, 2019. doi: 10.23919/EPE.2019.8915004 pp. P.1–P.10. [Pages 29, 30, 31, and 32.]

[22] S. Odhano, M. Tang, A. Formentini, P. Zanchetta, and R. Bojoi, "Identification of linear permanent magnet synchronous motor parameters and inverter non-linearity effects," in *2018 International Symposium on Power Electronics, Electrical Drives, Automation and Motion (SPEEDAM)*, 2018. doi: 10.1109/SPEEDAM.2018.8445214 pp. 26–32. [Pages 29 and 30.]

[23] I. Bojoi, E. Armando, G. Pellegrino, and S. Rosu, “Self-commissioning of inverter nonlinear effects in ac drives,” in *2012 IEEE International Energy Conference and Exhibition (ENERGYCON)*, 2012. doi: 10.1109/EnergyCon.2012.6347755 pp. 213–218. [Pages 29, 33, 34, and 35.]

[24] M. Vučković, B. Dumnić, V. Vasić, B. Vujkov, and V. Popović, “Inductance identification of the surface permanent magnet synchronous machines with sinusoidal voltage test signals,” in *2021 21st International Symposium on Power Electronics (Ee)*, 2021. doi: 10.1109/Ee53374.2021.9628325 pp. 1–6. [Pages 31 and 32.]

[25] N. Bedetti, S. Calligaro, and R. Petrella, “Stand-still self-identification of flux characteristics for synchronous reluctance machines using novel saturation approximating function and multiple linear regression,” *IEEE Transactions on Industry Applications*, vol. 52, no. 4, pp. 3083–3092, 2016. doi: 10.1109/TIA.2016.2535413 [Pages 31, 32, 42, 52, and 55.]

[26] H.-J. Lee, J.-E. Joo, and Y.-D. Yoon, “Standstill sensorless self-commissioning strategy of synchronous machine considering rotor rotation reduction technique,” in *2022 International Power Electronics Conference (IPEC-Himeji 2022- ECCE Asia)*, 2022. doi: 10.23919/IPEC-Himeji2022-ECCE53331.2022.9807050 pp. 2694–2700. [Pages 31 and 32.]

[27] P. Pescetto and G. Pellegrino, “Sensorless magnetic model and pm flux identification of synchronous drives at standstill,” in *2017 IEEE International Symposium on Sensorless Control for Electrical Drives (SLED)*, 2017. doi: 10.1109/SLED.2017.8078434 pp. 79–84. [Pages 31, 32, and 53.]

[28] L. Ortombina, N. Bianchi, and L. Alberti, “Standstill self-commissioning procedure for synchronous reluctance motors based on coenergy model,” in *2023 IEEE International Electric Machines & Drives Conference (IEMDC)*, 2023. doi: 10.1109/IEMDC55163.2023.10238999 pp. 1–6. [Pages 31 and 32.]

[29] H.-J. Lee, J.-E. Joo, and Y.-D. Yoon, “Standstill sensorless self-commissioning strategy of synchronous machines including initial positioning and torque canceling techniques,” *IEEE Transactions on Industry Applications*, vol. 59, no. 6, pp. 6817–6825, 2023. doi: 10.1109/TIA.2023.3308090 [Pages 31 and 32.]

[30] M. Hinkkanen, P. Pescetto, E. Mölsä, S. E. Saarakkala, G. Pellegrino, and R. Bojoi, “Sensorless self-commissioning of synchronous reluctance motors at standstill without rotor locking,” *IEEE Transactions on Industry Applications*, vol. 53, no. 3, pp. 2120–2129, 2017. doi: 10.1109/TIA.2016.2644624 [Pages 31 and 32.]

[31] ——, “Sensorless self-commissioning of synchronous reluctance motors at standstill,” in *2016 XXII International Conference on Electrical Machines (ICEM)*, 2016. doi: 10.1109/ICELMACH.2016.7732673 pp. 1174–1180. [Pages 31 and 32.]

[32] P. Pescetto and G. Pellegrino, “Determination of pm flux linkage based on minimum saliency tracking for pm-syr machines without rotor movement,” *IEEE Transactions on Industry Applications*, vol. 56, no. 5, pp. 4924–4933, 2020. doi: 10.1109/TIA.2020.3000710 [Pages 32 and 109.]

[33] H. Schierling, “Self-commissioning-a novel feature of modern inverter-fed induction motor drives,” in *Third International Conference on Power Electronics and Variable-Speed Drives*, 1988, pp. 287–290. [Pages 34, 35, 37, and 39.]

[34] A. M. Khambadkone and J. Holtz, “Vector-controlled induction motor drive with a self-commissioning scheme,” *IEEE Transactions on Industrial Electronics*, vol. 38, pp. 322–327, 1991. [Online]. Available: https://api.semanticscholar.org/CorpusID:110610094 [Pages 34 and 35.]

[35] G. B. Reddy, B. P. Muni, and G. Poddar, “Parameter estimation and self-commissioning of high power induction motor drive: Importance with a case study,” in *2020 IEEE International Conference on Power Electronics, Smart Grid and Renewable Energy (PESGRE2020)*, 2020. doi: 10.1109/PESGRE45664.2020.9070520 pp. 1–6. [Pages 34, 35, 37, and 39.]

[36] Y.-S. Kwon, J.-H. Lee, S.-H. Moon, B.-K. Kwon, C.-H. Choi, and J.-K. Seok, “Standstill parameter identification of vector-controlled induction motor using frequency characteristics of rotor bars,” in *2008 IEEE Industry Applications Society Annual Meeting*, 2008. doi: 10.1109/08IAS.2008.227 pp. 1–7. [Pages 35, 37, 38, 39, and 109.]

[37] A. Gastli, “Identification of induction motor equivalent circuit parameters using the single-phase test,” *IEEE Transactions on Energy Conversion*, vol. 14, no. 1, pp. 51–56, 1999. doi: 10.1109/60.749147 [Pages 36, 37, and 39.]

[38] J.-Y. Ruan and S.-M. Wang, “Magnetizing curve estimation of induction motors in single-phase magnetization mode considering differential inductance effect,” *IEEE Transactions on Power Electronics*, vol. 31, no. 1, pp. 497–506, 2016. doi: 10.1109/TPEL.2015.2401835 [Pages 40 and 41.]

[39] S. A. Odhano, A. Cavagnino, R. Bojoi, and A. Tenconi, “Induction motor magnetizing characteristic identification at standstill with single-phase tests conducted through the inverter,” in *2015 IEEE International Electric Machines & Drives Conference (IEMDC)*, 2015. doi: 10.1109/IEMDC.2015.7409177 pp. 960–966. [Pages 40, 41, and 108.]

[40] N. Cherix, “Proportional resonant controller,” Oct 2021. [Online]. Available: https://imperix.com/doc/implementation/proportional-resonant-controller [Page 51.]

[41] Z. Wang, K. Lu, and F. Blaabjerg, “A simple startup strategy based on current regulation for back-emf-based sensorless control of pmsm,” *IEEE Transactions on Power Electronics*, vol. 27, no. 8, pp. 3817–3825, 2012. doi: 10.1109/TPEL.2012.2186464 [Page 57.]

[42] R. Kerkman, J. Thunes, T. Rowan, and D. Schlegel, “A frequency based determination of the transient inductance and rotor resistance for field commissioning purposes,” in *IAS ’95. Conference Record of the 1995 IEEE Industry Applications Conference Thirtieth IAS Annual Meeting*, vol. 1, 1995. doi: 10.1109/IAS.1995.530322 pp. 359–366 vol.1. [Page 63.]

[43] Imperix, “Acg-sdk - automated code generation tools for imperix controllers,” Nov 2023. [Online]. Available: https://imperix.com/software/acg-sdk/ [Page 71.]

[44] S. Strobl, J. Orsinger, and S. Lovejoy, “Motor testbench quick start guide,” Aug 2023. [Online]. Available: https://imperix.com/doc/help/motor-testbench-quick-start-guide [Pages 73, 76, 77, and 78.]

[45] SEW, “Ac motors, asynchronous motors,” 2023. [Online]. Available: https://www.seweurodrive.com/products/motors/ac_motors/ac_motors.html [Pages 79 and 100.]

[46] ——, “Cm3c.. series synchronous servomotors,” 2023. [Online]. Available: https://www.seweurodrive.com/products/servo_drive_technology/servomotors/synchronous-servomotors-cm3c/synchronous-servomotors-cm3c.html [Page 80.]

[47] *Rotating electrical machines - Part 8: Terminal markings and direction of rotation*, International Electrotechnical Commission IEC Standard 60 034-8, 2007. [Page 80.]

[48] *MCR5000 series User Manual*, MATRIX TECHNOLOGY INC., 9 2019. [Page 82.]

[49] Brymen, “Brymen bm785,” 2023. [Online]. Available: https://brymen.eu/shop/bm785/ [Page 82.]

[50] Rigol, “Digital oscilloscope mso5074,” 2023. [Online]. Available: https://rigolshop.eu/product/oscilloscope/mso5000/mso5074.html [Page 82.]

[51] Micsig, “Micsig dp series high voltage differential probe_dp10007/dp10013/dp20003,” 2023. [Online]. Available: https://www.micsig.com/Differential%20Probe04/ [Page 82.]

[52] ——, “Low frequency ac/dc current probe cp2100 series,” 2023. [Online]. Available: https://www.micsig.com/current%20probe/ [Page 82.]

[53] Tektronix, “A6304xl 500 amp ac/dc current probe,” 2003. [Online]. Available: https://www.tek.com/en/manual/a6304xl-500-amp-ac-dc-current-probe [Page 82.]

[54] J. Ruan and S. Wang, “A prediction error method-based self-commissioning scheme for parameter identification of induction motors in sensorless drives,” *IEEE Transactions on Energy Conversion*, vol. 30, no. 1, pp. 384–393, 2015. doi: 10.1109/TEC.2014.2346198 [Page 108.]

[55] S. Wang and M. Lin, “A novel stator resistance online identification method based on adrc,” in *2021 IEEE 4th Student*

Conference on Electric Machines and Systems (SCEMS), 2021. doi: 10.1109/SCEMS52239.2021.9646154 pp. 1–3. [Page 109.]

TRITA-EECS-EX- 2023:0000

www.kth.se